

6-22-2020

Dynamic Response of Highway Bridge Superstructures Subjected to Wave Action: Experimental Analysis and Numerical Modeling

Alaa Waleed Hameed
Portland State University

Follow this and additional works at: https://pdxscholar.library.pdx.edu/open_access_etds



Part of the [Civil Engineering Commons](#)

Let us know how access to this document benefits you.

Recommended Citation

Hameed, Alaa Waleed, "Dynamic Response of Highway Bridge Superstructures Subjected to Wave Action: Experimental Analysis and Numerical Modeling" (2020). *Dissertations and Theses*. Paper 5489.
<https://doi.org/10.15760/etd.7361>

This Dissertation is brought to you for free and open access. It has been accepted for inclusion in Dissertations and Theses by an authorized administrator of PDXScholar. Please contact us if we can make this document more accessible: pdxscholar@pdx.edu.

Dynamic Response of Highway Bridge Superstructures Subjected to Wave

Action: Experimental Analysis and Numerical Modeling

by

Alaa Waleed Hameed

A dissertation submitted in partial fulfillment of the
requirements for the degree of

Doctor of Philosophy
in
Civil and Environmental Engineering

Dissertation Committee:
Thomas Schumacher, Chair
Arash Khosravifar
Christopher Higgins
Minjie Zhu
Hormoz Zareh

Portland State University
2020

Abstract

Bridges are critical lifeline components of the infrastructure network, enabling economies to function under normal conditions and disaster response and recovery missions to take place after extreme events. Therefore, ensuring satisfactory performance increases community resilience and minimizes both human and economic losses. Coastal bridges, which are the focus of this PhD dissertation, are vulnerable to coastal storms. High failure rates of these bridges during two major hurricane events in the mid-2000s have spurred research activities to better understand the wave-induced forces of coastal bridges.

This PhD research represents a continuation effort to build, implement, and introduce new fundamental concepts and methods that are important to the bridge engineering community. The data set analyzed was part of an experimental study conducted at the O. H. Hinsdale Wave Research Laboratory at Oregon State University in 2007. A unique aspect of the setup was that the substructure flexibility of the 1:5-scale bridge specimen could be adjusted by inserting springs with different stiffnesses. The realistic specimen was subjected to a range of wave conditions, water levels, and substructure fixity conditions.

First, a suitable equation of motion was developed as it represents an essential building block for the any for any planned simulation effort. This equation was derived based on the examination of the damping behavior of the system. This effort lead to a better understanding of how the dynamic properties of the bridge superstructure specimen are affected by different levels of submersion, and what their numerical values are.

Second, the available data set was analyzed in depth with the objective to determine the effect of substructure flexibility on the observed wave-induced forces on the bridge superstructure specimen. Reinforced by the test of restriction, it was found that that the measured forces experienced by the superstructure specimen with a flexible substructure were notably larger compared to the rigid case. These findings highlight the need to account for substructure flexibility when estimating wave forces. The proposed force magnification factors can be used in conjunction with code equations that are based on rigid support conditions.

Finally, in order to expand the understanding of substructure flexibility and exploring test conditions that are not part of the original experimental dataset, having a numerical model is a promising solution. The particle finite element method (PFEM) was selected as the tool for this purpose and is introduced and evaluated against sample responses from the experiment.

In conclusion, support conditions affect the dynamic response of bridges subjected to wave action and thus need to be considered. This PhD dissertation created a better fundamental understanding of how bridges respond dynamically to wave action considering varying levels of submersion as well as substructure flexibility. The findings allow bridge engineers to build more accurate numerical models for fluid-structure interaction problems and provide practical guidance with respect to the magnification of wave-induced forces for design and evaluation applications.

Acknowledgments

I would like to express my gratefulness to Allah (The Merciful and most Griseous, The provider) for his mercy and guidance, and surrounding me with amazing people who had directly influenced me in my life journey in general and during my PhD study in special. The only way of showing this gratefulness is by thanking those people. Words will not be sufficient to express thanks, to...

... my parents, thanks for your genuine and continuous streaming of help and love all lifelong, for your encouragement to continue my study abroad and for your prayers.

... my husband and children, thanks for your presence and support during my study, for your understanding, patience and sacrificing your needs to grant me extra time to study.

... The Higher Committee for Education in Iraq (HCED), for sponsoring my study in Portland State University for six years.

... my advisor (Dr. Thomas Schumacher), for providing me the data and sketches present in this dissertation, trusting and patience, and his continuous advice, help and support until the last minutes of preparing this dissertation.

... Dr. Zhu for his support and help in learning and implementing OpenSeesPy.

... Dr. Higgins for his valuable comments and assistance.

Table of Contents

Abstract	i
Acknowledgments	iii
List of Tables	vi
List of Figures	vii
Chapter 1	1
Introduction.....	1
1.1 Introduction	1
1.2 Dissertation Outline	4
1.3 References.....	8
Chapter 2.....	10
Manuscript 1: Characterization of Dynamic Properties from Free Vibration Tests of a Large-Scale Bridge Model	10
2.1 Introduction and Background	10
2.2 Motivation and Significance.....	13
2.3 Experimental Test Setup and Free Vibration Tests	14
2.4 Initial Observations from Free Vibration Tests	17
2.5 Analysis.....	21
2.5.1 Numerical Model	21
2.5.2 Parameter Estimation.....	23
2.6 Quantification of Added Mass Parameters	33
2.7 Summary and Conclusions	36
2.8 References.....	38
Chapter 3.....	41
Manuscript 2: Effect of Substructure Flexibility on Wave-induced Forces on Bridge Superstructures	41
3.1 Introduction and Background	41
3.2 Motivation and Objectives	47
3.3 Experimental Setup	48
3.4 Data Analysis	55
3.4.1 Unnormalized feature analysis.....	55

3.4.2 Normalized feature analysis	60
3.5 Substructure Flexibility Effect	63
3.6 Summary and Conclusion	71
3.7 References	73
Chapter 4.....	75
Manuscript 3: Implementation of the OpenSeesPy Particle Finite Element Method (PFEM) to Study Wave-induced Forces on Bridge Superstructures.....	76
4.1 Introduction	75
4.2 Motivation and Objective	77
4.3 Overview of the PFEM Method.....	78
4.4 Governing Equations.....	79
4.5 Experimental Study	81
4.6 Simulations.....	83
4.7 Model Validation and Results.....	86
4.8 Summary and Conclusions	94
4.9 References	95
Chapter 5.....	99
Conclusions and Future Work	100
5.1 Summary and Conclusions	99
5.2 Recommendations for Future Work.....	101
Appendix A: Runge-Kutta Method	103
Appendix B: Global Search Algorithm Validation.....	108
Appendix C: Parametric Study Exploring Effect of Damping Types on Response	110
Appendix D: Scatter Plots of Wave-Induced Forces vs. Wave Height.....	118
Appendix E: Magnification Factors for all Cases	119
Appendix F: Experiment -simulation results comparisons	122
Appendix G: Flexibility Effect via Experiment and Simulation Results.....	123

List of Tables

Table 2.1. Test matrix of free vibration tests.....	16
Table 2.2. Natural vibration frequencies, f_n for different test trials and phases obtained by DFT.	19
Table 2.3. Parameter estimates for all test trials obtained from the global search method.....	27
Table 2.4. Added mass factors and added mass coefficients calculated for both setups in fully submerged condition, 2a (= medium springs) and 2b (= soft springs)*.....	34
Table 2.5. Hydrodynamic mass per unit length for circular and rectangular sections.....	36
Table 3.1. Structural configurations and test phases investigated in [6] and used in this study.....	48
Table 3.2. Studied still water levels (SWL).	51
Table 3.3. Test of restrictions results.....	67
Table 3.4. Force magnification factors at different percentiles, for both horizontal and vertical forces.....	70

List of Figures

Figure 2.1. Elevation view of bridge superstructure model with key instrumentation used in this study (a) from the side and (b) looking down the flume. Dimensions are (m). Notation: LC = load cell, SWL = still water level, zd = mean water depth, hd = superstructure depth, d^* = non-dimensional water level.	15
Figure 2.2. Photo of experimental test setup during Phase 2a (medium springs, indicated by arrows). The inset shows the quick-release mechanism that initiated free vibration with initial displacement.	16
Figure 2.3. Example free vibration response for Phase 2b, dry trial: (a) time history and (b) frequency domain (Trial 2001: dry setting with soft spring).....	18
Figure 2.4. Comparison of logarithmic decrements for (a) theoretical values for three different types of damping following [26] and (b) free vibration tests from large-scale bridge superstructure model. The terminology in legend detailed in Table 1.....	20
Figure 2.5. Example force - displacement response of model with mean prediction line from linear regression (Trial 2303, 3rd water level with soft springs)....	26
Figure 2.6. Box-and-whisker plot for the estimated parameters as a function of water level with median based estimation. Also shown are numerical values for the means.....	29
Figure 2.7. Comparison between experimental data and numerical model for Phase 2a (medium springs setup) and 2b (soft springs setup) for select trials and water levels. Also listed are the numerical values of the estimated parameter values.	32
Figure 2.8. Parameters for the computation of the reference mass, m_{ref}	34
Figure 3.1. Photo of superstructures of the US 90 Biloxi Bay Bridge that have been removed from their substructures by wave loads during Hurricane Katrina. Source [2].	41
Figure 3.2. Elevation view of experimental test setup showing different horizontal support conditions, i.e. test phases (LC = load cell, SWL = still water level). Dimensions: m (ft). (Courtesy of Dr. Schumacher).	49
Figure 3.3. Elevation view of bridge superstructure under wave action with commonly used terminology. (Courtesy of Dr. Schumacher).....	50
Figure 3.4. Sample experimental measurements for $d^* = 0.0$, $T = 3.0$ s, $H = 0.625$ m, Phase 1: Time histories of (a) Water level at WG 9, 4.21 m (13.8 ft) away from front face of the bridge model, (b) total horizontal force, (c) total vertical force (WG = wave gage).....	51
Figure 3.5. A close-up view for a sample time-history for a total vertical force due to two passing waves.....	53

Figure 3.6. A close-up view for a sample time-history for the effect of substructure fixity on the on the observed wave force at same wave condition.	54
Figure 3.7. Boxplots of horizontal (left) and vertical (right) wave forces vs. normalized water level for wave height = 0.5 m and wave period = 2.5 s for rigid setup.	56
Figure 3.8. Scatter plots of (a) horizontal and (b) vertical wave forces vs. wave height. Normalized water depth, $d^* = +0.5$ and wave period, $T_p = 2.5$ s.	58
Figure 3.9. Scatter plots of (a) horizontal and (b) vertical wave forces vs. wave steepness. Normalized water depth, $d^* = +0.5$ and wave period, $T_p = 2.5$ s.	59
Figure 3.10. Scatter plots of (a) horizontal and (b) vertical wave forces vs. wave celerity. Normalized water depth, $d^* = +0.5$ and wave period, $T_p = 2.5$ s. ...	60
Figure 3.11. Scatter plots of normalized horizontal wave force vs. relative width.	61
Figure 3.12. The relative energy preservation at different water levels and wave heights.	63
Figure 3.13. Illustration of force magnification factors for sample horizontal force with $d^* = 0.0$ and $T_p = 2.5$ s: (a) Mean curve fit lines along with 95% prediction limits for the horizontal wave forces and (b) force magnification factors for different substructure flexibilities, considering the rigid condition as the reference value. Error bars represent 95% prediction limits of the curve fits.	65
Figure 3.14. Illustration of force magnification factors for sample vertical force with $d^* = 0.0$ and $T_p = 2.5$ s: (a) Mean curve fit lines along with 95% prediction limits for the vertical wave forces and (b) force magnification factors for different substructure flexibilities, considering the rigid condition as the reference value. Error bars represent 95% prediction limits of the curve fits.	65
Figure 3.15. Boxplot of the force magnification factors for both horizontal and vertical forces. Numerical values shown represent the median value for the specified group.	68
Figure 3.16. Boxplot of the force magnification factors for both horizontal and vertical forces for the all data. Numerical values shown represent the median value for the specified group.	69
Figure 3.17. Derived MGF from logistic distribution.	70
Figure 4.1. Elevation view of the large wave flume. (Courtesy of Dr. Schumacher).	82
Figure 4.2. Drawing of bridge superstructure specimen with key instrumentation used in this study (a) elevation view (longitudinal cut) and (b) view up the flume (cut across the flume). Dimensions: m (ft). Notation: LC = load cell, SWL = still	

water level, h = water depth, h_c = superstructure depth. (Courtesy of Dr. Schumacher)	83
Figure 4.3. Simulation domain of the bridge superstructure setup.....	86
Figure 4.4. Effect of mesh size on propagating wave height.	87
Figure 4.5. Effect of mesh size on simulated forces.	89
Figure 4.6. Simulation results for horizontal forces compared with the experimental data for case $d^* = -0.5$, $H = 0.75\text{m}$, and $T_p = 3.0\text{ s}$, and for both rigid and soft setups.	90
Figure 4.7. Simulation results for vertical forces compared with the experimental data for case $d^* = -0.5$, $H = 0.75\text{m}$, and $T_p = 3.0\text{ s}$, and for both rigid and soft setups.	91
Figure 4.8. Effect of substructure flexibility on horizontal forces for experiment results.	92
Figure 4.9. Effect of substructure flexibility on horizontal forces for simulation results.	93

Chapter 1

Introduction

1.1 Introduction

Bridges are critical lifeline components of the infrastructure network, enabling economies to function under normal conditions and disaster response and recovery missions to take place after extreme events. Their satisfactory performance increases community resilience and minimizes both human and economic losses. Therefore, enhancing the understanding of the behavior of these structures as they interact with waves has become an important area of study for many researchers.

Deck girder bridges, a common type of coastal bridge, can be divided in terms of three components: superstructure (which refers to the top part of the structure, including deck, girders, and diaphragms), substructure (which refer to the bottom part of the structure, consisting of bent columns and caps), and the connections between them. Due to the impact of hurricanes on coastal bridges, and contemplating on the failure modes of these structures, many researchers have been motivated to understand and estimate the wave-induced forces on bridges to improve bridge engineering practice [1]–[4]. These efforts have varied between being purely theoretical or numerical in nature [5]–[10] or by means of experimental testing [11]–[14]. Most of these studies assumed the investigated bridge component to be supported rigidly when studying the estimated forces. Since this

represents a simplification that is not realistic of a bridge in the real world, researchers [11], [12] considered substructure flexibility as an important factor to be investigated and its effect on wave forces to be determined. A preliminary study in 2008 [15] showed the difference between the magnitudes of the measured forces for different fixity conditions. Since then, only a few studies have been performed to investigate this effect, and with contradictory findings [8], [16], [10].

Creating a better understanding and quantifying the effect of substructure flexibility on the dynamic properties as well as the wave-induced forces on bridge superstructures were thus the inspiration and represent the key objectives of this PhD dissertation. Because conducting large-scale experiments costs effort, time, and money, simulations using numerical methods has become an important alternative in engineering research and practice. The particle finite element method (PFEM) is particularly powerful to simulate fluid-structure interaction problems [17]–[20], and was chosen in this research to build numerical models that would be representative of the experimental tests.

This PhD research represents a continuation effort to build, implement, and introduce new fundamental concepts and methods that are important to the bridge engineering community. The data analyzed was part of an experimental study conducted at the O. H. Hinsdale Wave Research Laboratory at Oregon State University in 2008 [11]. In this research effort, a realistic 1:5-scale bridge superstructure specimen was subjected to over 400 wave trials with different wave conditions and structural configurations and the resulting forces at the specimen supports measured in the vertical and horizontal directions. A unique aspect of the

setup is that the support conditions of the substructure could be adjusted to represent different horizontal bridge bent (or substructure) stiffnesses. In total, three substructure flexibilities were modeled: rigid, medium, and soft, enabling the team to create a unique and realistic dataset.

This PhD research starts by studying the dynamic properties of the bridge superstructure specimen. A suitable equation of motion was developed as it represents an essential building block for any planned simulation effort. This equation of motion was derived based on the examination of the damping behavior of the system. An additional outcome of this study is the estimation of those dynamic quantities (i.e., added mass and damping) that have a potential explanation to the dynamic behavior of the structure. Based on the available dataset from the large-scale experiment [11], a preliminary analysis of the data showed evidence that the measured forces experienced by the superstructure specimen with a flexible substructure were notably larger compared to the rigid case. The findings highlight the need to account for substructure flexibility when estimating wave forces. The proposed force magnification factors can be used in conjunction with code equations that are based on rigid support conditions. Finally, in order to expand the understanding of substructure flexibility and exploring test conditions that are not part of the original experimental dataset, having a numerical model is a promising solution. The particle finite element method (PFEM) was selected as the tool for this purpose and is introduced and evaluated against sample responses from the experiment.

1.2 Dissertation Outline

This PhD dissertation follows the multi-paper format per Portland State University's electronic thesis and dissertation (ETD) formatting requirements and is divided into five chapters. Chapters 1 and 5 are the introduction and conclusion chapters, respectively, whereas Chapters 2 to 4 represent manuscripts intended for submission to peer-reviewed journals.

- In Chapter 1, an introduction and the motivation to the performed research is provided along with this outline.
- Chapter 2 is the first manuscript entitled "Characterization of Dynamic Properties from Free Vibration Tests of a Large-Scale Bridge Model" and investigates the dynamic properties of a bridge superstructure specimen introduced in [11] under free vibration during varying levels of submersion. It is co-authored by Thomas Schumacher (adviser), Christopher Higgins, and Brittany Erickson, and is currently under review in the *Journal of Fluids and Structures*.

Abstract: To accurately predict dynamic response of a structure subjected to fluid induced loading, a thorough understanding of the dynamic properties (mass, stiffness, and damping) and associated interactions is required. Limited data are available to characterize dynamic fluid-structure interactions. Data are particularly limited for large scale and flexible structural models. In this article, the dynamic response characteristics of a large-scale highway bridge superstructure model were extracted from free vibration tests under varying water levels in the laboratory. The nature of the damping response was

identified based on the exhibited logarithmic decrements of the model's free vibration displacement amplitudes, and a suitable equation of motion (EOM) was subsequently developed. Using the classical fourth-order Runge-Kutta method, the EOM was solved for the different test trials and the dynamic parameters of the model were obtained through optimization employing a genetic algorithm. Finally, the values for two important quantities, namely added mass factor and added mass coefficient, were computed for the fully submerged bridge superstructure model. This study provides the suitable EOM needed for numerical simulations of fluid-structure interaction problems of the studied experiment and a method for establishing structural dynamic properties of hydro-dynamic analytical models.

- Chapter 3 is the second manuscript entitled “Effect of Substructure Flexibility on Wave-induced Forces on Bridge Superstructures” and investigates the effect of substructure flexibility on the observed forces on bridge superstructures due to wave action using experimental data. Co-authors include Thomas Schumacher (adviser), Christopher Higgins, and Avinash Unnikrishnan. This manuscript is currently being prepared for submission to a journal.

Abstract: Hurricane-induced wave forces have caused major damage on bridges ranging from local damage due to debris impact to complete removal of superstructures due to deficient connections failing between sub- and superstructures. Much research, both experimental as well as numerical, has been completed over the last two decades to study wave forces on bridges.

Most of the work, however, has focused on the hydraulics aspect, omitting structural engineering considerations. A particular aspect that has not received much attention is the effect of substructure flexibility on the forces a bridge superstructure has to endure during a hurricane event. The objective of the study discussed in this article was three-fold. First, a unique large-scale experimental dataset was analyzed to determine whether the effect of substructure flexibility has a statistically significant effect on the horizontal and vertical forces experienced by a bridge superstructure. Second, a physics-based explanation was developed to describe the observations. Third, force magnification factors were determined for different exceedance levels that bridge engineers can use in conjunction with existing force prediction equations that were developed using rigid substructures. In summary, substructure flexibility affects the magnitudes of the induced wave forces at the 95% confidence level. Longer waves create larger magnification factors for more flexible substructures. Force magnification factor magnitudes are close and largest for the two examined substructure flexibilities for the case when the superstructure is not submerged; they decrease with increasing levels of submersion.

- Chapter 4 represents the third manuscript entitled “Implementation of the OpenSEESPy Particle Finite Element Method (PFEM) to Study Wave-induced Forces on Bridge Superstructures”. In this chapter, the particle finite element method (PEFM) is introduced and implemented to build a simulation model for the bridge specimen. Co-authors include Minjie Zhu, Thomas Schumacher

(adviser), and Christopher Higgins. This manuscript is currently being prepared for submission to a journal.

Abstract: The response of coastal bridges subject to wave forces has been studied quite extensively over the last decade. In particular, the effect of substructure flexibility on the induced wave forces on bridge superstructures has been received little attention. Moreover, the few studies that have investigated it hold two different opinions. While one group claims that as structural support flexibility increases, the induced wave forces increase, the other group claims that the induced wave forces decrease. Information regarding this influence is critical for both the design of new systems as well as the evaluation of existing ones. In this study, the Particle Finite Element Method (PFEM) is implemented and validated using a large-scale experimental study performed at Oregon State University for a bridge superstructure specimen subjected to different wave and support conditions. The simulation results show acceptable agreement with the experimental results and provide initial evidence that an increase in substructure flexibility result in an increase in the wave-induced forces on the superstructure. By utilizing this model, cases that were not tested as part of the physical experiment can be simulated and additional relationships studied.

- Chapter 5 presents the main conclusions drawn from this research and suggests potential future work.

1.3 References

- [1] “Development of the AASHTO guide specifications for bridges vulnerable to coastal storms | Request PDF,” ResearchGate.
https://www.researchgate.net/publication/299678527_Development_of_the_AASHTO_guide_specifications_for_bridges_vulnerable_to_coastal_storms (accessed Nov. 09, 2018).
- [2] D. James, J. Cleary, and S. Douglass, “Estimating Wave Loads on Bridge Decks,” in Structures Congress 2015, 2015, pp. 183–193.
- [3] R. L. McPherson, “Hurricane induced wave and surge forces on bridge decks,” PhD Thesis, Texas A & M University, 2010.
- [4] J. Marin and D. M. Sheppard, “Storm surge and wave loading on bridge superstructures,” in Structures Congress 2009: Don’t Mess with Structural Engineers: Expanding Our Role, 2009, pp. 1–10.
- [5] Q. Chen, L. Wang, and H. Zhao, “Hydrodynamic investigation of coastal bridge collapse during Hurricane Katrina,” *J. Hydraul. Eng.*, vol. 135, no. 3, pp. 175–186, 2009.
- [6] H. Xiao, W. Huang, and Q. Chen, “Effects of submersion depth on wave uplift force acting on Biloxi Bay Bridge decks during Hurricane Katrina,” *Comput. Fluids*, vol. 39, no. 8, pp. 1390–1400, Sep. 2010, doi: 10.1016/j.compfluid.2010.04.009.
- [7] B. Huang, B. Zhu, S. Cui, L. Duan, and J. Zhang, “Experimental and numerical modelling of wave forces on coastal bridge superstructures with box girders, Part I: Regular waves,” *Ocean Eng.*, vol. 149, pp. 53–77, 2018.
- [8] X. Chen, J. Zhan, Q. Chen, and D. Cox, “Numerical Modeling of Wave Forces on Movable Bridge Decks,” *J. Bridge Eng.*, vol. 21, no. 9, p. 04016055, Sep. 2016, doi: 10.1061/(ASCE)BE.1943-5592.0000922.
- [9] J. Jin and B. Meng, “Computation of wave loads on the superstructures of coastal highway bridges,” *Ocean Eng.*, vol. 38, no. 17–18, pp. 2185–2200, 2011.
- [10] G. Xu and C. S. Cai, “Numerical investigation of the lateral restraining stiffness effect on the bridge deck-wave interaction under Stokes waves,” *Eng. Struct.*, vol. 130, pp. 112–123, 2017.
- [11] C. Bradner, T. Schumacher, D. Cox, and C. Higgins, “Experimental setup for a large-scale bridge superstructure model subjected to waves,” *J. Waterw. Port Coast. Ocean Eng.*, vol. 137, no. 1, pp. 3–11, 2010.
- [12] D. Istrati, “Large-Scale Experiments of Tsunami Inundation of Bridges Including Fluid-Structure-Interaction,” PhD Thesis, 2017.
- [13] M. Hayatdavoodi, B. Seiffert, and R. C. Ertekin, “Experiments and computations of solitary-wave forces on a coastal-bridge deck. Part II: Deck with girders,” *Coast. Eng.*, vol. 88, pp. 210–228, 2014.
- [14] G. Cuomo, K. Shimosako, and S. Takahashi, “Wave-in-deck loads on coastal bridges and the role of air,” *Coast. Eng.*, vol. 56, no. 8, pp. 793–809, Aug. 2009, doi: 10.1016/j.coastaleng.2009.01.005.

- [15] T. Schumacher, C. Higgins, C. Bradner, D. Cox, and S. C. Yim, "Large-Scale Wave Flume Experiments on Highway Bridge Superstructures Exposed to Hurricane Wave Forces," presented at the Sixth National Seismic Conference on Bridges and Highways Multidisciplinary Center for Earthquake Engineering Research South Carolina Department of Transportation Federal Highway Administration Transportation Research Board, 2008, Accessed: Mar. 09, 2020. [Online]. Available: <https://trid.trb.org/view/1120856>.
- [16] G. Xu and C. S. Cai, "Numerical simulations of lateral restraining stiffness effect on bridge deck–wave interaction under solitary waves," *Eng. Struct.*, vol. 101, pp. 337–351, 2015.
- [17] S. R. Idelsohn, E. Oñate, F. D. Pin, and N. Calvo, "Fluid–structure interaction using the particle finite element method," *Comput. Methods Appl. Mech. Eng.*, vol. 195, no. 17, pp. 2100–2123, Mar. 2006, doi: 10.1016/j.cma.2005.02.026.
- [18] E. Oñate, M. A. Celigueta, S. R. Idelsohn, F. Salazar, and B. Suárez, "Possibilities of the particle finite element method for fluid–soil–structure interaction problems," *Comput. Mech.*, vol. 48, no. 3, p. 307, Jul. 2011, doi: 10.1007/s00466-011-0617-2.
- [19] E. Oñate, S. R. Idelsohn, F. Del Pin, and R. Aubry, "The particle finite element method — an overview," *Int. J. Comput. Methods*, vol. 01, no. 02, pp. 267–307, Sep. 2004, doi: 10.1142/S0219876204000204.
- [20] M. Zhu, I. Elkhatali, and M. H. Scott, "Validation of OpenSees for Tsunami Loading on Bridge Superstructures," *J. Bridge Eng.*, vol. 23, no. 4, p. 04018015, Apr. 2018, doi: 10.1061/(ASCE)BE.1943-5592.0001221.

Chapter 2

Manuscript 1: Characterization of Dynamic Properties from Free Vibration Tests of a Large-Scale Bridge Model

This manuscript is co-authored by Thomas Schumacher (adviser), Christopher Higgins, and Brittany Erickson, and is currently under review in the *Journal of Fluids and Structures*.

2.1 Introduction and Background

Hurricanes in 2004 (Ivan) and 2005 (Katrina) caused failure of many existing coastal highway bridges. Bridge structures are critical lifeline components of the infrastructure network, enabling disaster response and recovery. Therefore, ensuring satisfactory performance increases community resilience and minimizes both human and economic losses. The observed bridge failures spurred research to better understand wave forces on bridges and fluid-structure interaction has become an important area of study for the engineering community.

One type of bridge structure that was particularly affected by past hurricane events is simply supported prestressed concrete bridges. Weak or non-existent connections [1] were found to be the main cause for bridges failures due to hurricane wave impacts. Connection failures allowed the superstructure to be washed off the substructure and into the water. Therefore, many experimental [2]–[8], mathematical [9], [10], theoretical, semi-empirical [11], and numerical [12]–[14] research studies have been conducted to quantify wave hydrodynamic forces on

these structures. Theoretical studies investigated the wave kinematics and momentum of the water body in order to derive force equations, considering simplified assumptions. Moreover, these studies resolved the problem of estimating the induced forces from a fluid mechanics perspective, which represents a significant limitation given that the measured experimental response is represented by the convolution between the force function with the impulse response function of the structure. Guo et al. [15] evaluated this feature in their laboratory experiment and presented a methodology to de-convolve the two functions. In other words, the structure's dynamic properties are expected to influence the forces experienced by the structure.

Multivariate regression analyses have been utilized for a variety of applications and provide means to study relationships between input parameters and empirically observed wave forces. In an earlier study [16], a multivariate regression analysis was employed without considering the convolution behavior of the collected data. To improve that, the study presented in this article investigated the dynamic characteristics of a highway bridge superstructure model that will enable the implementation of additional regressor variables for such analyses. Most models, numerically or experimentally, were dedicated to study wave impacts on bridge superstructures with fixed supports, representing rigid substructures [3], [4], [17], [18]. Bradner et al. [2] report the first large-scale experiment that allowed for varying the horizontal support flexibility to represent realistic structural behavior of the substructure. The bridge superstructure model used was a realistic 1:5-scale model representing the I-10 Bridge over Escambia Bay, FL. This causeway was

severely damaged during Hurricane Ivan in 2004. Over the period of one year, the researchers created a large data set consisting of over 400 test trials that varied the following parameters: wave period, wave height, still water level, presence of a guardrail, and substructure flexibility. Trials consisted of regular as well as random waves. Additionally, a series of free vibration tests were conducted under varying water levels and are the subject of this article. Most prior studies have considered the case of fixed support conditions [5], [12], [14], [15]. To date, few numerical studies have investigated the effect of flexibility on wave forces numerically [19]–[21]. Interestingly, these findings are conflicted as to whether substructure flexibility increases or decreases the wave forces experienced by the superstructure. Chen et al. [19] showed that as structural flexibility increases, a reduction to the force magnitude occurs. Xu and Cai [20], [21] on the other hand, showed the opposite. All of these studies used the data produced in [2] to verify their numerical models. Istrati [8], in 2017, conducted an experimental test similar to the 1:5 large-scale experimental study presented in [2]. In that experiment, the effect of tsunami wave loads on a composite bridge model with four steel I-girders were examined. The researchers report that the structure's dynamics affect the observed forces and they used slightly different support conditions than those employed in [2]. Bradner et al. [2] studied the total horizontal stiffness of the substructure only. Istrati used the same setup (two horizontal springs of different stiffness) but added elastomeric and steel bearings between the bridge model and the substructure.

2.2 Motivation and Significance

As mentioned in the previous section, most experimental tests and numerical models have used a rigidly supported bridge structure, which does not properly reflect realistic structural stiffness [2], [8]. As presented in [8], [22], structural dynamics have an important effect on the measured forces. Except for the two large scale experimental tests performed by Bradner et al. (2010) [2] and Istrati (2017) [8], substructure flexibility and dynamic effects on the measured wave forces have not been investigated experimentally. During the period between these two experiments, researchers attempted to address this issue by building and studying numerical models using the data presented in [2] to validate their models. Some prior research has applied regression models that exclude the dynamic structural behavior.

This paper focuses on the dynamic system properties required to define and develop a numerical model using the equation of motion (EOM) for the studied structure. The study reported in this article provides the required modeling components: proposes and evaluates an appropriate EOM and provides a method to properly capture the salient dynamic properties. Free vibration test data from a large-scale model were analyzed (data from [2]) that presents a unique opportunity to infer the dynamic properties required to capture dynamic responses and the influence of varying levels of submersion on such properties including model frictional resisting forces, hydrodynamic and hydroviscous damping. The former refers to the combined damping effect of the water body (added mass and added

damping), whereas the latter refers to the specific contribution of the water body to the effect of viscous damping.

2.3 Experimental Test Setup and Free Vibration Tests

The experimental test setup is illustrated in Fig. 1 and described in full detail in [2]. A unique aspect of this setup is the ability to change the flexibility of the substructure to represent different horizontal bridge bent stiffnesses. This is achieved by inserting coil springs between the horizontal load cell (LC) and the end block of the steel reaction frame. Two springs with different stiffnesses (labeled “Phase 2a” and “Phase 2b”) were selected to be representative of actual prototype substructure configurations (see [23]). Phase 1 represents the rigid configuration without a spring while Phase 2a and 2b represent medium and soft substructure configurations, respectively. The stiffnesses of the springs representing these configurations were selected based on a finite element analysis of different bent frame configurations with battered piles (for details see [24]).

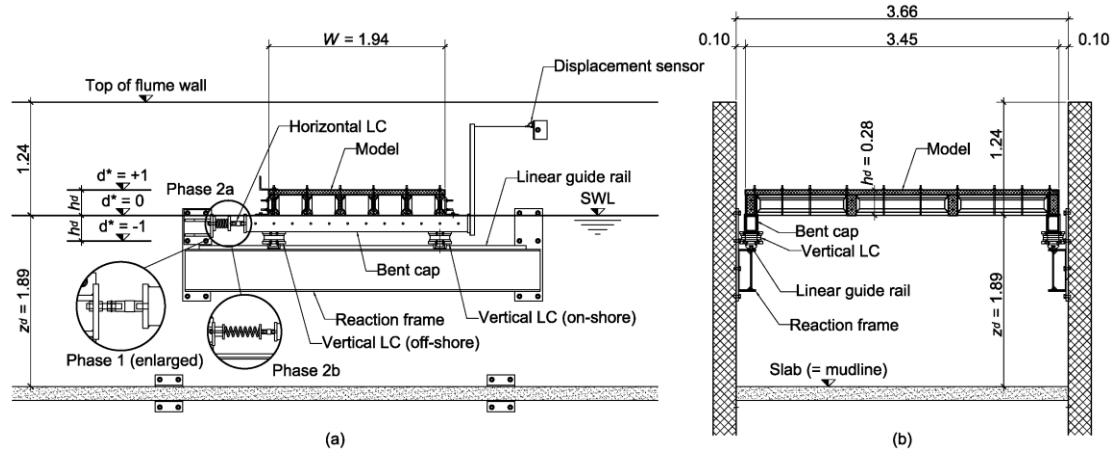


Figure 2.1. Elevation view of bridge superstructure model with key instrumentation used in this study (a) from the side and (b) looking down the flume. Dimensions are (m). Notation: LC = load cell, SWL = still water level, z_d = mean water depth, h_d = superstructure depth, d^* = non-dimensional water level.

A series of free vibration tests were conducted for two flexible substructure configurations and three different still water levels (SWL), as illustrated in Figure 2.1. Figure 2.1 shows the elevation views of the specimen and setup which is located near the center of the flume. The physical model is shown in Figure 2.2. In Figure 2.2, the model bridge superstructure is shown during one of the free-vibration tests. For the free-vibration test, the superstructure was slowly tensioned using a hoist and then suddenly released with a quick-release mechanism (shown in inset) to induce free vibration response with known initial displacement. The test matrix is illustrated in Table 2.1. The non-dimensional parameter, d^* represents the still water level (SWL) elevation relative to the bottom of the girders [24]. The absolute horizontal motion of the bridge superstructure model during the free vibration tests was measured with two displacement sensors (string

potentiometers) attached near the flume walls. The sampling frequency for all trials was 500 Hz.

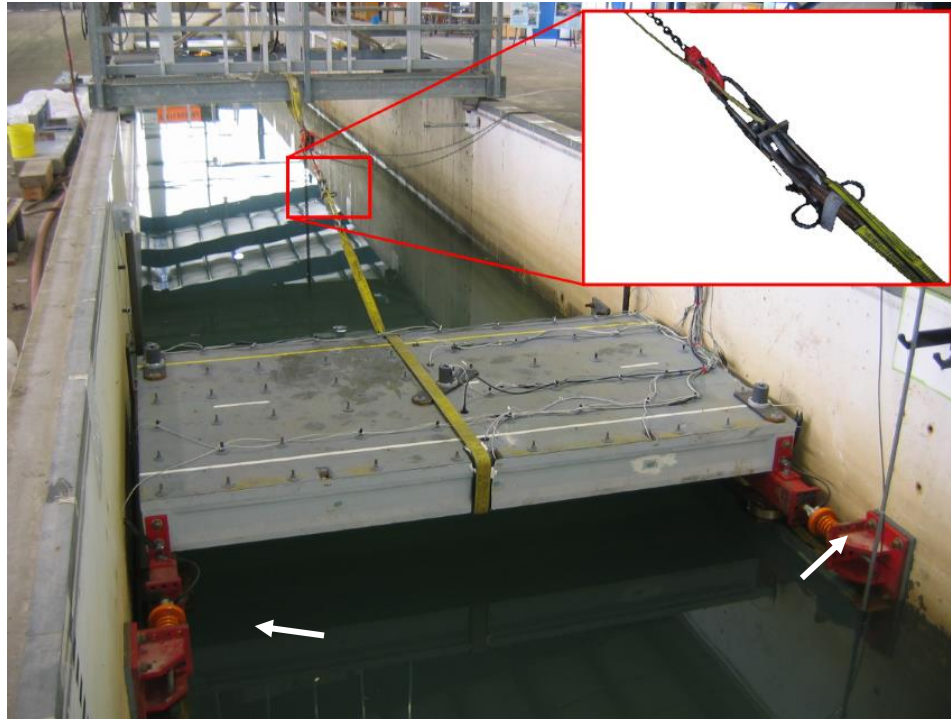


Figure 2.2. Photo of experimental test setup during Phase 2a (medium springs, indicated by arrows). The inset shows the quick-release mechanism that initiated free vibration with initial displacement.

Table 2.1. Test matrix of free vibration tests.

Phase	SWL (m)	d^* (-)	Number of trials	Description
2a	-1.89	dry	3	No water in the flume
	- 0.28	-1		SWL is one full depth of the bridge deck thickness is below the bottom of the girders
	+/- 0.00	0		Water level at bottom of girders, bent cap fully submerged
	+ 0.28	+1		Bridge superstructure fully submerged
2b	-1.89	dry		No water in the flume
	- 0.28	-1		SWL is one full depth of the bridge deck thickness is below the bottom of the girders
	+/- 0.00	0		Water level at bottom of girders, bent cap fully submerged
	+ 0.28	+1		Bridge superstructure fully submerged

2.4 Initial Observations from Free Vibration Tests

The bridge model setup can be represented as a single degree of freedom (SDF) system consisting of a mass, spring, and damper. In order to write an equation of motion to fully represent the model, the type of damping should first be defined. Since the model superstructure is mounted on linear guide rails to allow translational motion in the horizontal direction, a friction force exists. This force is expected to govern in the dry trials and for $d^* = -1$. The presence of water in the subsequent trials, when the model is partially or fully submerged, i.e. for $d^* = 0$ and $+1$, results in two types of damping. As discussed later in this section, based on the free vibration response analysis, total damping is a combination of viscous and friction (also called Coulomb) damping.

The time histories of the free vibration tests (see Table 2.1) were visualized in the time domain and analyzed in the frequency domain by means of the discrete Fourier transform (DFT). Zero-padding was used on the signals to increase the resolution in the frequency domain. An example response for Trial 2001 (Phase 2b, dry) both in the time and frequency domains is shown in Figure 2.3(a) and (b), respectively. Also shown in Figure 2.3 (a) are the symbols and definitions used in the computation of logarithmic decrements, which is discussed later in this section.

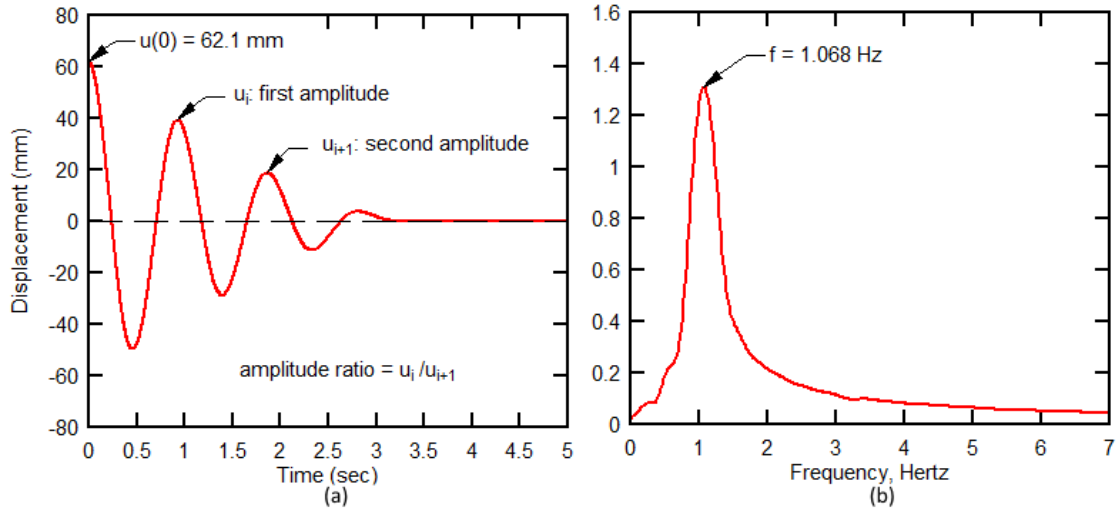


Figure 2.3. Example free vibration response for Phase 2b, dry trial: (a) time history and (b) frequency domain (Trial 2001: dry setting with soft spring).

The natural vibration frequencies, f_n , for different springs at the different water levels and all test trials are reported in Table 2.2. As can be observed, the frequencies decreased with increasing water level, which is particularly obvious for the fully submerged case of $d^* = +1$. This can be explained by the concept of added mass [25]–[27] whereby when a submerged body vibrates, it accelerates the surrounding fluid particles, that act as additional mass and damping compared to a body vibrating in air. For bodies submerged in water, this effect reduces the natural frequency of the vibrating body and increases the damping compared to what it would be in air [25]. Chandrasekaran et al. [25] also showed that the virtual mass “depends on the geometry and the size of the structure, dynamic properties of the structure in air (including its flexibility), the level of submergence, and the type of excitation to which it is subjected.” Additionally, they report that the stiffness of the structure is not affected by the level of submergence.

Table 2.2. Natural vibration frequencies, f_n for different test trials and phases obtained by DFT.

d^*		Phase 2a (medium springs)			Phase 2b (soft springs)		
		dry	Trial #	3001	3002	3003	2001
f_n (Hz)	2.159		2.151	2.151	1.068	1.068	1.068
-1	Trial #	3101	3102	3103	2101	2102	2103
	f_n (Hz)	2.151	2.151	2.151	1.068	1.068	1.076
0	Trial #	3301	3302	3303	2301	2302	2303
	f_n (Hz)	2.132	2.132	2.129	1.060	1.060	1.060
1	Trial #	3501	3502	3503	2501	2502	2503
	f_n (Hz)	1.926	1.915	1.911	0.885	0.885	0.885

Following the research presented in [28], logarithmic decrements were computed to identify the types of damping present in the system for all free vibration test trials in this study. Figure 2.4 (a) shows the theoretical logarithmic decrement behaviors obtained by solving the EOM via Runge-Kutta method for three types of damping: linear viscous (i.e., when the damping force is proportional to velocity), nonlinear viscous (i.e., when the damping force is a quadratic function of velocity), and Coulomb (or friction) damping. The abscissa is interpreted as vibration amplitudes decreasing in time. For linear viscous damping, the logarithmic decrement is independent of the amplitude; therefore, it is a constant value during vibration. For the nonlinear viscous damping case, the logarithmic decrement is a function of amplitude and thus decreases linearly. Lastly, for friction damping, the behavior is also dependent on the amplitude of vibration; however, it increases exponentially. The amplitude values used in the computation of the logarithmic decrements for Figure 2.4 were illustrated in Figure 2.3. The logarithmic decrements measured for the free vibration response for all trials are

shown in Figure 2.4b. and are compared with the expected behaviors (theoretical behavior) of the three damping models [28] (shown previously in Figure 2.4a).

Comparing Figure 2.4(a) and (b), one can observe that for the medium spring setup (Phase 2a) the damping behavior follows that of a viscous damping system at the beginning of the response; however, at the end of the response, the behavior changes and resembles a friction damped system. For the soft spring setup (Phase 2b), possibly because of the limited number of vibration cycles, the behavior is not as clear for the submerged cases; however, for the dry trial it shows a trend approximately following a friction damped system. The conclusion of these results is that a combination of both viscous and friction damping exist for the model and thus both need to be included in the EOM when creating a numerical model of this bridge superstructure.

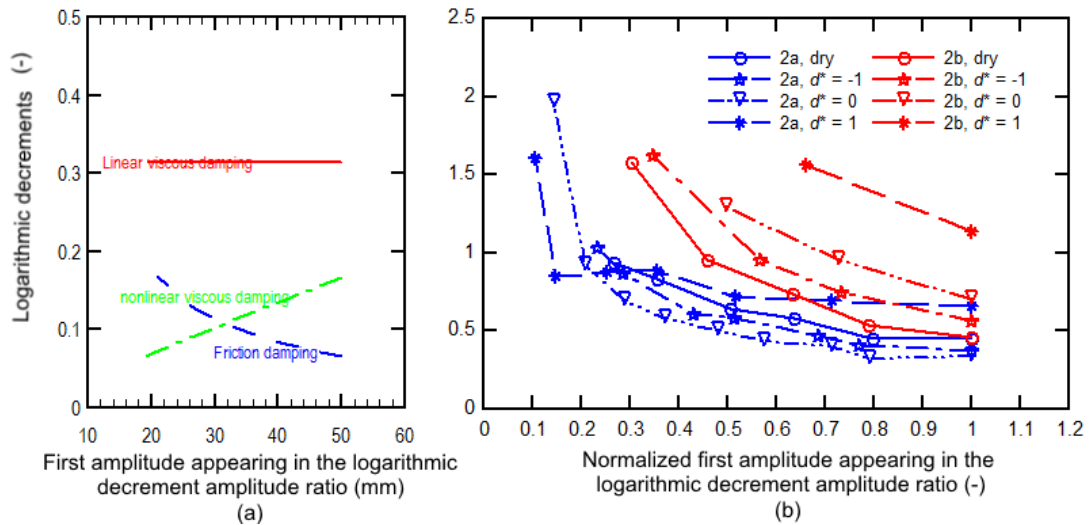


Figure 2.4. Comparison of logarithmic decrements for (a) theoretical values for three different types of damping following [26] and (b) free vibration tests from large-scale bridge superstructure model. The terminology in legend detailed in Table 1.

2.5 Analysis

After studying the damping characteristics exhibited by the bridge model, this section presents the relevant equation of motion (EOM), which is the first step for analysis. Subsequently, the optimization scheme used to estimate the dynamic parameters for the system is presented.

2.5.1 Numerical Model

The classic fourth-order Runge-Kutta (RK) numerical method [29] was implemented in this study to solve the SDF equation of motion (EOM) for free vibration of the large-scale experiment presented in [2]. Appendix A provides the details of the implemented method along with a test for code verification. Based on the findings presented in Section 4, the free vibration EOM implemented in this study considers two types of damping forces simultaneously, viscous and friction damping, as follows:

$$m \cdot \ddot{x} + c \cdot \dot{x} + F \cdot \text{sign}(\dot{x}) + k \cdot x = 0 \quad 2.1$$

where m , c , and k represent mass, viscous damping coefficient, and stiffness constant of the SDF system, F is the friction force, and \ddot{x} , \dot{x} , and x are acceleration, velocity, and displacement of the mass, respectively. Analytical solutions for the steady-state response of a similar system excited with a harmonic force and assuming a small friction force with no standstill regions were first presented by Den Hartog [30] using a closed-form non-continuous solution. In other words, two solutions based on the velocity sign, i.e. when $\dot{x} > 0$ and $\dot{x} < 0$, were used. Den

Hartog presented the solutions for several damping ratios as a function of the amplification factor vs. frequency ratio with a discussion of the regions when motion would or would not stop. Perls and Sherrard [31] extended Den Hartog's work for a wider range of damping ratios. Cheng and Zu [32] presented a different analytical solution for the steady-state response of a system with combined viscous and friction damping mechanisms subjected to two excitation forces with different frequencies. Like Den Hartog, Cheng and Zu presented a discontinuous solution due to discontinuities in the friction force function. Moreover, they discussed two cases of motion behavior: when the motion is assumed not to have a stopping region and when the motion experiences one stop. Feeny and Liang [33] presented a methodology to quantify the damping coefficients for a system with combined viscous and friction damping, assuming linearity of the system. This led them to assume a linearly decreasing behavior for the successive extremes of the displacement response, known as the displacement decrement identification method. However, as was observed earlier in the logarithmic decrement analysis, the decrement was not linear due to the nonlinearity of the system. Liang [34] extended the previous work to identify the damping parameters from the acceleration response, which they refer to as the acceleration decrement identification method. Both methods are based on the discontinuous form of the friction force function. Stanway and Mottershead [35] presented a numerical comparison between three least-squares techniques to identify the damping coefficient for a defined system using a continuous friction force function, by assuming a constant friction force with a magnitude that is altered based on the

sign of velocity. This representation was modeled by introducing the term $F \cdot \text{sign}(\dot{x})$. Finally, Mostaghel and Davis [36] suggested additional continuous functions to represent the friction force-sliding velocity function. In this study, the authors used the term $F \cdot \text{sign}(\dot{x})$ to represent the Coulomb friction damping force, as previously described in [35], since, based on [36], it showed an instantaneous phase change rather than any of the other presented functions. In addition, stop motion behavior was not observed in the experimental results.

2.5.2 Parameter Estimation

Since the main objective of this study was to characterize the dynamic properties associated with the effects of water submersion on the free vibration response of the laboratory model, the unknown and most important parameters to be estimated are: (a) viscous damping coefficient and (b) friction force. System mass and stiffness could be directly computed from the experimental data [2]. Estimating (a) and (b) represents a classic inverse problem [37] where the unknown input and known output parameters are the initial displacement as well as level of submersion and the displacement response, respectively. The unknown input parameters were obtained by varying them in the numerical model and maximizing the correlation coefficient between the two responses. Using MATLAB 2017b [38], two methods were implemented for this optimization process. The first one is referred to as “manual looping” where suitable ranges and increments for each model parameter (e.g. damping ratio or friction force) were determined based on the experimental results. By looping over these values, the best set of

parameters was found by maximizing the correlation coefficient between experimental and numerically predicted vibration responses. The second method is referred to as “global search” and utilizes a MATLAB built-in function called `GlobalSearch`, which is a solver for optimization problems, e.g. to find a single global minimum based on a user-defined objective function. The total absolute error criteria was used to find the best-fit parameters. `GlobalSearch` operates a local solver, `fmincon`, which is designed to find solutions near the starting point using a gradient-based method. Since the solution from this approach can be influenced by the starting point itself, a heuristic approach was implemented whereby multiple random starting points are employed to avoid the final solutions being associated with a local minima.

Both methods were validated by first simulating a number of vibration responses using a range of input parameters with the numerical approach described in Section 5.1. The two optimization schemes were then used on these simulated responses to estimate the input parameters. `Globalsearch` was able to match the assumed input parameters with a maximum error of 1.9% where manual looping led to larger errors (up to 11%) due to the finite increments required by the method. Detailed results of this validation are provided in Appendix B.

Three levels of optimizations were initially evaluated using the two methods with an increasing number of parameters to be estimated:

1. First level: damping ratio, ζ and friction force, F (two variables)
2. Second level: mass, m damping ratio, ζ , and friction force, F (three variables)

3. Third level: stiffness, k , mass, m , damping ratio, ζ , and friction force, F (four variables)

While the second and third level optimizations usually produced results, the objective functions for these two cases was likely relatively flat, leading to unreasonable results for some of the trials. Thus, the optimization was ultimately only performed for the first level, i.e. estimating damping ratio, ζ and friction force, F . For the manual looping method, the range of values for the viscous damping ratio was set at 0 to 20% with 0.5% increments. For the friction force, the range was set at 0 to 500 N using 10 N increments. The global search method uses a scatter-search mechanism using the same ranges but without predefined increments.

The spring stiffness, k , was computed for each trial as the slope from a linear least squares regression on the force vs. displacement response taken when the specimen was pulled to the initial displacement prior to release. Force and displacement were measured with the horizontal load cell (LC) and the displacement sensor labeled in Figure 2.1. An example force vs. displacement response for Trial 2303 is shown in Figure 2.5 along with the mean prediction line from the linear regression.

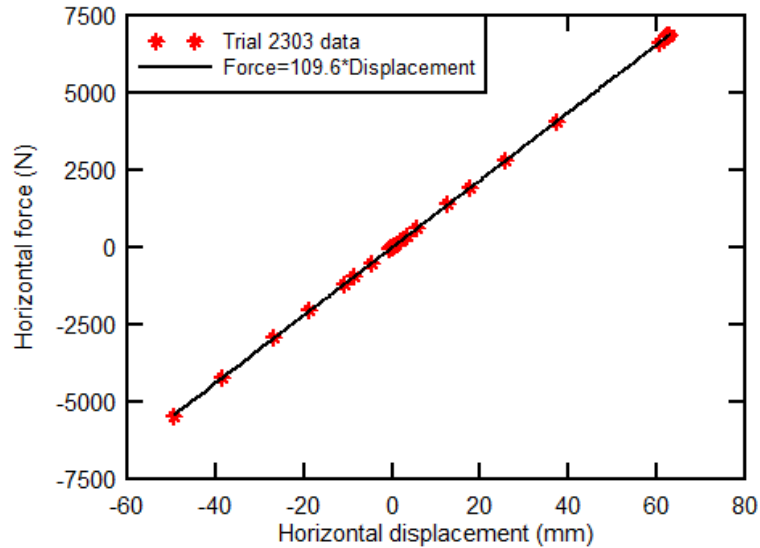


Figure 2.5. Example force - displacement response of model with mean prediction line from linear regression (Trial 2303, 3rd water level with soft springs).

Using k , and assuming that damping in the range considered does not change the natural frequency, along with the computed natural vibration frequency, f_n (obtained from Table 2.2), the total vibrating mass, m could be estimated using the following equation:

$$m = k / (2 \cdot \pi \cdot f_n)^2 \quad \mathbf{2.2}$$

The natural vibration frequencies of the dry trials were considered reference values. Subsequent trials had higher water levels that produced added mass on the system. Added mass, m_d , is defined as the difference between the total vibrating mass computed from Eq. 3 and the reference mass, m computed in the dry trials. Section 2.6 contains a detailed discussion of the added mass concept and its use.

The results from the global search method were chosen for further use in the study because they were more consistent and not bound to the values defined by the fixed increments used in the manual looping search method. The estimated parameters for all trials and both phases (medium and soft springs) determined from the global search method are shown in Table 2.3. Mean, standard deviation, and coefficient of variation (CV) for both stiffness and initial (dry) mass are also reported here.

Table 2.3. Parameter estimates for all test trials obtained from the global search method.

Trial #	Phase 2a (medium springs)						Phase 2b (soft springs)					
	k (kN/m)	m (kg)	m_d (kg)	ζ	F (N)	R^2	k (kN/m)	m (kg)	m_d (kg)	ζ	F (N)	R^2
Dry	449.2	2,458	-17	0.043	238	0.988	109.6	2,433	0	0.048	274	0.995
Dry	447.3	2,448	0	0.046	161	0.995	109.4	2,429	0	0.048	250	0.996
Dry	450.4	2,465	0	0.039	168	0.994	109.5	2,431	0	0.043	311	0.993
-1	444.1	2,430	0	0.040	174	0.991	109.6	2,433	0	0.059	254	0.995
-1	445.0	2,435	0	0.046	134	0.995	109.5	2,431	0	0.047	375	0.994
-1	447.7	2,450	0	0.037	162	0.995	109.9*	2,406	0	0.110	170	0.993
0	445.2	2,436	44	0.051	107	0.990	109.7	2,436	35	0.055	248	0.991
0	446.7	2,444	44	0.042	126	0.991	109.5	2,431	35	0.073	226	0.996
0	448.0	2,452	53	0.044	113	0.994	109.6	2,433	35	0.073	228	0.994
1	444.6	2,433	602	0.101	58	0.995	109.6	2,433	1111	0.106	311	0.993
1	444.1	2,430	637	0.097	58	0.996	109.7	2,436	1112	0.117	271	0.995
1	442.9	2,424	648	0.092	75	0.995	109.7	2,436	1112	0.089	388	0.993
Mean	446.3	2,442					109.6	2,433				
STD	2.2	12.1					0.1	2.3				
CV	0.49%	0.50%					0.09%	0.10%				

*This result was considered an outlier and thus excluded from the analysis.

The values in Table 2.3 show an increasing trend for added mass and hydroviscous damping with increasing water level, i.e. with greater submersion. This corresponds to the findings of [25] that as the fundamental vibration period

increases the added mass should decrease. One additional note is that the values presented as hydroviscous damping are not net values, rather they contain the initial structural viscous damping component. In other words, the inherent viscous damping of the structure in air is included in the values presented in Table 3 as hydroviscous damping.

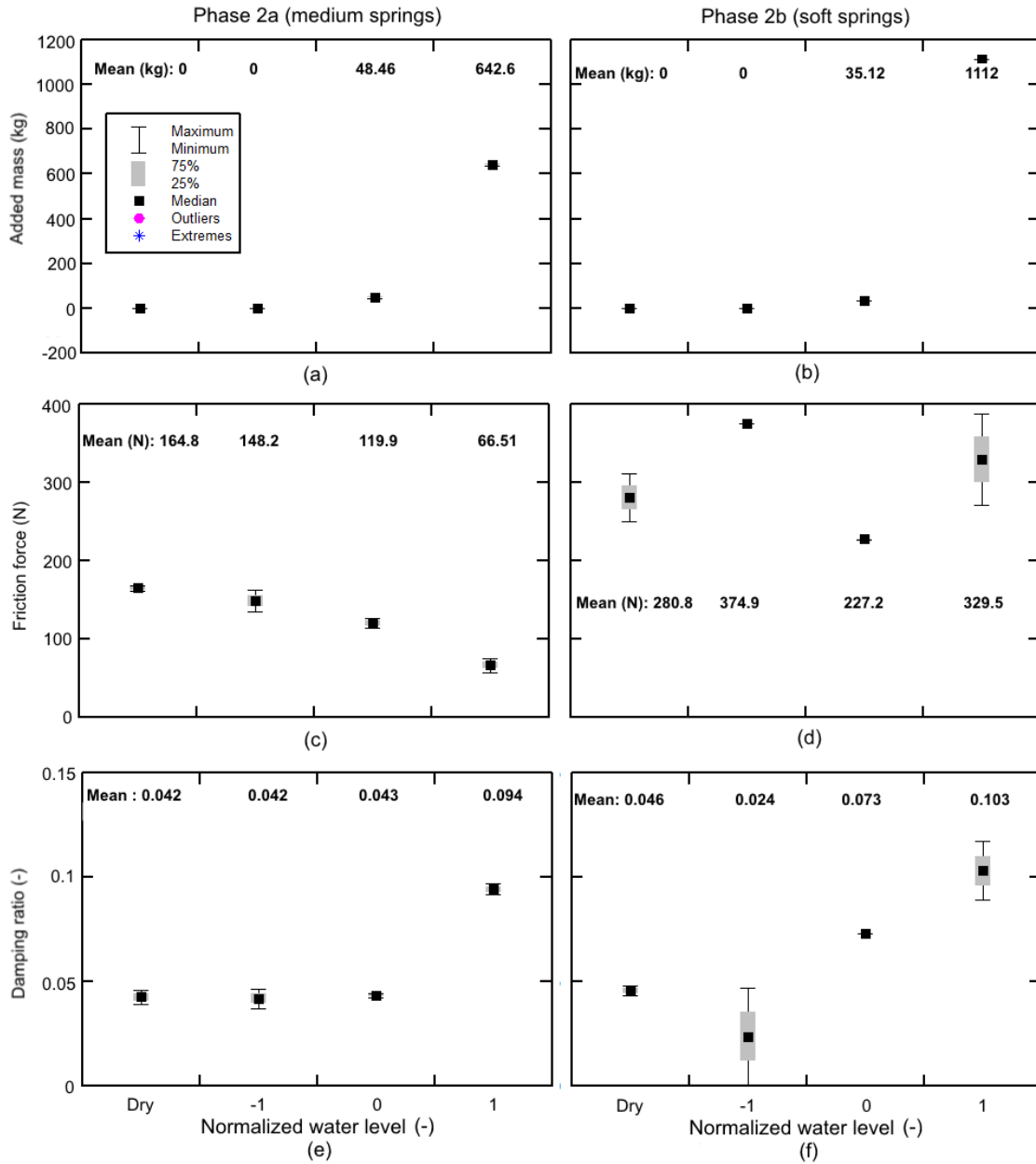


Figure 2.6. Box-and-whisker plot for the estimated parameters as a function of water level with median based estimation. Also shown are numerical values for the means.

Figure 2.6 shows box-and-whisker plots for the estimated values of added mass, hydroviscous damping, and the friction force (values taken from Table 2.3). The friction force does not exhibit a specific trend for the soft springs setup (Phase

2b), although the range of these values fall within the observed sliding friction values as found previously [23]. On the other hand, for the medium springs setup (Phase 2a), the friction force decreases with increasing water level, which would be expected. Moreover, the Phase 2b setup shows larger friction forces compared to those of the Phase 2a setup. As was observed in the logarithmic decrement analysis, the medium springs setup showed a more viscously damped behavior while the soft spring setup exhibited a more frictionally damped behavior. This may explain why the friction force for the medium springs setup was smaller compared to the values for the soft springs setup. To gain deeper insight into the combined effects of these parameters, a parametric study was performed and is presented in Appendix C.

Figure 2.1 provides a comparison between the experimental results and the numerical solutions using the dynamic parameters found by the optimization procedure. Also shown are the values for added mass, damping ratio, friction force, and the coefficient of determination, R^2 between the two curves for each of the selected trials. As can be observed, the two curves are almost identical, visually demonstrating the ability of the optimization scheme to accurately estimate the dynamic parameters from the free vibration trials.

Through the additional observations made from a parametric study (refer to Appendix C) it became evident that added mass and damping ratio are substantially influenced when the model was fully submersed. It had been argued in some studies that the added mass effect is more significant than the effect due to damping [26]. However, this argument depends on how the level of significance

is defined. In this study, both parameters play important roles in the dynamic response of the test specimen alongside with the effect of friction damping. For these experiments, the damping ratio ranged on average between 4.2 to 9.7% for the medium springs setup (Phase 2a) and 4.6 to 10.5% for the soft springs setup (Phase 2b). Added mass reached a value of 648 kg (26.6% of the dry mass) for the medium springs setup and 1,112 kg (45.6% of the dry mass) for the soft springs setup. Recall that the total mass of the superstructure model under dry conditions is approximately 2,440 kg. The dynamic characteristics, i.e. added mass and hydroviscous damping, appeared to have a greater effect for the soft springs setup. In other words, for flexible substructures the added mass and damping should be expected to be larger than for stiffer substructures.

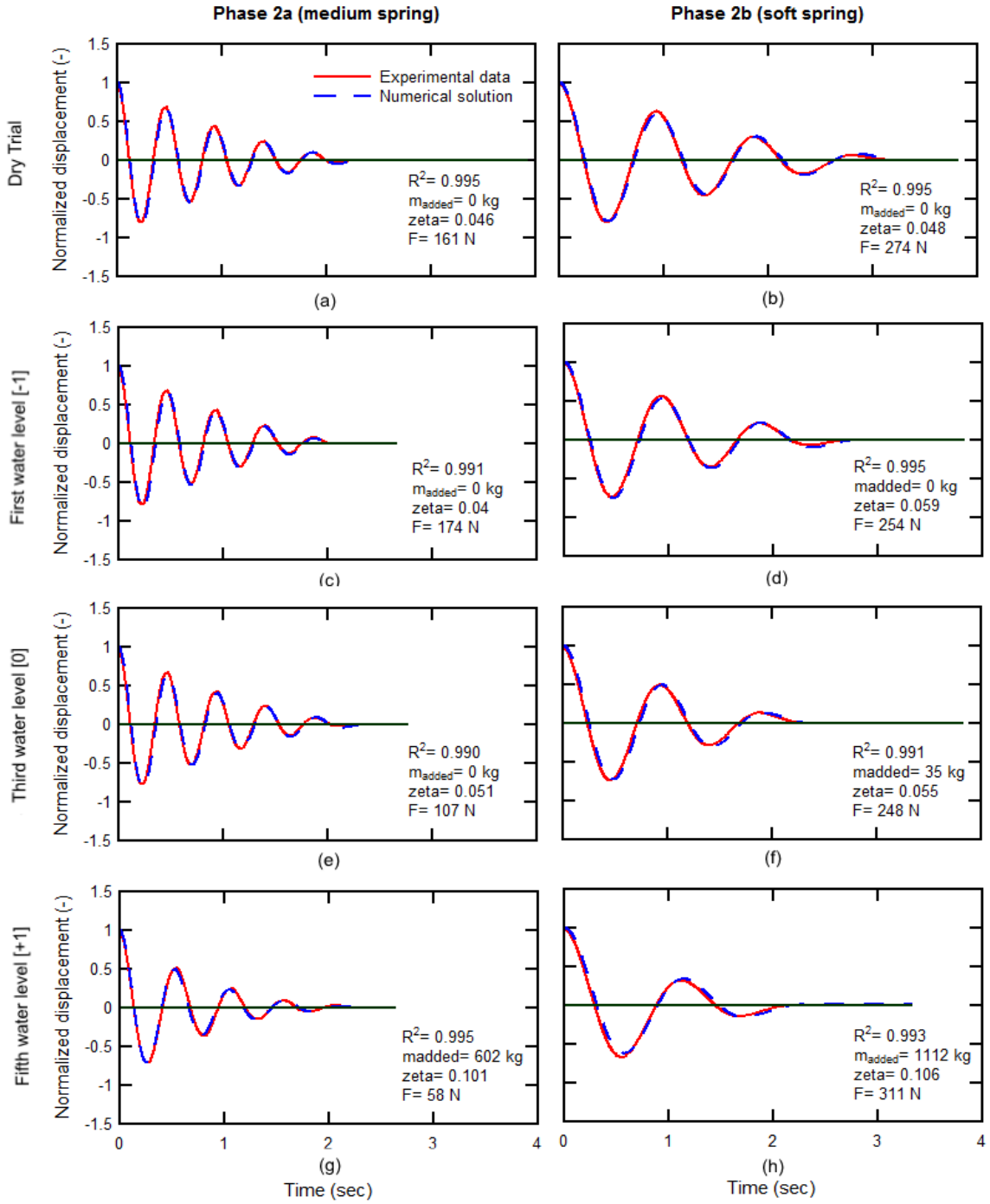


Figure 2.7. Comparison between experimental data and numerical model for Phase 2a (medium springs setup) and 2b (soft springs setup) for select trials and water levels. Also listed are the numerical values of the estimated parameter values.

2.6 Quantification of Added Mass Parameters

In this section, the concept of added mass is discussed in further detail. When defining added mass, m_d , and considering only the fully submerged case, there are two parameters that can be computed. The first one is the added mass factor, α , which is the ratio between added mass, m_d and actual (or dry) mass, m , and can be computed as [25]:

$$\alpha = (f_a/f_w)^2 - 1 \quad 2.3$$

$$m_d = m \cdot \alpha \quad 2.4$$

where f_a and f_w are the natural vibration frequency of the structure in air and water (fully submerged). The second parameter is referred to as added mass coefficient, C_m , which is defined as follows [26]:

$$C_m = m_d/m_{ref} \quad 2.5$$

where m_{ref} is a reference fluid (or displaced fluid) mass defined as the mass of a cylinder of fluid with a diameter equal to the dimension perpendicular to the direction of motion as illustrated in Figure 2.8. This reference mass can be computed as follows:

$$m_{ref} = \left[\rho_{water} * L * 2\pi * \left(\frac{D}{2}\right)^2 \right] \quad 2.6$$

where $\rho_{water} = 1000 \text{ kg/m}^3$ (freshwater was used for this study), and L and D are the total width and depth of the structure perpendicular to the flow motion.

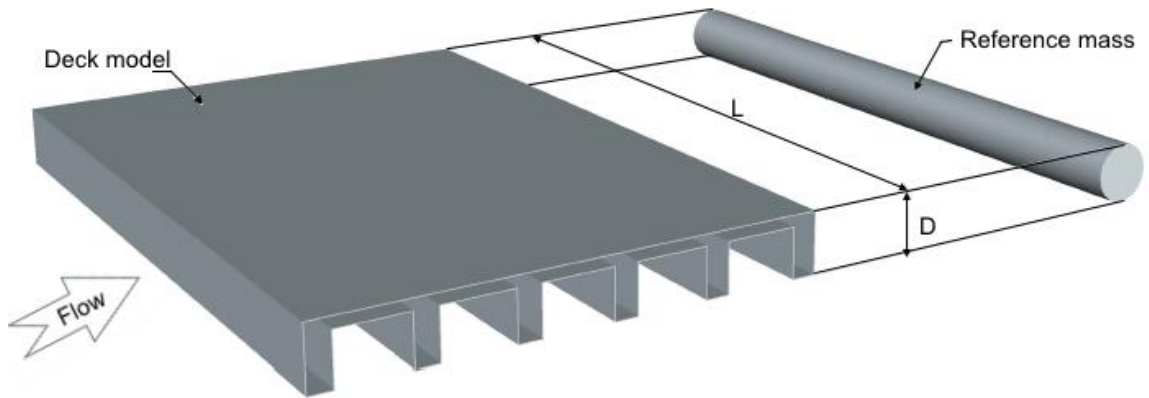


Figure 2.8. Parameters for the computation of the reference mass, m_{ref} .

For the case of partial submersion, the method of calculating the added mass parameters differs as discussed in [25]. Also, because of the limitation in the available data, the computation for the partially submerged cases is not addressed here. Moreover, the analyzed data represent only one type of geometry, i.e. a concrete deck-girder bridge superstructure with six girders. Both the geometric limitation as well as the lack of partial submersion trials are considered for a future study. As observed earlier, the structural stiffness influenced the added mass factor and coefficient values. Table 2.4 presents the calculated values for the added mass factor and the added mass coefficient for both test spring setups.

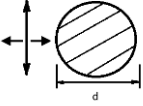
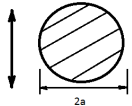
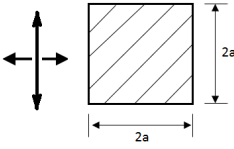
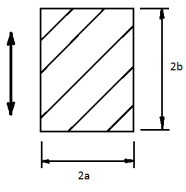
Table 2.4. Added mass factors and added mass coefficients calculated for both setups in fully submerged condition, 2a (= medium springs) and 2b (= soft springs)*.

	Added mass factor		Added mass value, kg		% of added mass from actual mass	Added mass coefficient	
Phase 2a	α_{2a}	0.262	$m_{d,2a}$	639	26%	$C_{m,2a}$	3.01
Phase 2b	α_{2b}	0.456	$m_{d,2b}$	1113	46%	$C_{m,2b}$	5.23

* $m_{ref} = 212.4\text{kg}$, $m_{actual (dry)} = 2440\text{kg}$

From the results of Table 2.4, the added mass coefficient can be interpreted as follows: the hydrodynamic force acting on the cylinder is approximately 3.0 times the mass of fluid displaced times the acceleration of the flow for the medium springs case, and 5.2 times the mass of fluid displaced times the acceleration of the flow for the soft springs case. Table 2.5 reports a sample of the added masses presented in [26], [39] for two cross sectional shapes: circle and rectangular, and along three directions of excitations: one vertical (heave) and two horizontal (surge, and sway) motions. It can be observed, for example, that in the vertical motion, as the ratio of the side perpendicular to the movement direction (dimension “a” in Table 2.5) to the side parallel to it increases, the added mass (hydrodynamic mass) per unit length decreases. Comparing the two motion cases, added mass seems to have the same magnitude. For the bridge specimen tested in this study, the ratio was 0.144, therefore, the added mass coefficient is expected to be between 1.98 and 2.23. The results from the present study show substantially higher added mass compared to the reference values: 3.01 (1.35 times higher than 2.23 reference) for the medium springs setup and 5.23 (2.35 times higher than 2.23 reference) for the soft springs setup. Since the bridge deck specimen contained chambers between the girders, which play as additional spaces for water to fill in, that will contribute to increasing the observed added mass compared to that for a solid structure. The large difference between the medium springs and soft springs setups demonstrates how the substructure stiffness can strongly influence the added mass.

Table 2.5. Hydrodynamic mass per unit length for circular and rectangular sections.

Section through body	Translational direction	Hydrodynamic mass per unit length
	Horizontal ^{*,1} (surge) (sway)	$m_{addsurge} = 1 \cdot \pi \cdot \rho \cdot d^2$ $m_{addsway} = 1 \cdot \pi \cdot \rho \cdot d^2$
	Vertical ² (heave)	$m_{add} = 1 \cdot \pi \cdot \rho \cdot a^2$
	Horizontal ¹ (surge) (sway)	$m_{addsurge} = 1.51 \cdot \pi \cdot \rho \cdot a^2$ $m_{addsway} = 1.51 \cdot \pi \cdot \rho \cdot a^2$
 <div style="display: inline-block; vertical-align: middle; margin-left: 10px;"> $a/b = \infty$ $a/b = 10$ $a/b = 5$ $a/b = 1$ $a/b = 1/5$ $a/b = 1/10$ </div>	Vertical ² (heave)	$m_{add} = 1 \cdot \pi \cdot \rho \cdot a^2$ $m_{add} = 1.14 \cdot \pi \cdot \rho \cdot a^2$ $m_{add} = 1.21 \cdot \pi \cdot \rho \cdot a^2$ $m_{add} = 1.51 \cdot \pi \cdot \rho \cdot a^2$ $m_{add} = 1.98 \cdot \pi \cdot \rho \cdot a^2$ $m_{add} = 2.23 \cdot \pi \cdot \rho \cdot a^2$

* m_{add} represent the added mass, 1: Ref. [37], 2: Ref. [24].

2.7 Summary and Conclusions

In this study, the dynamic response of a highway bridge superstructure model was investigated using free vibration tests under varying degrees of submersion to characterize the salient dynamic properties required for numerical modeling of structural responses for fluid loading. In addition to varying water levels, the substructure flexibility was also varied by inserting two sets of springs with different stiffnesses into the experimental test setup. Friction force was integrated into the equation of motion (EOM) to accurately capture the behavior of the model. The dynamic response of the bridge model was significantly affected

by the level of submersion and substructure stiffness, resulting in different values for damping and added mass. Consequently, these values (for damping and added mass) affect the forces experienced on the structure and transmitted to connections during highly-transient wave loading.

Numerical responses were generated by solving the EOM for a single degree of freedom (SDF) mass-spring-damper system with combined viscous and Coulomb friction damping via the classical 4th order Runge-Kutta numerical method. An optimization scheme was used to estimate the dynamic properties of the system, such as damping coefficient and friction force, by maximizing the correlation coefficient between the observed and numerically simulated vibration responses for each test trial. Based on the estimated parameters, the following observations were made:

1. The natural vibration frequency of the bridge superstructure model decreases with increasing water level (or submersion). In other words, the added mass increases with increasing water level and for softer substructure stiffness. This demonstrates that dynamic fluid-structure responses are influenced by substructure stiffness.
2. Damping increases with increasing water level.
3. Dynamic fluid-structure responses are influenced by substructure stiffness. Both added mass and damping coefficients were affected by the stiffness of the substructure. Added mass and damping increased for the reduced stiffness substructure.

4. The friction force, for the soft springs setup, stayed within the sliding friction limits discussed in [2]. However, for the medium springs setup, the friction force values were less than the sliding value limit and tended to decrease as the water level increased.

The substructure flexibility was observed to influence the free-vibration dynamic response of the model bridge when submersed in water. A properly developed EOM is required to capture the bridge model response and it must include the salient dynamic properties. Added mass and damping are important factors for interpretation and understanding of fluid-structure response and can be used as explanatory parameters in subsequent regression analyses.

2.8 References

- [1] I. N. Robertson, H. R. Riggs, S. C. Yim, and Y. L. Young, "Lessons from Hurricane Katrina Storm Surge on Bridges and Buildings," *J. Waterw. Port Coast. Ocean Eng.*, vol. 133, no. 6, pp. 463–483, Nov. 2007, doi: 10.1061/(ASCE)0733-950X(2007)133:6(463).
- [2] C. Bradner, T. Schumacher, D. Cox, and C. Higgins, "Experimental setup for a large-scale bridge superstructure model subjected to waves," *J. Waterw. Port Coast. Ocean Eng.*, vol. 137, no. 1, pp. 3–11, 2010.
- [3] G. Cuomo, M. Tirindelli, and W. Allsop, "Wave-in-deck loads on exposed jetties," *Coast. Eng.*, vol. 54, no. 9, pp. 657–679, 2007.
- [4] S. Douglass, Q. Chen, and J. Olsen, "Wave Forces on Bridge Decks Draft Report," *Coast. Transp. Eng. Res. Educ. Cent. Univ. South Ala.*, 2006.
- [5] M. Hayatdavoodi, B. Seiffert, and R. C. Ertekin, "Experiments and computations of solitary-wave forces on a coastal-bridge deck. Part II: Deck with girders," *Coast. Eng.*, vol. 88, pp. 210–228, 2014.
- [6] R. L. McPherson, "Hurricane induced wave and surge forces on bridge decks," PhD Thesis, Texas A & M University, 2010.
- [7] B. Seiffert, M. Hayatdavoodi, and R. C. Ertekin, "Experiments and computations of solitary-wave forces on a coastal-bridge deck. Part I: Flat plate," *Coast. Eng.*, vol. 88, pp. 194–209, 2014.
- [8] D. Istrati, "Large-Scale Experiments of Tsunami Inundation of Bridges Including Fluid-Structure-Interaction," PhD Thesis, 2017.

- [9] P. Kaplan, J. J. Murray, and W. C. Yu, "Theoretical analysis of wave impact forces on platform deck structures," American Society of Mechanical Engineers, New York, NY (United States), 1995.
- [10] P. Kaplan, "Wave impact forces on offshore structures: re-examination and new interpretations," in *Offshore Technology Conference*, 1992.
- [11] J. Marin and D. M. Sheppard, "Storm surge and wave loading on bridge superstructures," in *Structures Congress 2009: Don't Mess with Structural Engineers: Expanding Our Role*, 2009, pp. 1–10.
- [12] Q. Chen, L. Wang, and H. Zhao, "Hydrodynamic investigation of coastal bridge collapse during Hurricane Katrina," *J. Hydraul. Eng.*, vol. 135, no. 3, pp. 175–186, 2009.
- [13] D. James, J. Cleary, and S. Douglass, "Estimating Wave Loads on Bridge Decks," in *Structures Congress 2015*, 2015, pp. 183–193.
- [14] G. Xu and C. S. Cai, "Wave forces on Biloxi Bay Bridge decks with inclinations under solitary waves," *J. Perform. Constr. Facil.*, vol. 29, no. 6, p. 04014150, 2014.
- [15] A. Guo, Q. Fang, X. Bai, and H. Li, "Hydrodynamic experiment of the wave force acting on the superstructures of coastal bridges," *J. Bridge Eng.*, vol. 20, no. 12, p. 04015012, 2015.
- [16] J. Jin and B. Meng, "Computation of wave loads on the superstructures of coastal highway bridges," *Ocean Eng.*, vol. 38, no. 17–18, pp. 2185–2200, 2011.
- [17] J. Marin and D. M. Sheppard, "Storm surge and wave loading on bridge superstructures," in *Structures Congress 2009: Don't Mess with Structural Engineers: Expanding Our Role*, 2009, pp. 1–10.
- [18] "Development of the AASHTO guide specifications for bridges vulnerable to coastal storms | Request PDF," *ResearchGate*. https://www.researchgate.net/publication/299678527_Development_of_the_AASHTO_guide_specifications_for_bridges_vulnerable_to_coastal_storms (accessed Nov. 09, 2018).
- [19] X. Chen, J. Zhan, Q. Chen, and D. Cox, "Numerical Modeling of Wave Forces on Movable Bridge Decks," *J. Bridge Eng.*, vol. 21, no. 9, p. 04016055, Sep. 2016, doi: 10.1061/(ASCE)BE.1943-5592.0000922.
- [20] G. Xu and C. S. Cai, "Numerical simulations of lateral restraining stiffness effect on bridge deck–wave interaction under solitary waves," *Eng. Struct.*, vol. 101, pp. 337–351, 2015.
- [21] G. Xu and C. S. Cai, "Numerical investigation of the lateral restraining stiffness effect on the bridge deck–wave interaction under Stokes waves," *Eng. Struct.*, vol. 130, pp. 112–123, 2017.
- [22] T. Schumacher, C. Higgins, C. Bradner, D. Cox, and S. C. Yim, "Large-Scale Wave Flume Experiments on Highway Bridge Superstructures Exposed to Hurricane Wave Forces," presented at the Sixth National Seismic Conference on Bridges and Highways Multidisciplinary Center for Earthquake Engineering Research South Carolina Department of Transportation Federal Highway Administration Transportation Research Board, 2008, Accessed: Mar. 09, 2020. [Online]. Available: <https://trid.trb.org/view/1120856>.
- [23] C. Bradner, *Large-scale laboratory observations of wave forces on a highway bridge superstructure*. Oregon State University, 2008.
- [24] C. Bradner, T. Schumacher, D. Cox, and C. Higgins, "Large-Scale Laboratory Observations of Wave Forces on a Highway Bridge Superstructure," 2011.
- [25] A. R. Chandrasekaran, S. S. Siani, and M. M. Malhorta, "Virtual mass of submerged structures," *J. Hydraul. Div.*, vol. 98, no. 8923 Paper, 1972.

- [26] R. G. Dong, "Effective mass and damping of submerged structures," California Univ., Livermore (USA). Lawrence Livermore Lab., 1978.
- [27] R. J. Fritz, "The effect of liquids on the dynamic motions of immersed solids," *J. Eng. Ind.*, vol. 94, no. 1, pp. 167–173, 1972.
- [28] E. Nezirić, S. Isić, V. Doleček, and A. Voloder, "An Analysis of Damping type Influence to Vibration of Elastic Systems," 2010.
- [29] J. F. Epperson, *An Introduction to Numerical Methods and Analysis*. John Wiley & Sons, 2013.
- [30] J. D. Hartog, "LXXIII. Forced vibrations with combined viscous and coulomb damping," *Lond. Edinb. Dublin Philos. Mag. J. Sci.*, vol. 9, no. 59, pp. 801–817, 1930.
- [31] T. A. Perls and E. S. Sherrard, "Frequency response of second order systems with combined Coulomb and viscous damping," *J. Res. Natl. Bur. Stand.*, vol. 57, no. 1, p. 45, 1956.
- [32] G. Cheng and J. W. Zu, "Two-frequency oscillation with combined Coulomb and viscous frictions," *J. Vib. Acoust.*, vol. 124, no. 4, pp. 537–544, 2002.
- [33] B. F. Feeny and J. W. Liang, "A decrement method for the simultaneous estimation of Coulomb and viscous friction," *J. Sound Vib.*, vol. 195, no. 1, pp. 149–154, 1996.
- [34] J.-W. Liang, "Identifying Coulomb and viscous damping from free-vibration acceleration decrements," *J. Sound Vib.*, vol. 282, no. 3–5, pp. 1208–1220, 2005.
- [35] R. Stanway and J. E. Mottershead, "Identification of combined viscous and Coulomb friction—a numerical comparison of least-squares algorithms," *Trans. Inst. Meas. Control*, vol. 8, no. 1, pp. 9–16, 1986.
- [36] N. Mostaghel and T. Davis, "Representations of Coulomb friction for dynamic analysis," *Earthq. Eng. Struct. Dyn.*, vol. 26, no. 5, pp. 541–548, 1997.
- [37] J. C. Santamarina and D. Fratta, *Discrete signals and inverse problems: an introduction for engineers and scientists*. John Wiley & Sons, 2005.
- [38] "How GlobalSearch and MultiStart Work - MATLAB & Simulink." <https://www.mathworks.com/help/gads/how-globalsearch-and-multistart-work.html> (accessed May 19, 2018).
- [39] Techet, "2.016 Hydrodynamics _ Added Mass," .
- [40] P. J. Roache, *Verification and validation in computational science and engineering*, vol. 895. Hermosa Albuquerque, NM, 1998.
- [41] B. A. Erickson and E. M. Dunham, "An efficient numerical method for earthquake cycles in heterogeneous media: Alternating subbasin and surface-rupturing events on faults crossing a sedimentary basin," *J. Geophys. Res. Solid Earth*, vol. 119, no. 4, pp. 3290–3316, 2014.

Chapter 3

Manuscript 2: Effect of Substructure Flexibility on Wave-induced Forces on Bridge Superstructures

This manuscript is co-authored by Thomas Schumacher (adviser), Christopher Higgins, and Avinash Unnikrishnan. This manuscript is currently being prepared for submission to a journal.

3.1 Introduction and Background

A common failure mode of coastal bridges after the hurricane impacts in 2004 (Katrina) and 2005 (Ivan) was attributed to strength-deficient connections between superstructure and substructure. Once these connections had failed, wave loads were in many cases large enough to move superstructures off their substructures into the water [1], as can be observed in Figure 3.1.



Figure 3.1. Photo of superstructures of the US 90 Biloxi Bay Bridge that have been removed from their substructures by wave loads during Hurricane Katrina. Source [2].

Prior to the hurricane events in the early 2000s, it was thought that the superstructure's self-weight, along with shear-keys, would be sufficient to resist any hurricane-induced wave forces. The reason for the observed system failure is that the storm surge was much higher than anticipated, which lead to vertical, i.e. uplift, forces that were, in combination with the large horizontal forces, exceeding the capacity of the commonly used girder anchorage systems [3]. In many cases, no major damage was observed on the superstructures or to the substructures. Studying and providing stronger connections, i.e. anchorages, between girders and bent-caps has thus been proposed. The caveat is that stronger connections have the ability to transfer higher forces between superstructures and substructures. Therefore, it becomes necessary for the substructure to be able to carry these higher forces. Assuming the presence of anchorages that can transfer any forces, substructure flexibility is thus a factor that might significantly affect the experienced wave forces on bridge superstructures. To address these questions, Bradner et al. [4] tested a realistic 1:5-scale highway bridge model under various wave conditions experimentally. The setup is unique in that the horizontal flexibility of the substructure representing the bent columns, bent cap, and foundation, could be adjusted by inserting springs of different stiffness. The reported experiments were performed for three different substructure stiffnesses, including rigid (no springs), medium, and soft. The stiffnesses of the springs were selected based on 2D frame analyses of realistic substructure configurations [5], [6]. While some preliminary results have been reported [2], [4]–[6], no systematic analysis has been performed to date. Schumacher et al. in [2] qualitatively showed that the wave-

induced forces for a flexible setup are larger compared to a rigid setup. In [4]–[6], they showed that a second-order polynomial relationship between wave height and wave forces could be defined for both regular and random waves. Also, they addressed the effect of water level. They showed that, for the first three levels, forces were increased as water level increased. However, as the structure started to submerge until it got fully submerged, forces start to level off or even decrease. In this study, these observations are reinforced by a statistical test emphasizing the effect of substructure flexibility, besides the derivation of factors that account for this effect. Additionally, wave forces on coastal structures, particularly bridges, attracted the attention of many other researchers, who studied them experimentally [6]–[12] or numerically [13]–[20]. Through these efforts, many concepts and theories regarding wave-structure interaction dynamics have been established and equations for estimating wave forces developed. Additionally, an AASHTO guide has been developed to calculate horizontal and vertical forces, as well as overturning moment for highway bridge superstructures having a variety of girder types [21]. Most of the aforementioned research has focused on bridge systems where the substructure is assumed to be rigid horizontally. Some recently conducted numerical studies have studied the effects of horizontal fixity issue and submersion depth on the experienced forces [17], [18]. Both of these studies found that the induced wave forces increase with increasing flexibility of the structure.

Most coastal engineers use normalized features in their analyses as a way to generalize the results [22]. One advantage is that these non-dimensional

analyses help in reducing the scattering in the estimated values and provides physics-based models that are less sensitive to superior correlations [22].

For example, air trapped under a bridge deck between girders has been studied as a factor affecting the wave forces acting on an elevated coastal bridge deck [23]. The procedure for analyzing the data was to filter the collected signals using the wavelet transform of the recorded signals, and distinguish the forces' time history to have two regions: short time wave application (slamming force) and long-time wave application (quasi-static force). In their analysis, the researchers normalized the measured pressure by the static-equivalent pressure (ρgH), where ρ is water density, g is the gravitational acceleration, and H wave height, and plotted them against the hydrostatic head ($\frac{\eta-c}{h}$), where η is the wave elevation, c is the clearance between the still water level and the bottom of the structure, and h is the water depth. Hydrostatic head could be interpreted as the relative wetted area. Three distinct regions were observed in the analyzed data and they were attributed to the structural inundation level. These regions are defined as follows:

1. Hydrostatic head < 0 : rapid increase in loading
2. $0 < \text{Hydrostatic head} < 0.4$: slow increase in loading.
3. $0.4 < \text{Hydrostatic head} < 0.65$: rapid increase in loading.

Openings introduced in the deck to relief trapped air showed a decrease on the measured forces.

AASHTO [21], on the other hand, counted for this factor (air entrapment) which was defined by calculating the trapped air factor (TAF). TAF in turn was a

function of several parameters: submersion depth, bridge width, and girders depths per their specifications. This factor defines a wide rank (0 -100%) depending on the designer decision.

[7] found that vertical force was highly affected by air entrapment, and by introducing openings in the deck, the vertical forces decreased.

Using potential flow theory, Guo et al. [19] studied the behavior of forces normalized by (ρghA) vs. wavenumber ($k = 1/\lambda$) as the independent variable, with A being the area by which the wave interacts with the structure, and λ being wavelength. Two equations were derived to estimate vertical and horizontal forces. In their study they showed that the normalized vertical force experienced a dramatic decrease by an increase of wave numbers ≤ 1.0 , after this point (i.e. for wave numbers > 1.0) the vertical force decreased slowly. For horizontal force, a reversed behavior was observed. For wave number ≤ 1.0 , the normalized horizontal force increased dramatically as k increased. For $1.0 \leq k < 1.5$, the normalized horizontal force slowly increased. For $k > 1.5$, the normalized horizontal force exhibited a decreasing trend.

Using the last numerical model presented in [19], Fang et al. [20] studied the effect of incident angle on wave forces on bridge superstructures. Similarly, they employed normalized features in their analyses and showed that the perpendicular direction produces the highest wave forces. Three additional normalized parameters were studied besides the angle of action. The first one is submersion depth normalized by water depth. The other parameter was the relative thickness of the bridge, which was measured by dividing deck thickness

by the submersion depth. The third parameter was the number of girders. All three parameters were shown to affect the horizontal force, whereas they had no effect on the vertical force components.

Hayatdavoodi et. al. [24] studied the effect of solitary and cnoidal waves on a submerged horizontal deck on the normalized horizontal force, vertical force, and overturning moment (around the middle of the deck). Wave height, wave period, deck submersion, and deck width were among the studied parameters after they were normalized. Simplified empirical equations were developed based on the numerical results. Their findings can be summarized as follows:

For solitary waves:

- a. Vertical force, horizontal force, and overturning moment linearly increase with increasing wave height.
- b. Vertical force and overturning moment increase with increasing deck width. The horizontal force reaches a constant value after the deck width reaches a certain value.
- c. The level of submersion has little effect (if none) on the forces, in general.

For cnoidal waves:

- a. Forces change nonlinearly with wave height.
- b. Vertical force and overturning moment decrease with increasing level of submersion. The horizontal force remains constant after a certain level of submersion is reached.

- c. Vertical force and overturning moment increase nonlinearly with increasing deck width, whereas the horizontal force oscillates.

Finally, Park et al. [25] normalized wave forces by the incident wave energy along the shoreline and plotted them against normalized clearance by water depth, which can be thought of as relative water depth. The normalized forces by the incident wave energy is a measure of energy dissipation. Following in this study, the normalized wave forces by the incident wave energy vs. the relative width will be examined.

3.2 Motivation and Objectives

The effect of horizontal flexibility of the substructure representing bent columns, bent cap, and foundation, have not been studied sufficiently. In fact, the two studies found, i.e. [15], [17], actually contradict each other as to whether flexible support conditions lead to increased or decreased wave-induced forces. Additionally, current design guides are based on rigid substructure conditions, which from a structural engineering perspective are not realistic [21]. The motivation of the work presented in this article, which is based on the unique dataset described in [4], was to study the effect of substructure flexibility and develop force magnification factors that bridge engineers can use in conjunction with prediction equations to estimate wave forces on bridge superstructures.

3.3 Experimental Setup

The analysis presented in this article is based on data produced from a large-scale experimental research project conducted in the O.H. Hinsdale Wave Research Laboratory at Oregon State University [4]. Details of the experimental setup as well as testing protocols and some preliminary data can be found in [4], [6]. Only a brief overview of the experiment is given subsequently. Figure 3.2 shows an elevation view of the realistic 1:5-scale highway bridge superstructure model used in the experiments as well as some of the instrumentation. The three different horizontal support conditions representing three different substructure flexibilities are highlighted as well and include: Phase 1, 2a, and 2b. These correspond to rigid, medium, and soft horizontal support conditions, respectively. Numerical values are summarized in Table 3.1.

Table 3.1. Structural configurations and test phases investigated in [6] and used in this study.

Phase	Horizontal support condition	Model spring stiffness kN/m (lb/in)	Connection between model superstructure and bent cap
1	Rigid	Very large	Fixed, bolted (assumed rigid)
2a	Dynamic, medium springs	458 (2614)	
2b	Dynamic, soft springs	107 (612)	
3*	Unconstrained	N/A	None (free, held by gravity and friction)

* Data from this test phase was not used in this study.

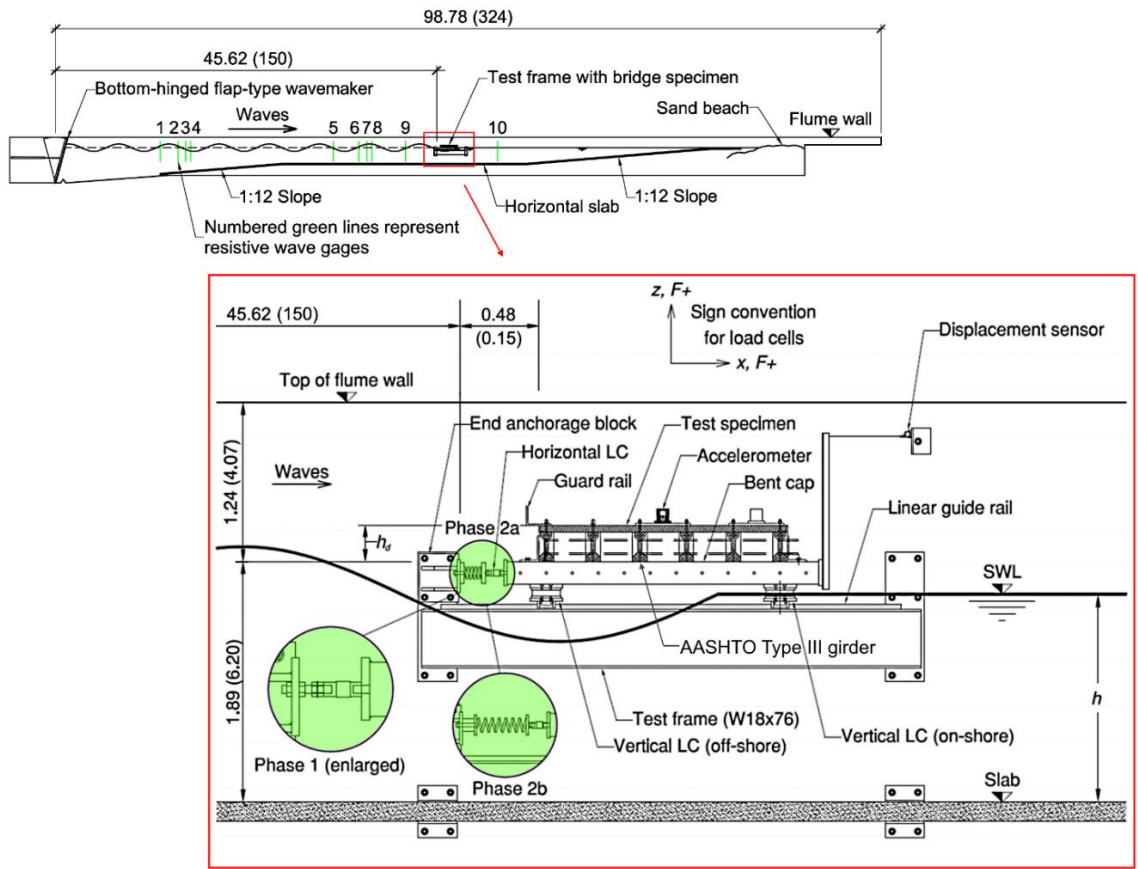


Figure 3.2. Elevation view of experimental test setup showing different horizontal support conditions, i.e. test phases (LC = load cell, SWL = still water level). Dimensions: m (ft). (Courtesy of Dr. Schumacher).

Figure 3.3 illustrates a bridge superstructure under wave action and provides commonly used terminology, which is also used herein.

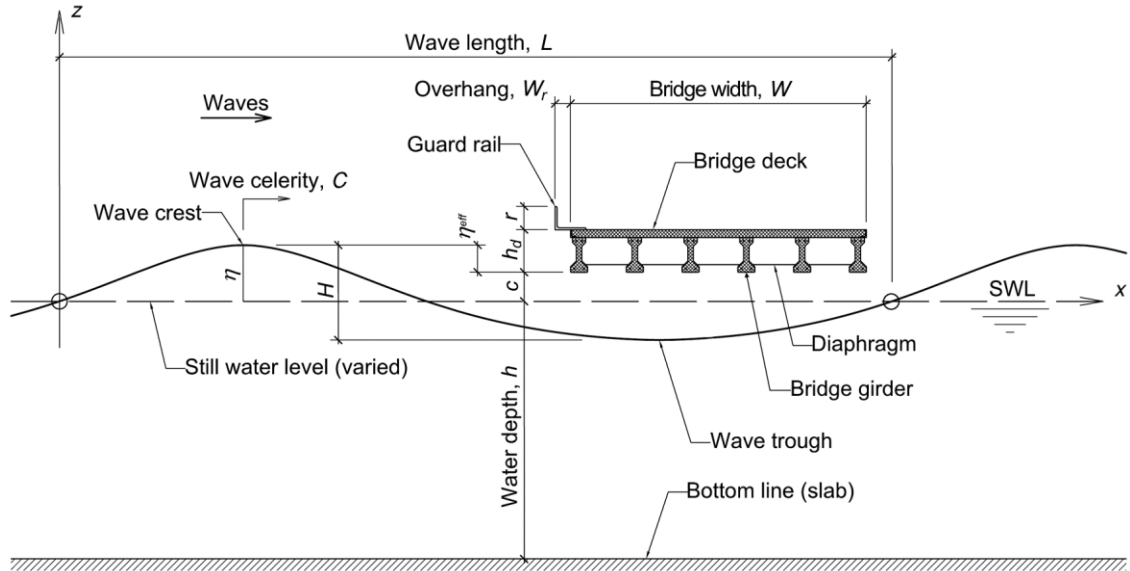


Figure 3.3. Elevation view of bridge superstructure under wave action with commonly used terminology. (Courtesy of Dr. Schumacher).

In the experiment [6], five still water levels (SWL), corresponding to depths ranging from $h = 1.61$ m to 2.17 m, were studied with increments of 0.14 m, which is equal to one-half of the total depth of the bridge superstructure, h_d . Let z_d represent the elevation of the bridge specimen measured from the bottom of the girders, which is equal to the water depth (h) plus the clearance (c). Subsequently, normalized water levels are referred to and are calculated as follows:

$$d^* = \frac{h - z_d}{h_d} \quad 3.1$$

The range of normalized depths is thus -1.0 to 1.0 with increments of 0.5. In the text we also refer to first to fifth water level, which correspond to $d^* = -1.0$ to +1.0, respectively.

Table 3.2. Studied still water levels (SWL).

Description	Water depth, h (m)	clearance, c (m)	Normalized water level d^* (-)
First water level	1.61	+0.28	-1.0
Second water level	1.75	+0.14	-0.5
Third water level	1.89	0.00	0
Fourth water level	2.03	-0.14	0.5
Fifth water level	2.17	-0.28	1.0

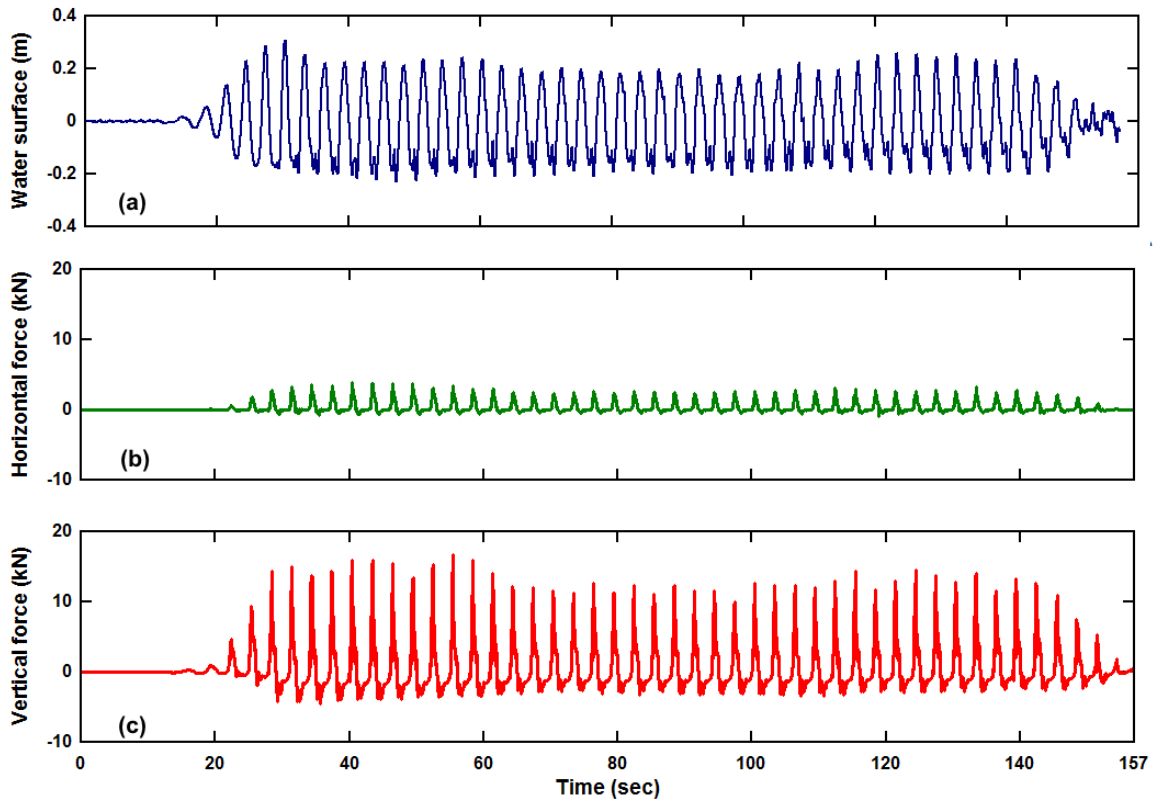


Figure 3.4. Sample experimental measurements for $d^* = 0.0$, $T = 3.0$ s, $H = 0.625$ m, Phase 1: Time histories of (a) Water level at WG 9, 4.21 m (13.8 ft) away from front face of the bridge model, (b) total horizontal force, (c) total vertical force (WG = wave gage).

Figure 3.4 shows sample measurements for a select wave trial for Phase 1 (rigid setup). Note that the total horizontal force is the summation of the two horizontal load cells measurements, whereas the total vertical force is the

summation of all four vertical load cells (two offshore and two onshore). Researchers define wave force as having two components, horizontal and vertical, that are used to identify the forces experienced by a structure. Each component has two distinct regions; positive that increases until reaching the force maximum positive value and negative that decreases until reaching the force maximum negative value. The forces that are analyzed and processed are those that capture the dynamic action of the bridge superstructure. In this article the net positive forces were considered in the analysis. Figure 3.5 shows a close-up view of sample time histories for total vertical force that show these two regions. The same can be applied for total horizontal force. Different windows were selected for each wave force time history (which corresponds to a single trial), over which the average was computed, which represented one sample measurement in the data set.

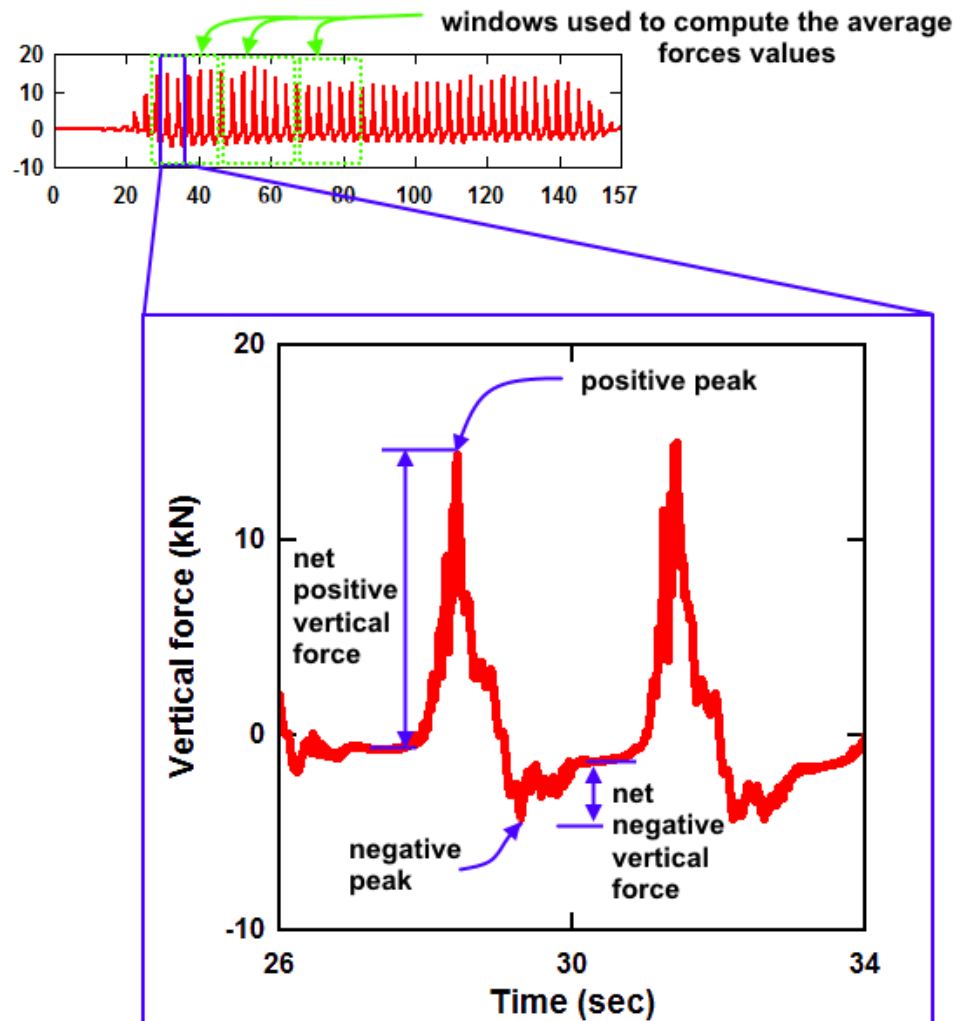


Figure 3.5. A close-up view for a sample time-history for a total vertical force due to two passing waves.

In Figure 3.6, the time histories for the fixed/rigid (Phase 1) and soft (Phase 2b) setups at the second water level ($d^* = -0.5$) with a wave period, $T = 2.5$ s for both vertical and horizontal forces are shown for comparison. As can be observed, the behavior of the horizontal wave force differs significantly between the two substructure flexibilities. For the flexible condition, besides the increase in wave force, the horizontal force is smooth and dominated by the spring stiffness,

whereas for the vertical force response, not much difference in the behavior except for a slight increase in the force magnitude can be observed.

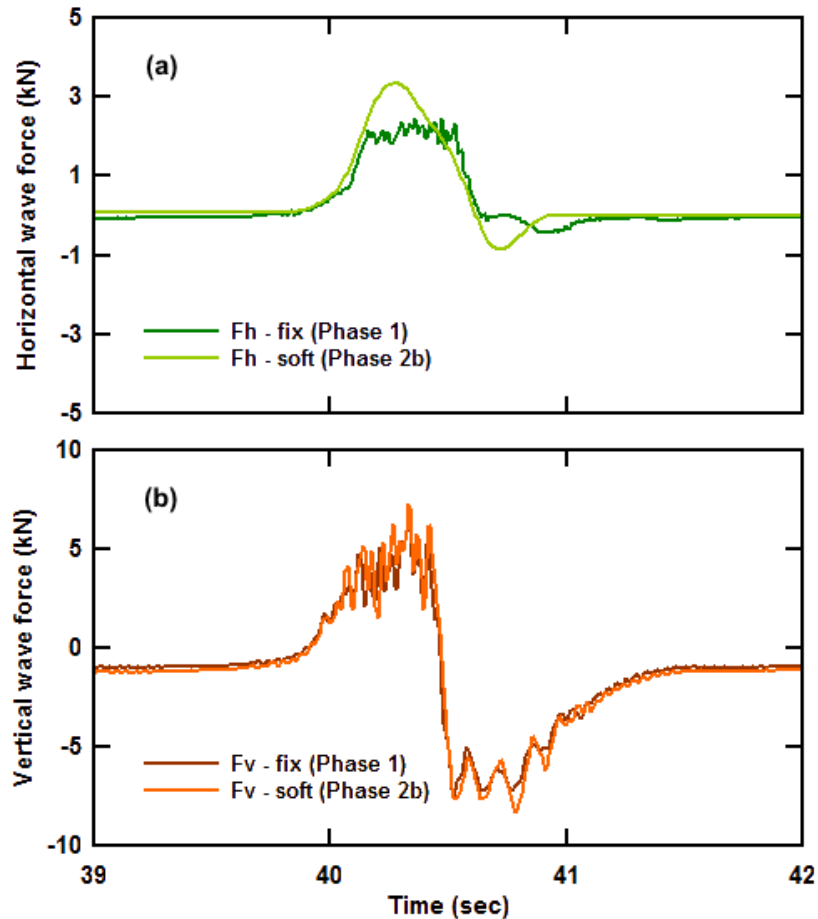


Figure 3.6. A close-up view for a sample time-history for the effect of substructure fixity on the on the observed wave force at same wave condition.

Subsequently, the effect of substructure flexibility on the forces experienced by the bridge superstructure model are analyzed and discussed through presenting parameters that the authors believe to be important in understanding and estimating wave forces. These parameters are organized in two categories: unnormalized features (parameters), and normalized features (parameters), as suggested in the literature.

3.4 Data Analysis

In this section, visualizations are done to the experimental data through presenting two categories of the commonly used parameters through the literature in defining wave forces. These categories are unnormalized and normalized features. Levels of submersion, wave height, wave steepness, and wave celerity are features presented under the unnormalized features. Normalized features analyzed include normalized forces by the incident wave energy along with the relative width.

The main point of this section is to show how substructure flexibility affects the magnitude of the induced wave forces considering these different features, set the stage for future work in building refined models that account for substructure flexibility, and provide physical interpretations for the reason why structures with flexible supports have larger forces.

3.4.1 Unnormalized feature analysis

Plotting data is an important key to depicting interesting features of possible relationships between the defined variables. As seen earlier, many parameters were believed to have an influence on the magnitude of the measured forces. In Figure 3.7, box plots of horizontal and vertical wave forces are drawn vs. normalized water level, d^* for waves with wave height, $H = 0.5$ m, and wave period, $T_p = 2.5$ s. It can be observed that both horizontal and vertical wave force components increase with increasing water level, reaching their maxima (in this

defined wave condition) at the fourth water level, i.e. at $d^* = +0.5$, when the bridge superstructure is partially submerged [14], [16], [24], [26]. After that, a drop in their magnitudes occurs when the deck is fully submerged, i.e. for $d^* = +1.0$. This can likely be attributed to the decrease in wave celerity with increasing water depth. For other wave conditions, the maximum occurred at the third water level, i.e. for $d^* = 0.0$.

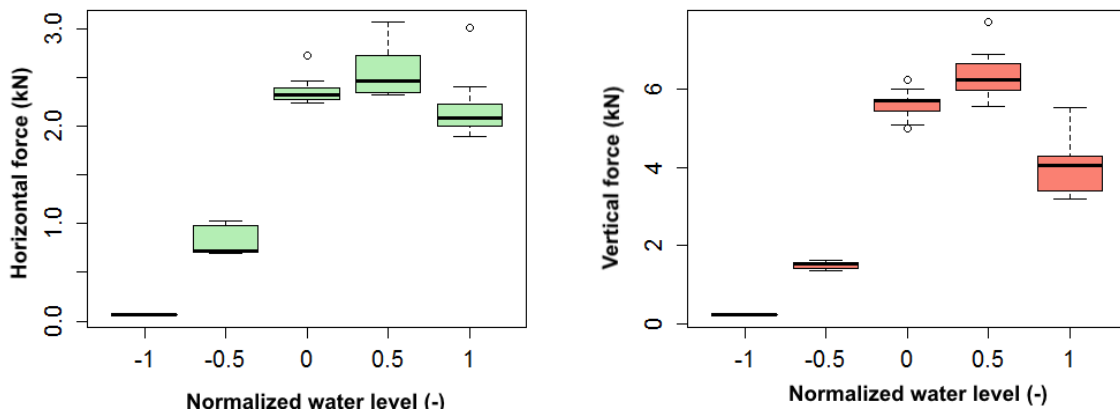


Figure 3.7. Boxplots of horizontal (left) and vertical (right) wave forces vs. normalized water level for wave height = 0.5 m and wave period = 2.5 s for rigid setup.

Substructure flexibility has not been a common subject of investigation until recently, where it has been studied through numerical modeling [15], [17], [18]. Bradner et al. [6] were the pioneers in investigating this aspect in their large-scale experimental study. In Chapter 2, a subset of the dataset used herein that captures the free vibration response of the bridge model, was analyzed to determine the dynamic properties of the experimental setup. Because of the unique experimental setup, which allows the superstructure specimen to move on top of a guardrail, an equation of motion having friction force hydrodynamic damping terms was

developed and its dynamic parameters quantified. This equation of motion is essential to build any numerical model of this particular experimental setup [5]. Some researchers who implemented numerical modeling did not consider the appropriate damping terms in their work [15], [17], [18]. As a result, inconsistencies between their results and the experimental data of [5] can be observed. As presented in [15], wave forces experienced a reduction in their magnitudes with increasing support flexibility. Contradicting this finding, [17] showed that wave forces were increasing with increasing support flexibility. To answer the question whether increasing substructure flexibility leads to increasing or decreasing wave forces, a series of plots are interpreted subsequently.

Figure 3.8 shows the behavior of wave forces vs. wave heights for different substructure flexibilities, which are shown in different symbols and colors. Normalized water depth, $d^* = +0.5$ and wave period, $T_p = 2.5$ s. Both horizontal and vertical wave forces with their mean values within a selective window of their actual response are presented. Distinct features can be observed. The forces experienced for the soft substructure flexibility are larger than those experienced for the rigid case, as proposed in [2], [17], and the difference increases linearly with increasing wave height, reaching a value of approximately 38% for a wave height of 0.58 m. Therefore, increasing substructure flexibility make a structure more susceptible to wave action, especially when the structure interferes with the water body (i.e., for partially submerged cases), putting the bridge superstructure in the maximum fluid flow field, and the surrounding water body starts to add additional mass to the moving structure. This additional mass increases the

momentum induced in the structure, which leads to increased forces experienced to be sustained by the structure. This also could be linked to the drag force. Drag force plays a role in determining the wave forces, since it is related to the projected area of interaction and wave celerity [27], [28].

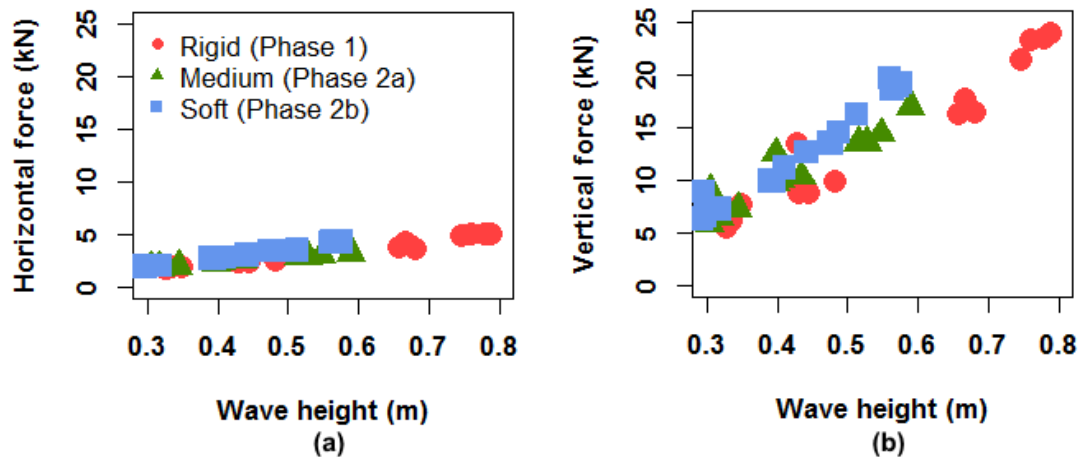


Figure 3.8. Scatter plots of (a) horizontal and (b) vertical wave forces vs. wave height. Normalized water depth, $d^* = +0.5$ and wave period, $T_p = 2.5$ s.

Appendix D shows the remaining cases of wave forces vs. wave heights for wave periods $T_p = 2, 2.5,$ and 3.0 s and for all five water levels. From these figures, it seems that the action of a wave will not be noticed until its height reaches a certain level. A positive correlation between wave forces and wave height be found, which is intuitive and has been confirmed by others [2], [4]–[6]. As water level increase, the role of wave height is more significant up to the third water level when it is starting to decline, as observed from the inclination of the line formed by the data.

Another unnormalized feature that may affect wave forces is wave steepness, which is calculated by dividing the wave height by the wavelength. Figure 3.9 depicts the relation between wave forces and wave steepness. As wave steepness increases (which an indication of wave energy increase) the induced wave forces increase as well.

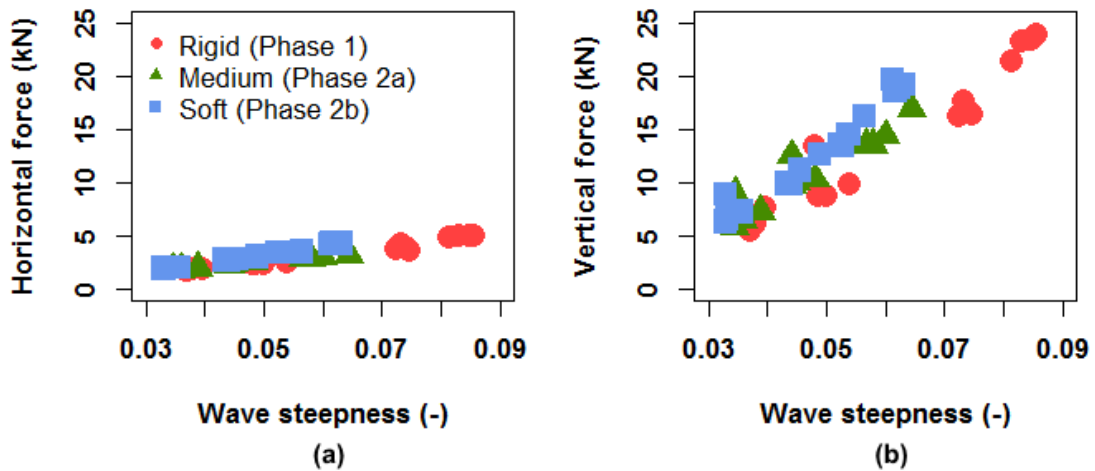


Figure 3.9. Scatter plots of (a) horizontal and (b) vertical wave forces vs. wave steepness. Normalized water depth, $d^* = +0.5$ and wave period, $T_p = 2.5$ s.

Wave celerity (or velocity) is another factor thought to be one of the important features shaping wave force magnitudes, since it is related to forces via the drag term. Again, a positive correlation can be observed between wave celerity and wave-induced forces, as visualized in Figure 3.10.

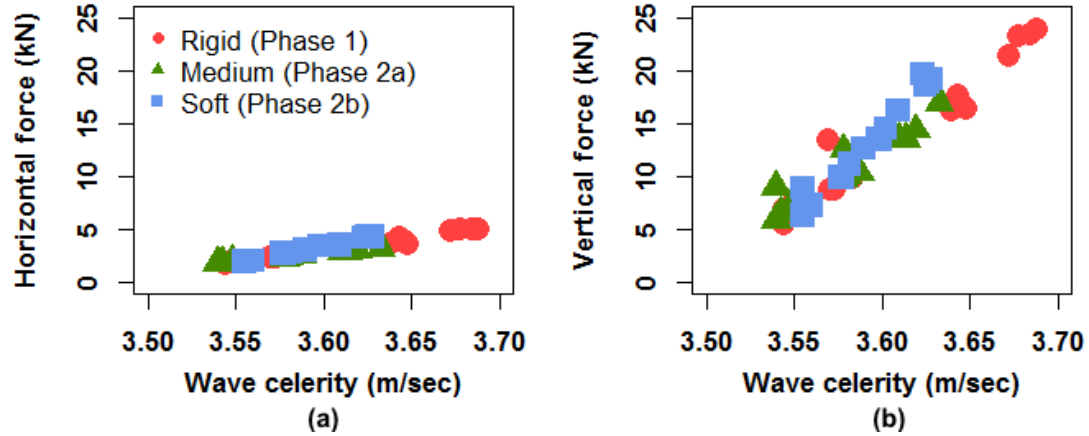


Figure 3.10. Scatter plots of (a) horizontal and (b) vertical wave forces vs. wave celerity. Normalized water depth, $d^* = +0.5$ and wave period, $T_p = 2.5$ s.

3.4.2 Normalized feature analysis

Implementing ocean engineers' practices in writing equations by normalizing features, another analysis to the data was performed and is presented in this section. As mentioned in the introduction section, normalized features can help generalizing results, and reducing the scatter in estimated values, while providing physical-based models that are less sensitive to superior correlations [22]. Following this approach, Figure 3.11 and Figure 3.12 were created and are discussed next. These figures show the normalized horizontal force by the incident wave energy ($\frac{F_h}{\rho \cdot g \cdot H^2 \cdot B}$) vs. the relative width, which is defined as the wavelength, L divided by the bridge width, W in the direction of wave action, x . B is the width of the specimen perpendicular to the wave direction. The normalized force quantity represents a measurement for the degree of relative wave energy dissipation [25]. However, this quantity can also be interpreted as a measure of the relative preserved energy. As shown in Figure 3.11(a), the data are grouped according to

wave periods, T_p with an interesting behavior of the normalized wave forces. This behavior defines an inflection point between short and long wave periods. These two regions were observed in [15] through a different comparison. In [15], they showed that for short wave periods ($T_p < 3.0$) wave celerity plays a major role, whereas for longer wave periods ($T_p > 3.0$), it plays a secondary role. This can be explained by the limitations in wave steepness, which required no wave breaking or flume overflow, therefore, wave celerity gets slower for the same wavelength as wave height decreases, and that is why we see a reduction in the energy level. As a result, for further analyses, normalized forces generated by waves with periods, $T_p = 2.5$ s are examined, as shown in Figure 3.11(b).

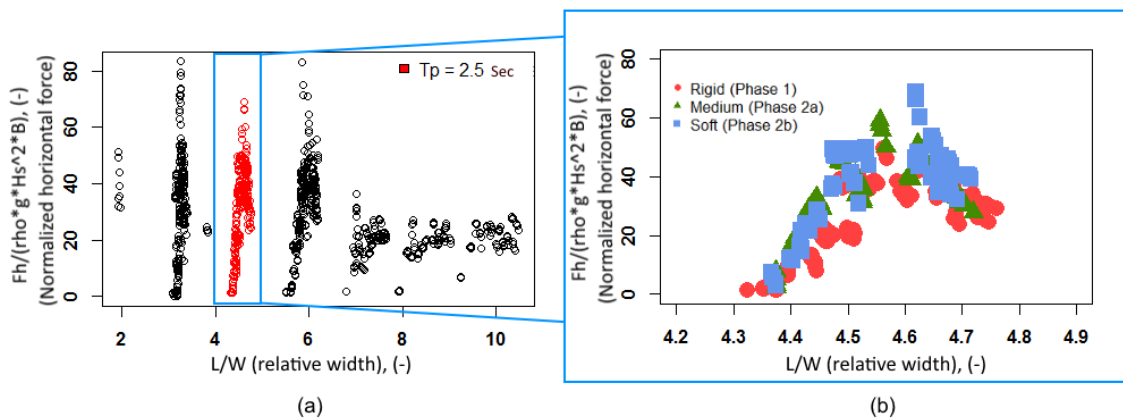


Figure 3.11. Scatter plots of normalized horizontal wave force vs. relative width.

Figure 3.11 (b) visualizes the different substructure flexibility effects on the measured forces. A more rigorous analysis is done to Figure 3.11(b) in Figure 3.12. A clear distinction between the three flexibility configurations shows that a superstructure with a flexible substructure has the least wave energy dissipation, or the highest relative energy preservation from the wave application. Additionally,

waves with wave height, $H = 0.375$ m show the highest relative energy preservation from wave action compared to other wave heights starting from the third water level. In another words, when the wave height is almost a full projection on the superstructure depth - i.e. complete wave interaction with the structure - the relative preserved wave energy by the superstructure is the highest. However, at initial water levels (the superstructure is above the still water level), as wave height increases, the more wave energy is preserved. This means wave height plays a significant role in adding more force to the structure when the superstructure is elevated. This observation reinforces the conclusion made in the previous section.

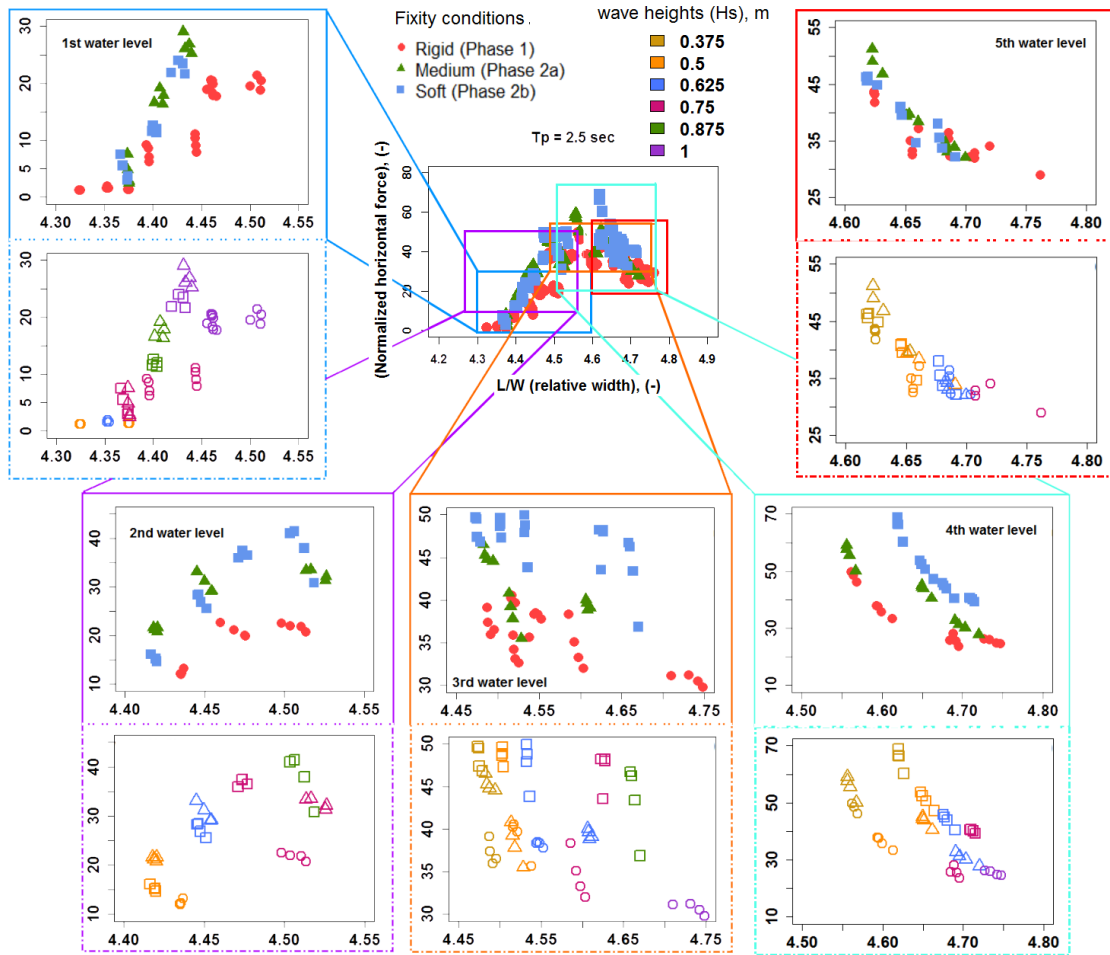


Figure 3.12. The relative energy preservation at different water levels and wave heights.

3.5 Substructure Flexibility Effect

Motivated by the strong evidence of the substructure flexibility influence on the induced wave force magnitudes, this section quantifies the amount of magnification. As suggested by [2], an anticipated quadratic relation could be observed between wave forces and wave height. Therefore, a linear least-squares first-order curve fit was used to describe the relation between the square root of wave force and wave height. The curve was forced to pass through the origin,

ensuring that zero wave height corresponds to zero force. Additional data processing prior to the regression process was needed for the first and second water levels, since at these water levels certain minimum wave heights are required to produce any wave forces. Therefore, a shift in the x-axis equal to the clearance between the still water level and the bottom of the superstructure girders, which reflect the height that the wave needs to reach before have some interaction with specimen. In Figure 3.13 and Figure 3.14, the mean curve fit lines along with 95% prediction limits for both horizontal and vertical forces and wave height are shown. Finally, force magnification factors were calculated by dividing the computed slopes for the two flexible setups by the slope of the rigid setup (the reference case). Since three slopes, corresponding to mean, lower, and upper 95% prediction limits, were available for each case, force magnification factors using combinations were computed.

Recall that the data used to generate these curve fits are represented by the average value of 5 to 7 peaks in series for a selected window of loading cycles, as shown in Figure 3.5. Three windows per one trial were defined and their average were computed. The magnification factors for all five water levels and three wave periods are included in Appendix E.

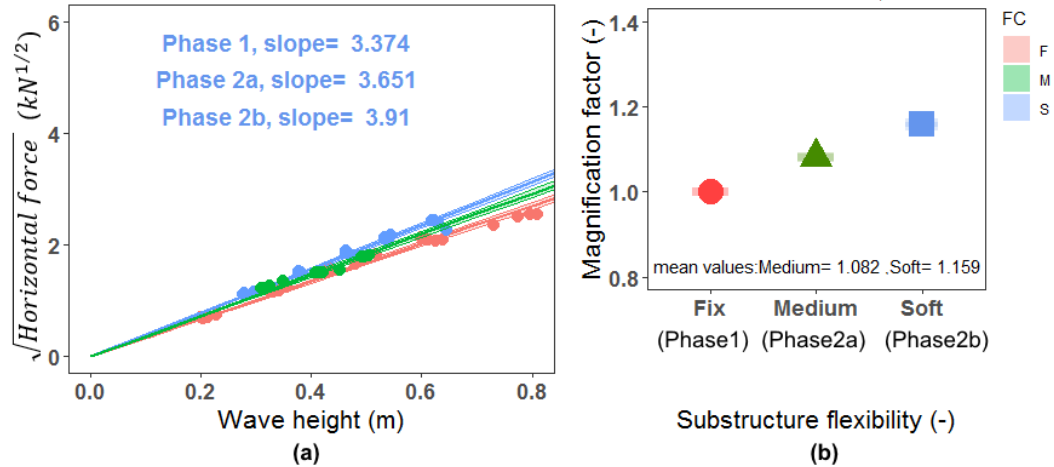


Figure 3.13. Illustration of force magnification factors for sample horizontal force with $d^* = 0.0$ and $T_p = 2.5$ s: (a) Mean curve fit lines along with 95% prediction limits for the horizontal wave forces and (b) force magnification factors for different substructure flexibilities, considering the rigid condition as the reference value. Error bars represent 95% prediction limits of the curve fits.

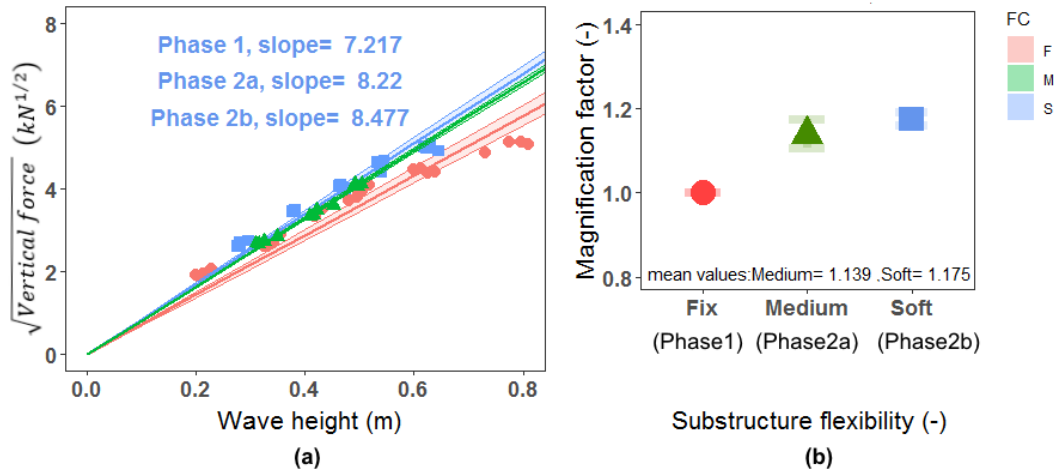


Figure 3.14. Illustration of force magnification factors for sample vertical force with $d^* = 0.0$ and $T_p = 2.5$ s: (a) Mean curve fit lines along with 95% prediction limits for the vertical wave forces and (b) force magnification factors for different substructure flexibilities, considering the rigid condition as the reference value. Error bars represent 95% prediction limits of the curve fits.

To find if the slopes of the fitted regression lines for the flexible setups are significantly different from the fitted regression lines for the rigid setup, tests of

restrictions were run for all different cases of water levels and wave periods. In these tests, two models are generated. The full model (or: unrestricted model) is one which assumes that the slope of the regression line fitted to the whole data is affected by both data setups (rigid and flexible), which can be written as:

$$\sqrt{Force} = m_{rigid} \cdot wave\ heights_{rigid} + m_{flexible} \cdot wave\ heights_{flexible} \quad 3.2$$

In this case, the wave heights are recognized by their groups (rigid/ flexible), and the final regression line is affected by the two groups.

For the restricted model, on the other hand, it is assumed that the slopes of the two groups are the same. Therefore, the new model (or: restricted model) is written as:

$$\sqrt{Force} = m \cdot (wave\ heights_{rigid} + wave\ heights_{flexible}) \quad 3.3$$

F-tests are run using:

$$F = \frac{(SS_{Res}^R - SS_{Res}^F)/r}{SS_{Res}^F/(n-k)}, \quad 3.4$$

in which r is the number of restrictions, which in this case is equal to 1. SS_{Res} is the sum square of residuals, n is the number of the rows in the data set, and k is number of the total variables used in both models. This test was run for all water levels and wave periods, and the results are summarized in Table 3.3. This table

shows that there is a significant difference between the rigid and flexible setups for all water levels and wave periods at 0.05 level, except for the first water level for wave periods, $T_p = 2$ and 2.5 s, where they were not significant. Note: Significance codes shown in Table 3 are color coded as follows:



Table 3.3. Test of restrictions results.

Water level	Wave period	Medium				Soft			
		Horizontal force		Vertical force		Horizontal force		Vertical force	
		p-value	F-statistic	p-value	F-statistic	p-value	F-statistic	p-value	F-statistic
1	2	4.78E-01	5.16E-01	1.15E-01	2.64E+00	3.56E-03	9.81E+00	9.13E-01	1.22E-02
	2.5	3.29E-02	4.87E+00	3.80E-01	7.88E-01	3.63E-01	8.45E-01	7.79E-02	3.27E+00
	3	4.29E-05	2.29E+01	1.82E-02	6.24E+00	4.09E-05	2.30E+01	4.18E-02	4.52E+00
2	2	6.02E-08	6.38E+01	7.85E-04	1.51E+01	7.49E-05	2.21E+01	2.77E-06	3.55E+01
	2.5	1.49E-10	1.25E+02	8.49E-06	3.32E+01	1.68E-08	6.43E+01	1.93E-07	4.91E+01
	3	2.91E-05	2.33E+01	3.84E-05	2.24E+01	7.66E-08	4.40E+01	5.96E-05	2.04E+01
3	2	2.40E-11	9.45E+01	5.05E-07	3.41E+01	3.91E-07	3.61E+01	7.60E-02	3.31E+00
	2.5	1.51E-04	1.82E+01	2.43E-04	1.68E+01	5.42E-13	1.05E+02	1.26E-07	4.03E+01
	3	1.05E-06	3.52E+01	5.52E-03	8.78E+00	1.46E-06	3.06E+01	5.05E-07	3.41E+01
4	2	1.56E-02	6.87E+00	3.76E-01	8.18E-01	1.41E-01	2.31E+00	3.05E-02	5.23E+00
	2.5	1.99E-04	1.87E+01	1.05E-08	6.76E+01	3.90E-10	7.52E+01	1.52E-12	1.17E+02
	3	1.36E-03	1.29E+01	1.32E-01	2.42E+00	3.08E-08	5.47E+01	2.55E-06	3.35E+01
5	2	1.45E-02	6.87E+00	2.09E-03	1.17E+01	2.74E-01	1.25E+00	1.84E-02	6.32E+00
	2.5	9.04E-02	3.09E+00	8.51E-02	3.20E+00	2.75E-02	5.45E+00	4.17E-04	1.63E+01
	3	5.81E-02	3.93E+00	7.47E-02	3.45E+00	3.77E-04	1.60E+01	6.37E-05	2.16E+01

To gain a better understanding on the behavior of the magnification factors and their range, their values were examined at different water levels across all wave periods, at different wave periods across all water levels, and for the whole data set. Boxplot, as shown in Figure 3.15, were selected as the means to evaluate differences, trends, and to qualitatively confirm whether there was a statistical

difference between force magnification factors associated with different substructure flexibilities.

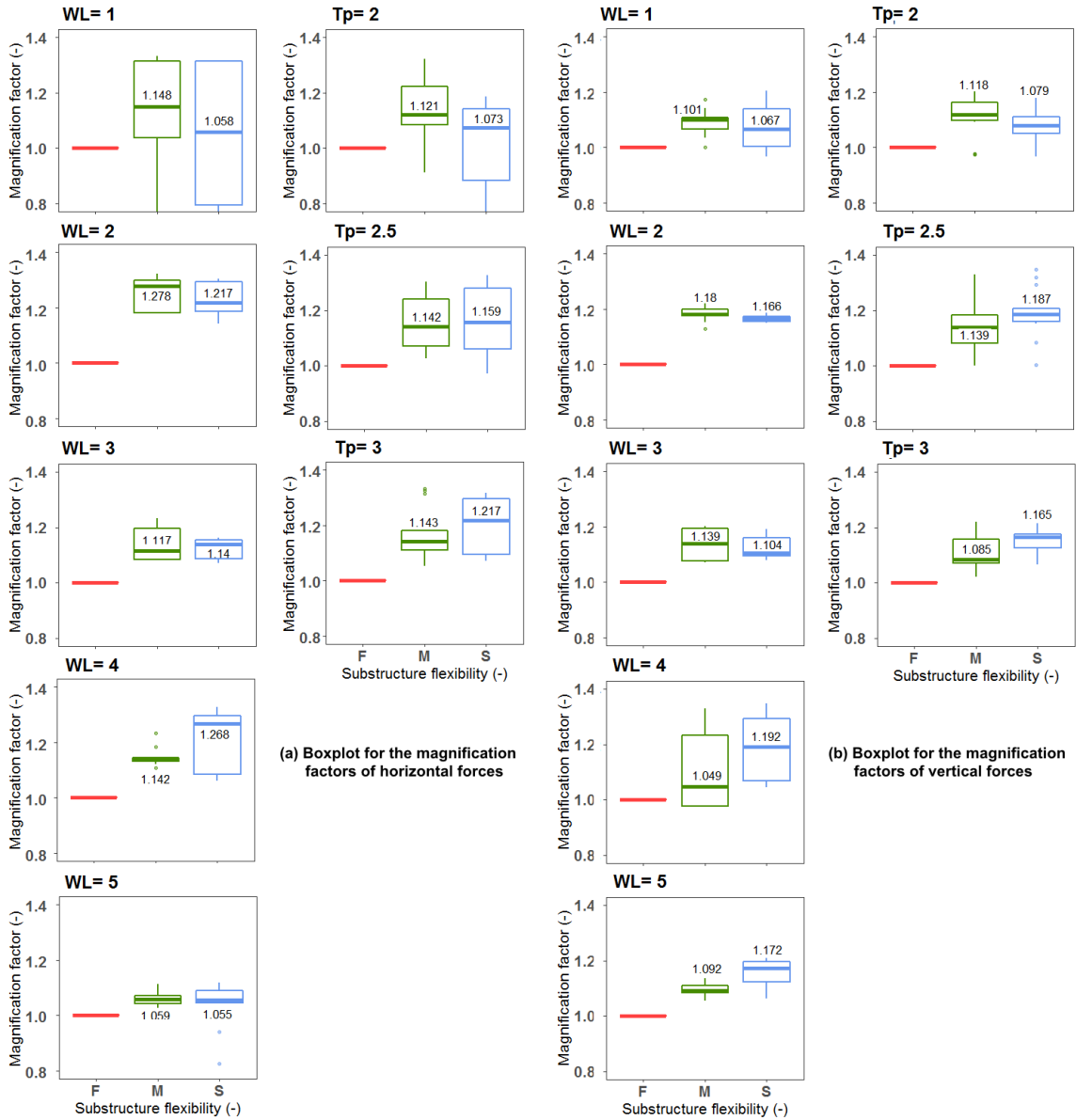


Figure 3.15. Boxplot of the force magnification factors for both horizontal and vertical forces. Numerical values shown represent the median value for the specified group.

Lumped together, force magnification factors across all water level and wave periods for both horizontal and vertical forces are shown in Figure 3.16.

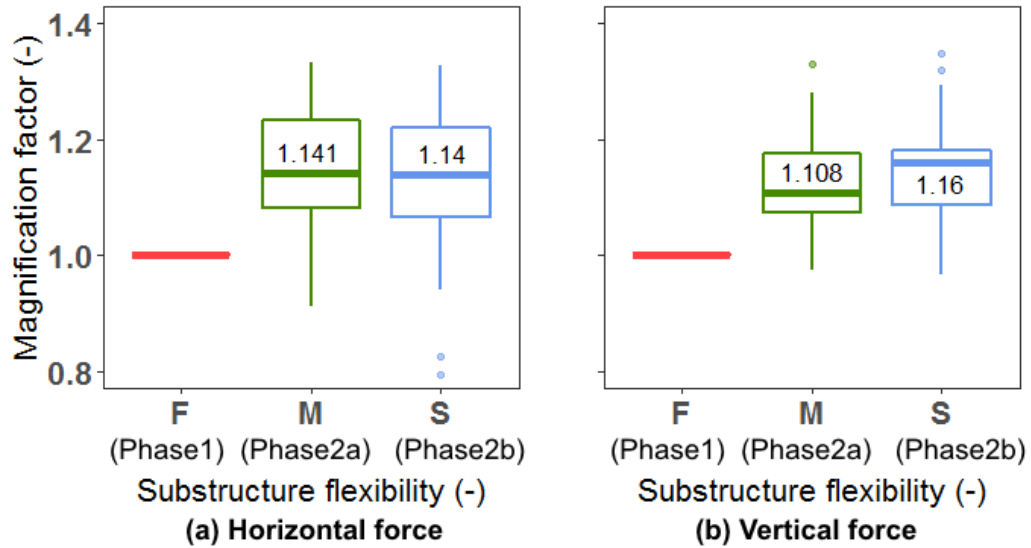


Figure 3.16. Boxplot of the force magnification factors for both horizontal and vertical forces for the all data. Numerical values shown represent the median value for the specified group.

Several important observations can be derived from Figure 3.15 and Figure 3.16, and are as follows:

1. As wave period, T_p increases, the level of substructure flexibility starts to play a role in magnifying both the horizontal and vertical wave forces.
2. With increasing submersion, increasing substructure flexibility magnifies both horizontal and vertical forces.
3. The largest magnification factors are found for $d^* = -0.5$. This may be attributed to the effect of wave height that was discussed in Sections 3.4.1 and 3.4.2.
4. From Figure 3.16, it can be observed that force magnification factors span the same range for both medium and soft setups.

Recommended force magnification factors for horizontal and vertical forces for design purposes are obtained after fitting a distribution function and compute the 50th, 75th, 95th, and 99th percentiles based on the cases shown in Figure 3.16, and as shown in Figure 3.17. Numerical values are shown in Table 3.4 for two fitted distributions, Logistic and Normal.

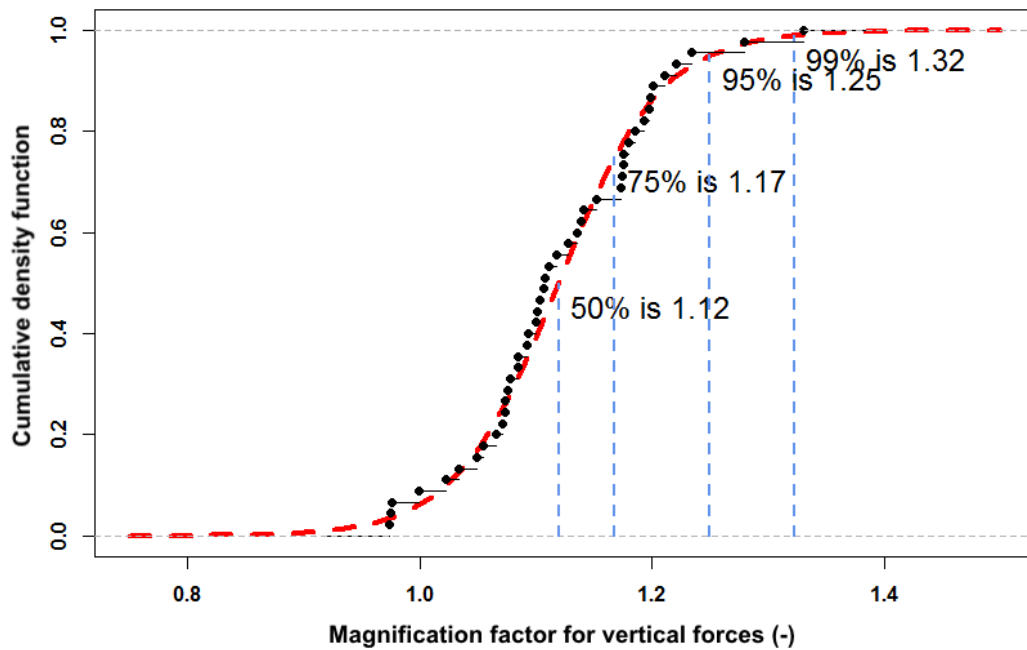


Figure 3.17. Derived MGF from logistic distribution.

Table 3.4. Force magnification factors at different percentiles, for both horizontal and vertical forces

	Fitted distribution	50%	75%	95%	99%
Horizontal	Normal	1.14	1.23	1.34	1.42
	Logistic	1.15	1.22	1.33	1.44
Vertical	Normal	1.12	1.17	1.25	1.30
	Logistic	1.12	1.17	1.25	1.32

Finally, to estimate the horizontal and vertical forces experienced by a bridge superstructure with a flexible substructure, the following equation can be used:

$$F_{flexible} = \left(MGF \sqrt{F_{rigid}} \right)^2 \quad 3.5$$

where F_{rigid} represents the horizontal or vertical forces calculated using equations that were developed based on rigid test setups. MGF are the force magnification factors values showed in and $F_{flexible}$ represents the modified force magnitudes.

3.6 Summary and Conclusion

Data from a unique experimental testing program on wave-induced forces on a large-scale highway bridge superstructure model were analyzed and are presented and discussed in this article. A unique aspect of the test was the ability to adjust the substructure's flexibility. The available data includes three substructure conditions: rigid, medium, and soft. The main conclusion of this study is that substructure flexibility results in increased horizontal as well as vertical forces that a superstructure has to withstand. While equations exist to estimate wave-induced forces, they are based on either rigid supports or unverified numerical models. A physics-based explanation was also developed to explain the observed increase in wave-induced forces. For example, cases with a rigid superstructure show high energy dissipation, whereas for the flexible conditions they showed high energy preservation, which was the reason for the force increase. The effect of wave height is larger for an unsubmerged superstructure

and the case of zero clearance; this effect decreases with increasing level of submersion.

To study the magnification of wave-induced forces, measured horizontal and vertical forces were plotted against different parameters, separately for each substructure flexibility. It was found that waves with longer periods resulted in an increase of the magnification factors. The reason for this could be that longer waves are an indication of higher wave amplitudes with longer contact time with the structure, which allows for a higher level of energy transfer. As the level of submersion increases, increasing substructure flexibility leads to an increase in force magnification. Based on the test of restrictions, substructure flexibility shows a significance effect on the measured forces. However, there is no statistical difference as evident by the significant overlap visible in the boxplots. Hence, magnification factors are proposed at different exceedance levels, which account for the increase in the wave forces when a realistic flexible bridge substructure is considered. These can be used in conjunction with force prediction equations that were based on experiments or models using rigid support conditions.

Future work includes developing more sophisticated force magnification factors that are a function of independent variables such as wave period, water level, and substructure flexibility. Finally, advanced modeling techniques such as the particle finite element method (PFEM) will be employed to substitute additional wave trials allowing for the creation of a force prediction model.

3.7 References

- [1] I. N. Robertson, H. R. Riggs, S. C. Yim, and Y. L. Young, "Lessons from Hurricane Katrina Storm Surge on Bridges and Buildings," *J. Waterw. Port Coast. Ocean Eng.*, vol. 133, no. 6, pp. 463–483, Nov. 2007, doi: 10.1061/(ASCE)0733-950X(2007)133:6(463).
- [2] T. Schumacher, C. Higgins, C. Bradner, D. Cox, and S. C. Yim, "Large-Scale Wave Flume Experiments on Highway Bridge Superstructures Exposed to Hurricane Wave Forces," presented at the Sixth National Seismic Conference on Bridges and Highways Multidisciplinary Center for Earthquake Engineering Research South Carolina Department of Transportation Federal Highway Administration Transportation Research Board, 2008, Accessed: Mar. 09, 2020. [Online]. Available: <https://trid.trb.org/view/1120856>.
- [3] J. B. Lehrman, C. Higgins, and D. Cox, "Performance of Highway Bridge Girder Anchorages under Simulated Hurricane Wave Induced Loads," *J. Bridge Eng.*, vol. 17, no. 2, pp. 259–271, Mar. 2012, doi: 10.1061/(ASCE)BE.1943-5592.0000262.
- [4] C. Bradner, T. Schumacher, D. Cox, and C. Higgins, "Experimental setup for a large-scale bridge superstructure model subjected to waves," *J. Waterw. Port Coast. Ocean Eng.*, vol. 137, no. 1, pp. 3–11, 2010.
- [5] C. Bradner, *Large-scale laboratory observations of wave forces on a highway bridge superstructure*. Oregon State University, 2008.
- [6] C. Bradner, T. Schumacher, D. Cox, and C. Higgins, "Large-Scale Laboratory Observations of Wave Forces on a Highway Bridge Superstructure," 2011.
- [7] B. R. Seiffert, R. C. Ertekin, and I. N. Robertson, "Wave loads on a coastal bridge deck and the role of entrapped air," *Appl. Ocean Res.*, vol. 53, pp. 91–106, 2015.
- [8] R. L. McPherson, "Hurricane induced wave and surge forces on bridge decks," PhD Thesis, Texas A & M University, 2010.
- [9] D. Istrati, I. G. Buckle, P. Lomonaco, S. Yim, and A. Itani, "TSUNAMI INDUCED FORCES IN BRIDGES: LARGE-SCALE EXPERIMENTS AND THE ROLE OF AIR-ENTRAPMENT," *Coast. Eng. Proc.*, vol. 1, no. 35, p. 30, Jun. 2017, doi: 10.9753/icce.v35.structures.30.
- [10] A. Guo, Q. Fang, X. Bai, and H. Li, "Hydrodynamic experiment of the wave force acting on the superstructures of coastal bridges," *J. Bridge Eng.*, vol. 20, no. 12, p. 04015012, 2015.
- [11] B. Huang, B. Zhu, S. Cui, L. Duan, and J. Zhang, "Experimental and numerical modelling of wave forces on coastal bridge superstructures with box girders, Part I: Regular waves," *Ocean Eng.*, vol. 149, pp. 53–77, 2018.
- [12] M. Hayatdavoodi, B. Seiffert, and R. C. Ertekin, "Experiments and computations of solitary-wave forces on a coastal-bridge deck. Part II: Deck with girders," *Coast. Eng.*, vol. 88, pp. 210–228, 2014.
- [13] G. Xu and C. S. Cai, "Wave forces on Biloxi Bay Bridge decks with inclinations under solitary waves," *J. Perform. Constr. Facil.*, vol. 29, no. 6, p. 04014150, 2014.
- [14] H. Xiao, W. Huang, and Q. Chen, "Effects of submersion depth on wave uplift force acting on Biloxi Bay Bridge decks during Hurricane Katrina," *Comput. Fluids*, vol. 39, no. 8, pp. 1390–1400, Sep. 2010, doi: 10.1016/j.compfluid.2010.04.009.
- [15] X. Chen, J. Zhan, Q. Chen, and D. Cox, "Numerical Modeling of Wave Forces on Movable Bridge Decks," *J. Bridge Eng.*, vol. 21, no. 9, p. 04016055, Sep. 2016, doi: 10.1061/(ASCE)BE.1943-5592.0000922.

- [16] W. Huang and H. Xiao, "Numerical Modeling of Dynamic Wave Force Acting on Escambia Bay Bridge Deck during Hurricane Ivan," *J. Waterw. Port Coast. Ocean Eng.*, vol. 135, no. 4, pp. 164–175, Jul. 2009, doi: 10.1061/(ASCE)0733-950X(2009)135:4(164).
- [17] G. Xu and C. S. Cai, "Numerical investigation of the lateral restraining stiffness effect on the bridge deck-wave interaction under Stokes waves," *Eng. Struct.*, vol. 130, pp. 112–123, 2017.
- [18] G. Xu and C. S. Cai, "Numerical simulations of lateral restraining stiffness effect on bridge deck–wave interaction under solitary waves," *Eng. Struct.*, vol. 101, pp. 337–351, 2015.
- [19] A. Guo, Q. Fang, and H. Li, "Analytical solution of hurricane wave forces acting on submerged bridge decks," *Ocean Eng.*, vol. 108, pp. 519–528, 2015.
- [20] Q. Fang, R. Hong, A. Guo, P. K. Stansby, and H. Li, "Analysis of hydrodynamic forces acting on submerged decks of coastal bridges under oblique wave action based on potential flow theory," *Ocean Eng.*, vol. 169, pp. 242–252, 2018.
- [21] "Development of the AASHTO guide specifications for bridges vulnerable to coastal storms | Request PDF," *ResearchGate*. https://www.researchgate.net/publication/299678527_Development_of_the_AASHTO_guide_specifications_for_bridges_vulnerable_to_coastal_storms (accessed Nov. 09, 2018).
- [22] G. Cuomo, M. Tirindelli, and W. Allsop, "Wave-in-deck loads on exposed jetties," *Coast. Eng.*, vol. 54, no. 9, pp. 657–679, 2007.
- [23] G. Cuomo, K. Shimosako, and S. Takahashi, "Wave-in-deck loads on coastal bridges and the role of air," *Coast. Eng.*, vol. 56, no. 8, pp. 793–809, Aug. 2009, doi: 10.1016/j.coastaleng.2009.01.005.
- [24] M. Hayatdavoodi, K. Treichel, and R. C. Ertekin, "Parametric study of nonlinear wave loads on submerged decks in shallow water," *J. Fluids Struct.*, vol. 86, pp. 266–289, 2019.
- [25] H. Park, T. Tomiczek, D. T. Cox, J. W. van de Lindt, and P. Lomonaco, "Experimental modeling of horizontal and vertical wave forces on an elevated coastal structure," *Coast. Eng.*, vol. 128, pp. 58–74, Oct. 2017, doi: 10.1016/j.coastaleng.2017.08.001.
- [26] J. Jin and B. Meng, "Computation of wave loads on the superstructures of coastal highway bridges," *Ocean Eng.*, vol. 38, no. 17–18, pp. 2185–2200, 2011.
- [27] J. Marin and D. M. Sheppard, "Storm surge and wave loading on bridge superstructures," in *Structures Congress 2009: Don't Mess with Structural Engineers: Expanding Our Role*, 2009, pp. 1–10.
- [28] P. Kaplan, J. J. Murray, and W. C. Yu, "Theoretical analysis of wave impact forces on platform deck structures," American Society of Mechanical Engineers, New York, NY (United States), 1995.

Chapter 4

Manuscript 3: Implementation of the OpenSeesPy Particle Finite Element Method (PFEM) to Study Wave-induced Forces on Bridge Superstructures

This manuscript is co-authored by Minjie Zhu, Thomas Schumacher (adviser), and Christopher Higgins. This manuscript is currently being prepared for submission to a journal.

4.1 Introduction

Bridges are considered important link elements in an infrastructure network during crises to provide rescue and assistance to the stricken areas. Studying and investigating these structures helps to minimize the danger and reducing their vulnerability to damage, while increasing the structure's lifetime. Many coastal bridges are susceptible to wave action, especially during hurricanes where the still water level can rise significantly, and tsunami events. Records from Hurricane Katrina in 2005 show that a common type of failure was related to the inadequate connections between bridge superstructure and substructure [1]–[3], which in some cases led to the superstructure being swept off the substructure [4]. Reflecting on this type of failure, researchers started to perform experimental studies to quantify the forces that are induced by hurricane waves [5]–[8]. Many parameters were believed to affect the magnitude of the induced forces such as wave height, wave period, level of submersion [9]–[11], and amount of entrapped air [12], [13]. Other parameters were studied via numerical methods such as

number of girders, air vents in the deck [14], inclination of the deck, and other general modeling parameters [15].

The effect of support flexibility on the observed forces has been a subject in several studies. The first observations based on large-scale experimental test data is reported in [16]. In this research, support flexibility is represented by the lateral flexibility of the bridge substructure, consisting of bent cap and columns, as well as the soil. The dynamic properties, type of damping, as well as a proper equation of motion that controls the behavior of the studied bridge superstructure system were presented in Chapter 2. An analysis of the experimental data set described in [17] was presented in Chapter 3, where the effect of support flexibility was investigated after contradicting findings looking into support flexibility issue were raised [16], [18]–[20]. Some studies show the opposite, i.e. forces decrease with increasing support flexibility [21]. Others have reported that as support flexibility increases, wave forces increase, which they found both experimentally [16] and numerically [19], [20]. The latter position is supported by the authors of this article, and discussed in Chapter 3. Based on the recommendations given in Chapter 2, one should consider the proper equation of motion and the estimated dynamic parameters to accurately model wave action on bridges. In this article, the PFEM available through OpenSeesPy [22] is introduced as a means to properly simulate fluid-structure interaction for bridge superstructures under wave action.

Numerical modeling is an effective and inexpensive way to conduct different studies in different areas, since it minimizes time and cost that physical

experiments can take. Besides, it has the ability to build models as the real structure size, along with the ability to change different parameters easily. Particle Finite Element Modelling (PFEM) is a numerical method based on the standard finite element method (FEM), which discretizes the studied domain into elements of finite size and solves the governing equations using the shape functions with the Galerkin-weighted residual method [23], [24]. However, in PFEM, the nodes of these elements can freely move based on the solutions of the Lagrangian formulation to the governing equations. This method has a variety of important applications. In this chapter, the implementation of the PFEM method for modeling a bridge superstructure subjected to wave action and evaluating the effect of substructure flexibility to the measured forces is presented and discussed.

4.2 Motivation and Objective

In fluid-structure interaction problems (FSI), PFEM has received significant attention among researchers [25]–[27] due to its ability to process problems encountered with large deflections in both the fluid and solid domains. FSI represents a fully coupled problem where fluid movement directly affects how the structure is represented in the fluid. Simultaneously, there is a reverse action (effect) on the fluid flow. The PFEM has been used to solve a wide range of engineering problems, including wave action on breaking waters and bridges, and large motion of floating objects and submerged bodies [28]. The objective of this study was to implement and validate the PFEM by modeling select trials of a large-scale experimental study [17] and thereby set the foundation to perform parameter

studies on modified versions of the setup. Additionally, this study can be considered a real-world application of the open source package OpenSeesPy scripting with Python [22]. Moreover, this provides a continuation of the work discussed in Chapter 3, which studied the effect of substructure flexibility on the observed forces using experimental data.

4.3 Overview of the PFEM Method

The PFEM is analogous to the standard FEM in that it solves the discretized governing equations through iterative time stepping. However, the main difference between the two methods lies within the remeshing techniques and the identification of updated domain boundaries at each time step [29]. In PFEM, the meshing nodes are treated as moving materials in both the fluid and solid domains, which have the capability to separate from each other for large motions. This capability of separating while maintaining their material properties allows for realistic representations of phenomena such as wave breaking or water splashing.

A key attribute of the PFEM is that the governing equations are formulated using a Lagrangian formulation, which eliminates the convective terms in the momentum equation. One difficulty that emerges thereby is how to move the meshing nodes in an efficient way [30], [31]. A moving mesh approach was used as the first implementation of the PFEM [25], in which the meshes for all domains are updated and remeshed again at each time step. The updating does not take place during nonlinear iterations within one time step, which may lead to numerical difficulties [32]. A method using a fixed mesh promises computational efficiency

over a moving mesh approach since a remeshing of the domain is not required [32]. Moreover, an advanced remeshing technique, which is considered as a balance between a fixed and moving mesh, is a background mesh. This approach keeps the mesh fixed for the fluid and the solid, but a local moving mesh is created at each time step within the interface layer between fluid and solid (structure) [32]. This method is used in this work.

At each time step, the state variables are assumed to be known, then the discretized governing equations are solved to compute the next time state variables. The solution of these equations iterates until it reaches a specified convergence criterion.

4.4 Governing Equations

The governing equations for conservation of linear momentum and conservation of mass in both the fluid and solid domains need to be satisfied. As presented in [29], the Lagrangian form for the conservation of momentum equation can be written as:

$$\rho \cdot \frac{\partial \dot{u}_i}{\partial t} = \frac{\partial \sigma_{ij}}{\partial x_j} + b_i \quad 4.1$$

The conservation of mass equation, also referred to as pressure-velocity relationship, for a real fluid is defined as:

$$\frac{1}{K} \cdot \frac{\partial p}{\partial t} - \frac{\partial \dot{u}_i}{\partial x_i} = 0 \quad 4.2$$

For an incompressible fluid, where $K = \infty$, Equation (2) reduces to:

$$\frac{\partial \dot{u}_i}{\partial x_i} = 0 \quad 4.3$$

In Equations (4.1) to (4.3), \dot{u}_i is velocity along the i^{th} global coordinate, p is the fluid pressure, and K , ρ , b_i , and σ_{ij} are bulk modulus, density of the fluid, body force, and Cauchy stress, respectively.

The constitutive equations used for an incompressible continuum follow [33] and are:

$$\sigma_{ij}^{t+1} = 2\mu \cdot \dot{\epsilon}_{ij} - \delta_{ij} \cdot p^{t+1} \quad 4.4$$

where μ is fluid viscosity, $\dot{\epsilon}$ is deformation rate, and δ_{ij} is the Kronecker delta. The deformation rate is derived from the displacement field:

$$\frac{\partial}{\partial t} (\epsilon_{ij}) = \frac{\partial}{\partial t} \left[\frac{1}{2} \cdot \left(\frac{\partial u_i}{\partial x_j} + \frac{\partial u_j}{\partial x_i} \right) \right] \quad 4.5$$

These set of equations are completed by defining boundary conditions for displacement, and surface traction, as follows:

$$\sigma_{ni} = \bar{\sigma}_{ni} \quad \text{on } \Gamma_\sigma \quad 4.6$$

$$V_i = \bar{V}_i \quad \text{on } \Gamma_V \quad 4.7$$

Maintaining mass balance was an issue in several studies that used PFEM [34]. However, in this study, a MINI element [35] was used, which is a mixed velocity-pressure finite element. Using this element, the velocity field is represented by a continuous piecewise linear function enriched by a bubble function, whereas pressure is represented by a piecewise linear function. This

element satisfies the inf-sup condition and converges with the first order for both velocities and pressures [35].

Synthesizing the contribution of all elements, the governing equations can be written in matrix form, as follows:

$$\mathbf{M}_f \mathbf{u}_f + \mathbf{K}_f \mathbf{u}_f - \mathbf{G}_f \mathbf{p} = \mathbf{F}_f \quad 4.8$$

$$\mathbf{G}_f^T \mathbf{u}_f + \mathbf{L} \mathbf{p} = \mathbf{0} \quad 4.9$$

FSI problems are coupled problems, which implies fluid flow induces forces due to pressure and viscous stress on the structure present in the fluid stream. This effect is manifested as an external force, \mathbf{f}_{ext} defined in the structure's equation of motion:

$$\mathbf{M}_s \mathbf{u}_s + \mathbf{K}_s \mathbf{u}_s + \mathbf{C} \mathbf{u}_s = \mathbf{f}_{\text{ext}} \quad 4.10$$

For more information on the derivations of the equations and their solutions, the reader may refer to [36], [37].

4.5 Experimental Study

The OpenSeesPy PFEM was implemented by validating it against select results from a large-scale experimental study conducted in 2007 at the O. H. Hinsdale Wave Research laboratory at Oregon State University [17]. A realistic 1:5-scale concrete bridge specimen was placed in the 100 m wave flume at a distance of 45.62 m from a flap-type motion wavemaker, as shown in Figure 4.1.

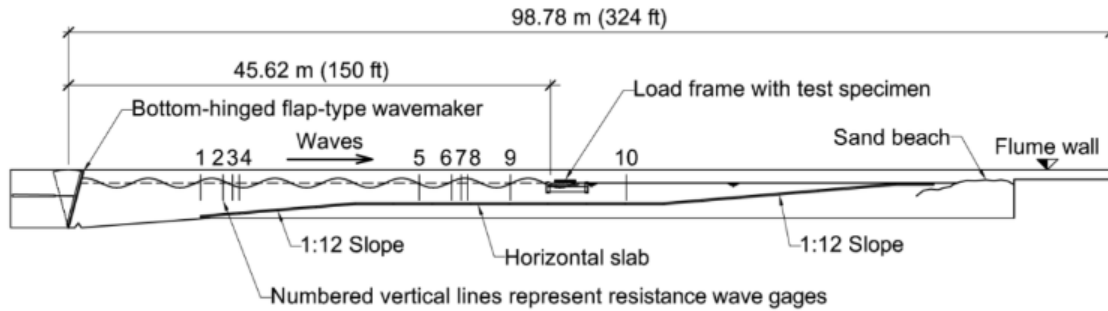


Figure 4.1. Elevation view of the large wave flume. (Courtesy of Dr. Schumacher).

The test specimen consisted of a 5 cm thick slab supported by six scaled AASHTO Type III girders. The overall depth of the specimen superstructure, $h_d = 0.28$ m. Total span of the bridge specimen is 3.45 m. The width of the specimen, $W = 1.94$ m, which is running along the wave propagation. The experimental setup is characterized by a unique ability to adjust the lateral support flexibility to represent different substructure flexibilities. This is achieved by inserting springs between the horizontal load cell (LC) and the end block of the steel reaction frame. Phase 1 represents the rigid configuration without a spring, while Phase 2a and 2b represent medium and soft substructure configurations, respectively. The stiffnesses of the springs representing these configurations were selected based on a finite element analysis of different bent frame configurations with battered piles (for details see [38]). Figure 4.2 shows drawings of the test specimen and setup. Additional details can be found in [17].

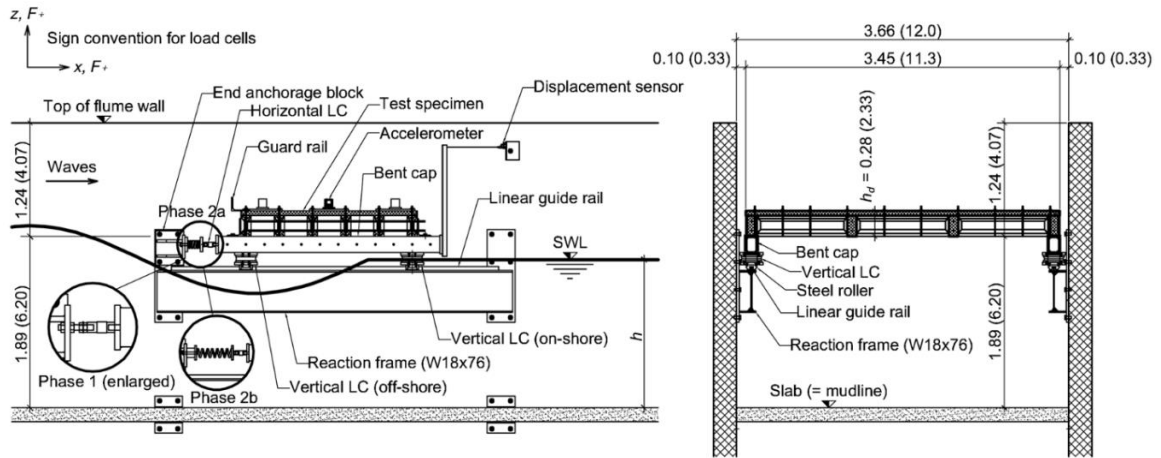


Figure 4.2. Drawing of bridge superstructure specimen with key instrumentation used in this study (a) elevation view (longitudinal cut) and (b) view up the flume (cut across the flume). Dimensions: m (ft). Notation: LC = load cell, SWL = still water level, h = water depth, h_c = superstructure depth. (Courtesy of Dr. Schumacher)

The testing protocol included running over 400 trials with different wave conditions, water levels, and substructure flexibility conditions. Reaction forces were measured directly with six load cells, as shown in Figure 4.2. Displacement sensors captured the lateral motion of the specimen during Phase 2.

4.6 Simulations

The objective of this chapter was to implement a numerical model based on the OpenSeesPy PFEM and validate it with select experimental data described in [17]. Two substructure configurations were selected: Phase 1 (rigid) and Phase 2b (soft springs). To minimize computational time, the numerical simulation was based on the 1:5 model scale to directly match the experimental measurements. Additionally, only a portion of the flume was included in the simulation. The total length of wave flume included in the domain was 50.0 m, of which the first 3.5 m

were part of the wavemaker, followed by 30 and 20 m of horizontal and 1/10 inclined floor beds, respectively. The inclined floor bed is designed to dissipate the coming waves and minimize their reflections, in both the physical and numerical experiments. As opposed to the experimental tests, waves in the numerical simulations were generated via a piston wavemaker, through selecting a desired water level, wave period, and wave height. The selection of piston wave maker over the flap wave maker was made because the generated waves via the flap type experienced larger reduction in wave height. As presented in [39], the piston wavemaker gate motion is defined in a numerical simulation through the equation:

$$x_p(t) = \frac{S}{2} \cdot \sin \omega t \quad 4.11$$

where S is gate stroke and ω frequency of piston movement, which is equal to the target wave frequency. The resulting transfer function is defined as:

$$TF = \frac{2(\cosh 2kh - 1)}{\sinh 2kh + 2kh} \quad 4.12$$

where k is the wavenumber, and h is water level. The gate stroke can be defined as:

$$S = \frac{H}{TF} \quad 4.13$$

where H is wave height. The bridge superstructure model was placed at 18 m from the wavemaker. Two wave gauges were defined in front of the model at a distance of 7.8 m and 3.76 m. These wave gauges are representative of the actual locations

of wave gauges 8 and 9, respectively, in the experiment (see Figure 4.1). Figure 4.3 shows the simulation domain.

The mesh size used for the bridge specimen was 0.01 m using the `dispBeamColumn` element. This element is based on the displacement formulation, and it considers the distribution of the plasticity along the element. Gauss-Legendre quadrature is considered as the default rule of integration along the element. Elements properties are identified by the section modulus at each integration point. By default, this element is considered prismatic [40]. For the water body, the mesh size was 0.02 m using the MINI elements as described in Section 4. The number of particles in each element is five in both the x- and y-directions. Maximum and minimum time steps were set equal to $10e-3$ sec and $10e-6$ sec, respectively. Water density, $\rho = 998.2 \text{ kg/m}^3$, water viscosity, $\nu = 8.90e-4 \text{ Pa} \cdot \text{s}$, and water bulk modulus, $K = 2.2e6 \text{ (N/m}^2\text{)}$. The mass of the bridge superstructure specimen was taken to be, $m = 2470 \text{ kg}$, whereas concrete density was assumed, $\rho_c = 2400 \text{ kg/m}^3$. Two substructure flexibility configurations were studied, similar to those defined in the experimental study: rigid (Phase 1) and soft (Phase 2b), which assumes a total lateral substructure stiffness, $k_{tot} = 2 \times 10^7 \text{ kN/m} = 214 \text{ kN/m}$.

Both the experimental and simulation data were subjected to filtering process with a Butterworth low-pass filter with a cutoff frequency = 50 Hz.

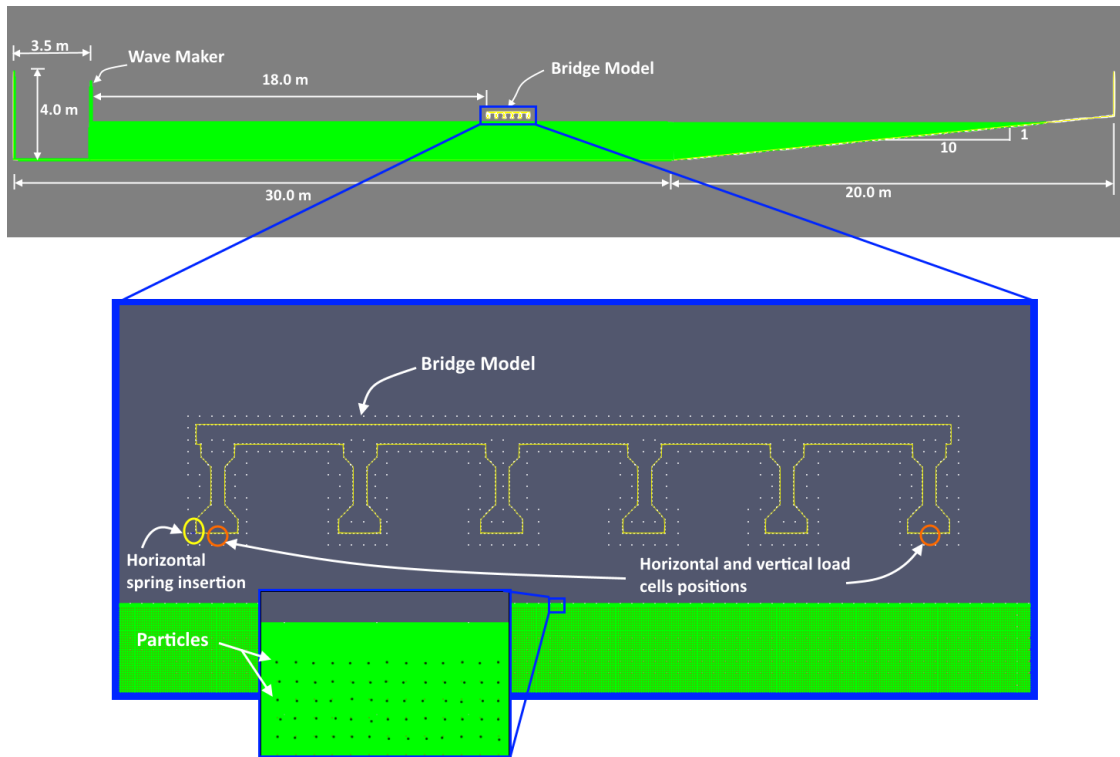


Figure 4.3. Simulation domain of the bridge superstructure setup.

4.7 Model Validation and Results

Initially, the mesh size for the water body was taken equal to 0.03 m, with five particles per element. Implementing this mesh size resulted in a significant reduction in the propagating wave height, which affected the induced forces, especially the vertical component. Therefore, the mesh size was reduced to 0.02 m having four particles per element. This refinement resulted in a notable change in the propagating wave height as well as in the measured forces. Figure 4.4 shows wave gauge readings at wave gauge 8 and wave gauge 9 (WG 8 and WG 9) for $d^* = -0.5$ (second water level), $H = 0.75\text{m}$, and $T_p = 2.5\text{ s}$.

The increase due to mesh refinement at WG 8 was equal to 66.7%, whereas for WG 9 it was 117%) However, wave amplitudes at these wave gauges were still below the magnitudes observed in the experiment by 19.4 and 25.4% at WG and WG 9, respectively. In the experiment, a reduction in wave height between WG 8 and WG 9 of 9.9% could be observed. In the simulation with mesh size 0.02 m it was 13.3%, which is comparable. The reduction in wave amplitude as the wave is propagating can be attributed to the friction viscosity force. As for the simulation, this can be attributed to the numerical model used to define turbulence effects and the used mesh size, in addition to the friction viscosity force.

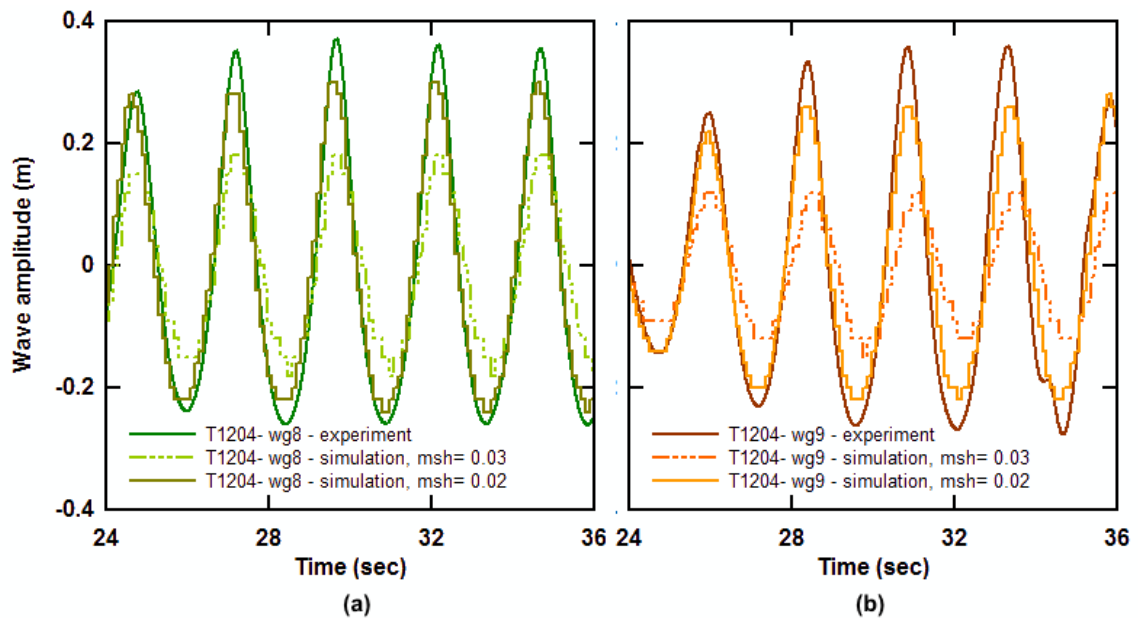


Figure 4.4. Effect of mesh size on propagating wave height.

A comparison of the forces corresponding to the above wave amplitudes is shown in Figure 4.5. The magnitudes of the forces jumped from being unnoticeable to almost the same magnitude of the experimental readings. As for the horizontal

force, the simulation captures the general trend for the experimental record, on the other hand, the vertical force exhibits a couple of noticeable inconsistencies. For this trial, the simulation was not able to capture the significant drop that occurs at time 32.3 s, neither the maximum negative value. Whereas, for the case $d^* = 0.0$ (third water level), $H = 0.625$ m, and $T_p = 3.0$ s, better results were obtained regarding the vertical wave force component, which can be observed in Appendix F.

The discrepancy found for the case of the second water level ($d^* = -0.5$) can be attributed to the specific condition of the test specimen that was not added to the simulation model. In the experiment, the specimen was sitting on two HSS7x5x1/2 steel sections (see Figure 4.2a) that were allowing water to be trapped inside them as the waves approached the superstructure and was discharged after the wave had passed the specimen. Therefore, the additional water affected the weight of the specimen, which resulted in a vertical off-set of the force, as can be observed in Figure 4.5b.

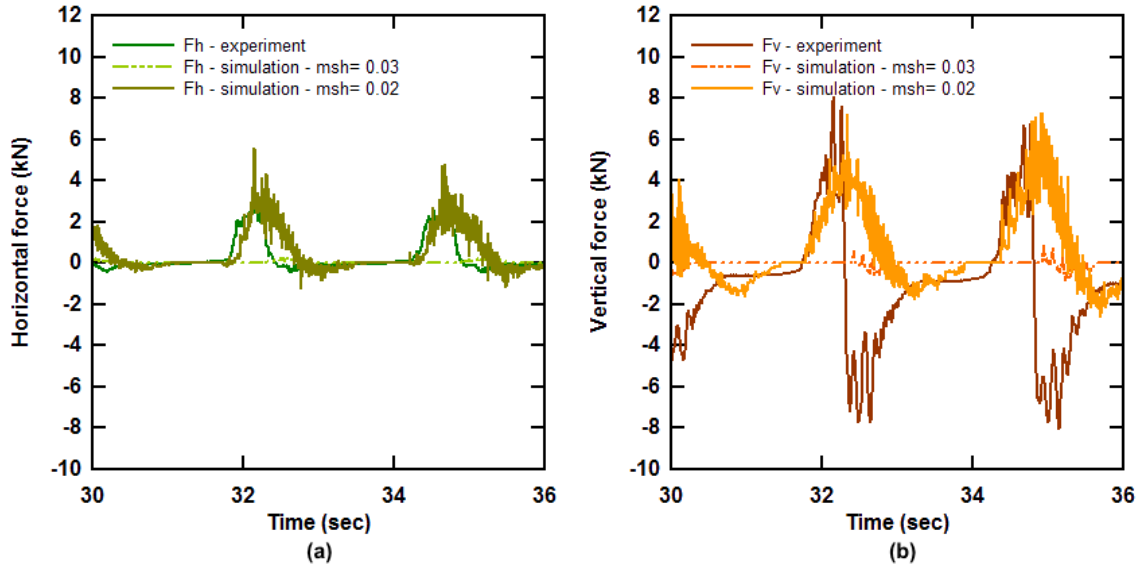


Figure 4.5. Effect of mesh size on simulated forces.

The simulation results did provide a better match with the experimental results for longer wave periods, which can be attributed to the mesh size effect. Hence, improvement for shorter periods will be achieved by further reducing the mesh size.

Figure 4.6 and Figure 4.7 represent cases at $d^* = -0.5$, $H = 0.75$ m, and $T_p = 3$ s. In Figure 4.6, even though the simulation results for the horizontal force shows acceptable agreement with the experimental results for both the rigid and soft substructure conditions, there is still a discrepancy in the width of the transient force response. In addition to the overestimation of the horizontal wave force for the soft setup, an oscillation in the response can be observed. This can be attributed to the friction force, which has not yet been included in the PFEM model, but should be considered in the equation of motion in the future, as suggested per Chapter 2. For the vertical forces, the simulation results show a closer response in

terms of the general trend. However, due to the lack in achieving the required wave height in addition to the water trapped in the bent caps, the simulation results underestimate the maximum positive and negative values recorded in the experiment. This is shown in Figure 4.7.

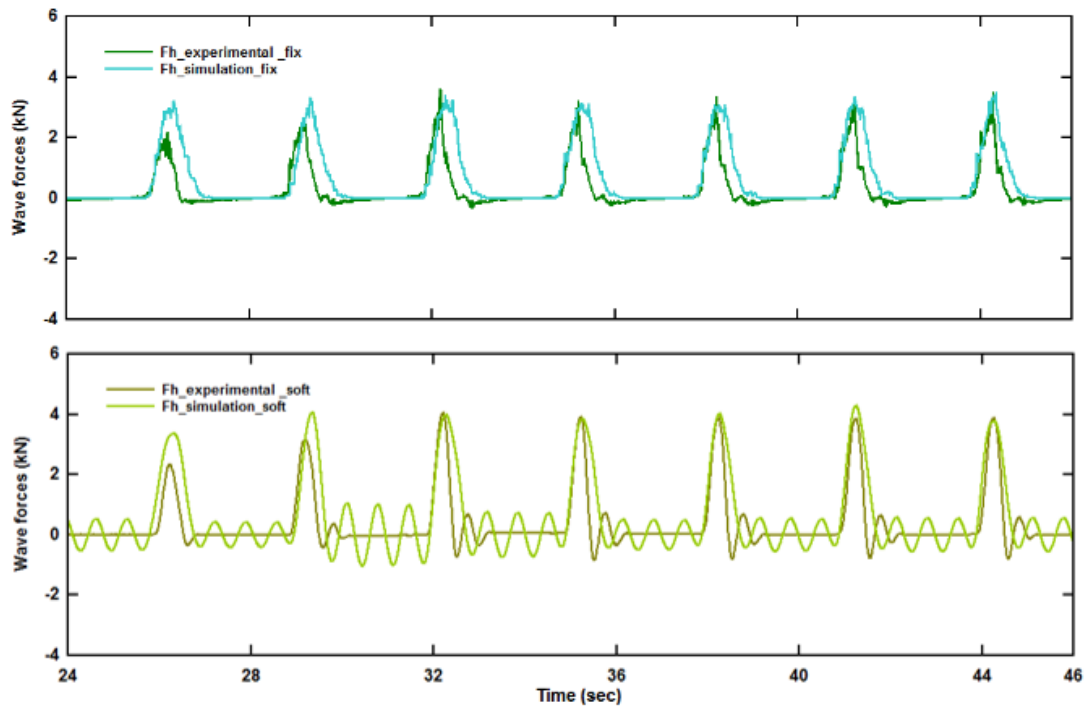


Figure 4.6. Simulation results for horizontal forces compared with the experimental data for case $d^* = -0.5$, $H = 0.75\text{m}$, and $T_p = 3.0\text{ s}$, and for both rigid and soft setups.

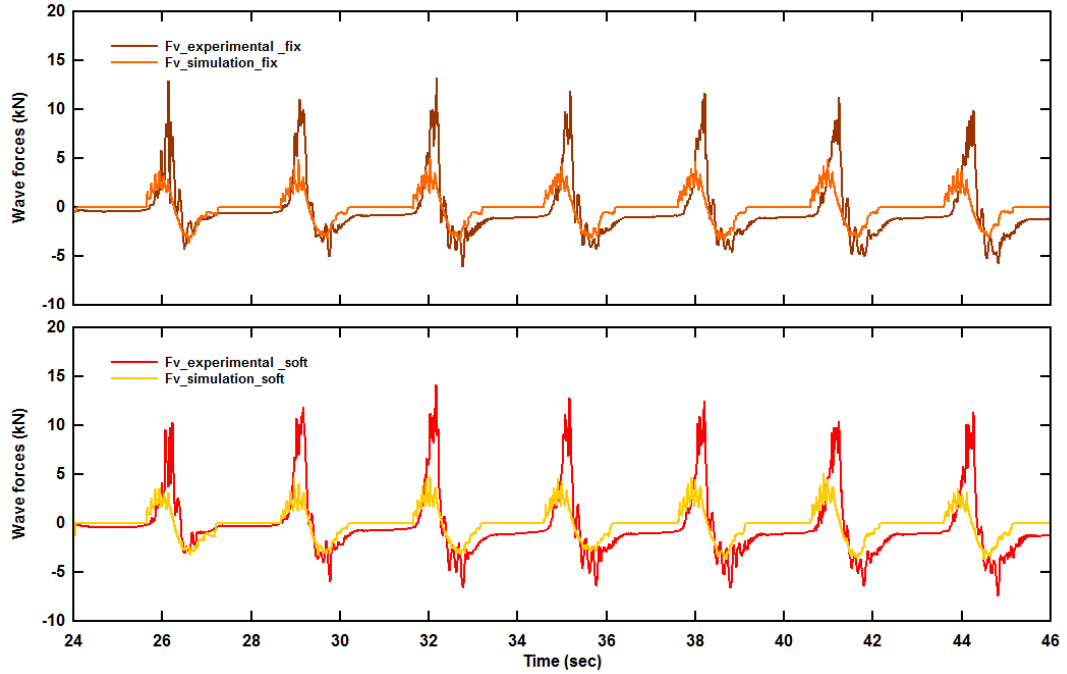


Figure 4.7. Simulation results for vertical forces compared with the experimental data for case $d^* = -0.5$, $H = 0.75\text{m}$, and $T_p = 3.0\text{ s}$, and for both rigid and soft setups.

Finally, the effect of substructure flexibility on the horizontal and vertical forces for both the experimental and simulation results are compared and shown in Figure 4.8 and Figure 4.9.

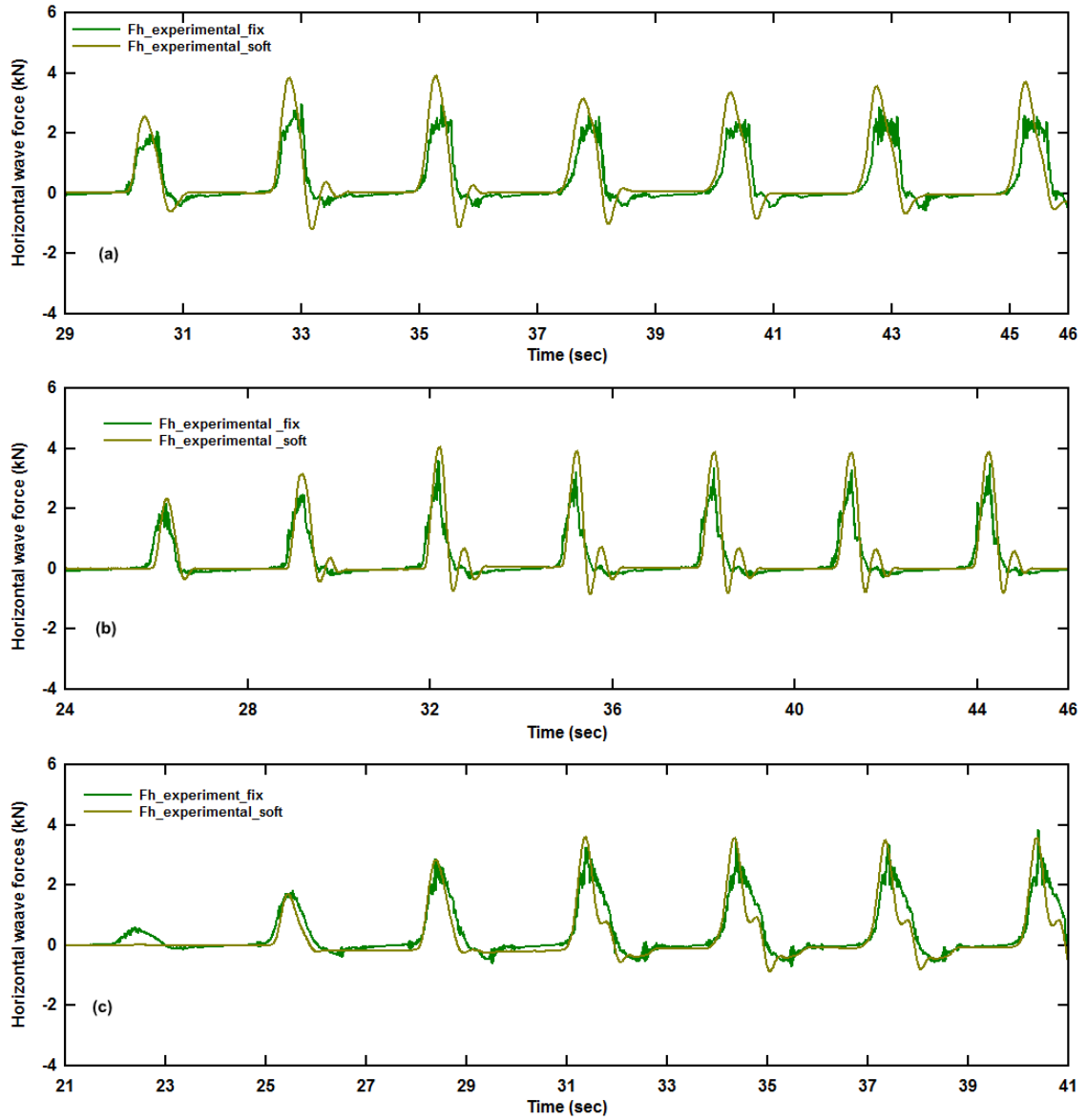


Figure 4.8. Effect of substructure flexibility on horizontal forces for experiment results.

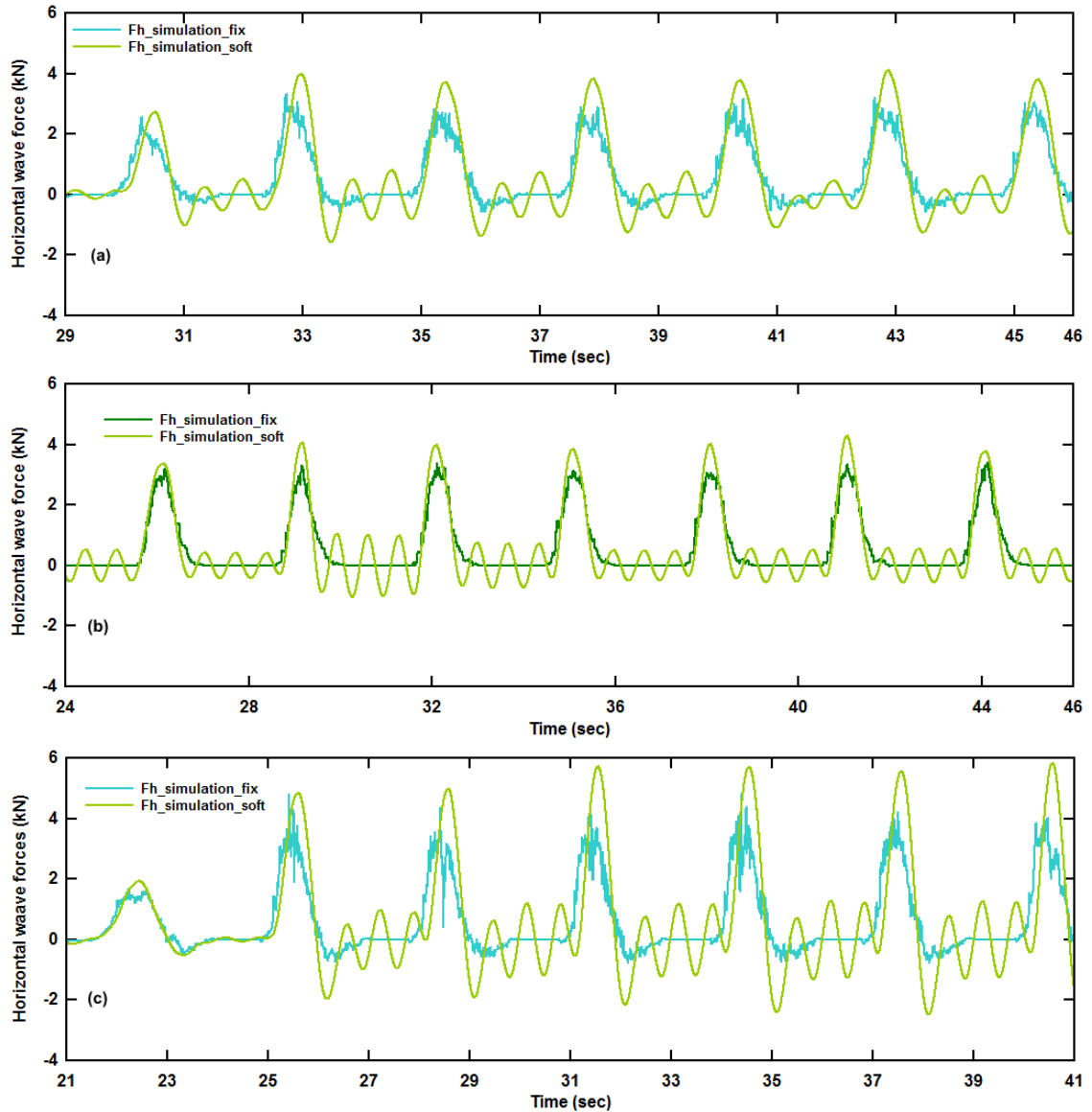


Figure 4.9. Effect of substructure flexibility on horizontal forces for simulation results.

As mentioned in Chapter 3, the observed forces for the soft substructure conditions are larger than those measured for the fixed support condition at the same wave conditions, which is supported by both Figure 4.8 and Figure 4.9. In Appendix G, an expansion to these cases in terms of showing the effect of fixity conditions on vertical forces is presented.

4.8 Summary and Conclusions

A PFEM model was built to simulate a large-scale highway bridge superstructure laboratory specimen tested under wave action. The aim of creating this model was to (a) have the ability to expand the range of parameters tested in the laboratory study and (b) answer new questions that cannot be answered with the available laboratory data. The model was implemented and validated using select available cases. The mesh size was found to be a critical factor affecting the simulation results. Although the results are still informative about the actual behavior and magnitudes for horizontal and vertical forces, more refinement and adjustment of the model needs to occur as well as more sophisticated boundary conditions need to be tested.

Attributable to a number of reasons, a noticeable wave height reduction is observed in the simulation results between WG 8 and WG 9 compared to what was observed in the experiment. In general, wave heights experience a reduction in their amplitude due to fluid viscous friction. The source of this energy dissipation can be divided into two sources: numerical and physical. Numerically, the attributes could be found due to: numerical hardening, mesh size, usage of the turbulent models [41], and the used advection scheme for momentum [41]. Physically, bottom friction/viscosity is considered a main source for wave energy dissipation, which in turn manifested as a wave height reduction as well.

The horizontal forces showed a noticeable change in the behavior especially in terms of the occurrence of the peak value as well as its magnitude when substructure flexibility is varied. Supporting the experimental observations,

peak force is larger for the soft setup compared to the rigid one. Also, the time history of the horizontal force is smoothed out because it is dominated by the single-degree of freedom response discussed in Chapter 2 and this was something found in the simulation results as well. The vertical forces, on the other hand, were not affected by the change of support flexibility conditions in terms of the general behavior, however, a slight increase was found. It should be noted that a decrease in mesh size is expected to significantly improve the simulation results for the vertical forces as they are found to be more sensitive.

In conclusion, the PFEM shows promise with acceptable agreement with the experimental data under the limited mesh sizes studied. A further decrease of the mesh size is needed, and will be performed in the future. This will come with additional significant computational cost.

4.9 References

- [1] I. N. Robertson, H. R. Riggs, S. C. Yim, and Y. L. Young, "Lessons from Hurricane Katrina Storm Surge on Bridges and Buildings," *J. Waterw. Port Coast. Ocean Eng.*, vol. 133, no. 6, pp. 463–483, Nov. 2007, doi: 10.1061/(ASCE)0733-950X(2007)133:6(463).
- [2] M. Hayatdavoodi and R. C. Ertekin, "Review of wave loads on coastal bridge decks," *Appl. Mech. Rev.*, vol. 68, no. 3, p. 030802, 2016.
- [3] Q. Chen, L. Wang, and H. Zhao, "Hydrodynamic investigation of coastal bridge collapse during Hurricane Katrina," *J. Hydraul. Eng.*, vol. 135, no. 3, pp. 175–186, 2009.
- [4] J. Jin and B. Meng, "Computation of wave loads on the superstructures of coastal highway bridges," *Ocean Eng.*, vol. 38, no. 17–18, pp. 2185–2200, 2011.
- [5] "Development of the AASHTO guide specifications for bridges vulnerable to coastal storms | Request PDF," *ResearchGate*. https://www.researchgate.net/publication/299678527_Development_of_the_AASHTO_guide_specifications_for_bridges_vulnerable_to_coastal_storms (accessed Nov. 09, 2018).
- [6] R. G. Bea, T. Xu, J. Stear, and R. Ramos, "Wave Forces on Decks of Offshore Platforms," *J. Waterw. Port Coast. Ocean Eng.*, vol. 125, no. 3, pp. 136–144, May 1999, doi: 10.1061/(ASCE)0733-950X(1999)125:3(136).

- [7] James Derek, Cleary John, and Douglass Scott, "Estimating Wave Loads on Bridge Decks," *Struct. Congr.* 2015, doi: 10.1061/9780784479117.016.
- [8] T. Q. Do, J. W. van de Lindt, and D. T. Cox, "Performance-based design methodology for inundated elevated coastal structures subjected to wave load," *Eng. Struct.*, vol. 117, pp. 250–262, Jun. 2016, doi: 10.1016/j.engstruct.2016.02.046.
- [9] G. Cuomo, M. Tirindelli, and W. Allsop, "Wave-in-deck loads on exposed jetties," *Coast. Eng.*, vol. 54, no. 9, pp. 657–679, 2007.
- [10] H. Park, T. Tomiczek, D. T. Cox, J. W. van de Lindt, and P. Lomonaco, "Experimental modeling of horizontal and vertical wave forces on an elevated coastal structure," *Coast. Eng.*, vol. 128, pp. 58–74, Oct. 2017, doi: 10.1016/j.coastaleng.2017.08.001.
- [11] H. Xiao, W. Huang, and Q. Chen, "Effects of submersion depth on wave uplift force acting on Biloxi Bay Bridge decks during Hurricane Katrina," *Comput. Fluids*, vol. 39, no. 8, pp. 1390–1400, Sep. 2010, doi: 10.1016/j.compfluid.2010.04.009.
- [12] G. Cuomo, K. Shimosako, and S. Takahashi, "Wave-in-deck loads on coastal bridges and the role of air," *Coast. Eng.*, vol. 56, no. 8, pp. 793–809, Aug. 2009, doi: 10.1016/j.coastaleng.2009.01.005.
- [13] B. R. Seiffert, R. C. Ertekin, and I. N. Robertson, "Wave loads on a coastal bridge deck and the role of entrapped air," *Appl. Ocean Res.*, vol. 53, pp. 91–106, 2015.
- [14] M. Hayatdavoodi, B. Seiffert, and R. C. Ertekin, "Experiments and computations of solitary-wave forces on a coastal-bridge deck. Part II: Deck with girders," *Coast. Eng.*, vol. 88, pp. 210–228, 2014.
- [15] N. Ataei and J. E. Padgett, "Influential fluid–structure interaction modelling parameters on the response of bridges vulnerable to coastal storms," *Struct. Infrastruct. Eng.*, vol. 11, no. 3, pp. 321–333, Mar. 2015, doi: 10.1080/15732479.2013.879602.
- [16] T. Schumacher, C. Higgins, C. Bradner, D. Cox, and S. C. Yim, "Large-Scale Wave Flume Experiments on Highway Bridge Superstructures Exposed to Hurricane Wave Forces," presented at the Sixth National Seismic Conference on Bridges and Highways Multidisciplinary Center for Earthquake Engineering Research South Carolina Department of Transportation Federal Highway Administration Transportation Research Board, 2008, Accessed: Mar. 09, 2020. [Online]. Available: <https://trid.trb.org/view/1120856>.
- [17] C. Bradner, T. Schumacher, D. Cox, and C. Higgins, "Experimental setup for a large-scale bridge superstructure model subjected to waves," *J. Waterw. Port Coast. Ocean Eng.*, vol. 137, no. 1, pp. 3–11, 2010.
- [18] D. Istrati, "Large-Scale Experiments of Tsunami Inundation of Bridges Including Fluid-Structure-Interaction," PhD Thesis, 2017.
- [19] G. Xu and C. S. Cai, "Numerical investigation of the lateral restraining stiffness effect on the bridge deck-wave interaction under Stokes waves," *Eng. Struct.*, vol. 130, pp. 112–123, 2017.
- [20] G. Xu and C. S. Cai, "Numerical simulations of lateral restraining stiffness effect on bridge deck–wave interaction under solitary waves," *Eng. Struct.*, vol. 101, pp. 337–351, 2015.
- [21] X. Chen, J. Zhan, Q. Chen, and D. Cox, "Numerical Modeling of Wave Forces on Movable Bridge Decks," *J. Bridge Eng.*, vol. 21, no. 9, p. 04016055, Sep. 2016, doi: 10.1061/(ASCE)BE.1943-5592.0000922.
- [22] "The OpenSeesPy Library — OpenSeesPy 3.1.5.12 documentation." <https://openseespydoc.readthedocs.io/en/latest/#> (accessed Jan. 27, 2020).
- [23] T. J. Chung, *Finite element analysis in fluid dynamics*. New York: McGraw-Hill International Book Co., 1978.

- [24] D. Chandrakant S and A. John F., *Introduction to the Finite Element Method A numerical method for engineering analysis*. VAN Nostrand Reinhold Company.
- [25] E. Oñate, S. R. Idelsohn, F. Del Pin, and R. Aubry, “The particle finite element method — an overview,” *Int. J. Comput. Methods*, vol. 01, no. 02, pp. 267–307, Sep. 2004, doi: 10.1142/S0219876204000204.
- [26] S. R. Idelsohn, E. Oñate, F. D. Pin, and N. Calvo, “Fluid–structure interaction using the particle finite element method,” *Comput. Methods Appl. Mech. Eng.*, vol. 195, no. 17, pp. 2100–2123, Mar. 2006, doi: 10.1016/j.cma.2005.02.026.
- [27] S. R. Idelsohn, E. Oñate, and F. D. Pin, “The particle finite element method: a powerful tool to solve incompressible flows with free-surfaces and breaking waves,” *Int. J. Numer. Methods Eng.*, vol. 61, no. 7, pp. 964–989, 2004, doi: 10.1002/nme.1096.
- [28] E. Oñate *et al.*, “Advances in the Particle Finite Element Method (PFEM) for Solving Coupled Problems in Engineering,” in *Particle-Based Methods: Fundamentals and Applications*, E. Oñate and R. Owen, Eds. Dordrecht: Springer Netherlands, 2011, pp. 1–49.
- [29] E. Oñate, M. A. Celigueta, S. R. Idelsohn, F. Salazar, and B. Suárez, “Possibilities of the particle finite element method for fluid–soil–structure interaction problems,” *Comput. Mech.*, vol. 48, no. 3, p. 307, Jul. 2011, doi: 10.1007/s00466-011-0617-2.
- [30] J. Donea and A. Huerta, *Finite Element Methods for Flow Problems*. John Wiley & Sons, 2003.
- [31] M. D. Gunzburger, *Finite Element Methods for Viscous Incompressible Flows: A Guide to Theory, Practice, and Algorithms*. Elsevier, 2012.
- [32] M. Zhu, I. Elkhetali, and M. H. Scott, “Validation of OpenSees for Tsunami Loading on Bridge Superstructures,” *J. Bridge Eng.*, vol. 23, no. 4, p. 04018015, Apr. 2018, doi: 10.1061/(ASCE)BE.1943-5592.0001221.
- [33] S. R. Idelsohn, J. Marti, A. Limache, and E. Oñate, “Unified Lagrangian formulation for elastic solids and incompressible fluids: Application to fluid–structure interaction problems via the PFEM,” *Comput. Methods Appl. Mech. Eng.*, vol. 197, no. 19, pp. 1762–1776, Mar. 2008, doi: 10.1016/j.cma.2007.06.004.
- [34] “Improving mass conservation in simulation of incompressible flows - Ryzhakov - 2012 - International Journal for Numerical Methods in Engineering - Wiley Online Library.” <https://onlinelibrary-wiley-com.proxy.lib.pdx.edu/doi/full/10.1002/nme.3370> (accessed Jan. 24, 2020).
- [35] Arnold, D. N., Brezzi, F., and Fortain, M., “A stable Finite Element for the Stokes Equations,” *Estratto Calcolo*, vol. XXI, no. IV.
- [36] M. Zhu and M. H. Scott, “Modeling fluid–structure interaction by the particle finite element method in OpenSees,” *Comput. Struct.*, vol. 132, pp. 12–21, Feb. 2014, doi: 10.1016/j.compstruc.2013.11.002.
- [37] E. Oñate, J. García, S. R. Idelsohn, and F. D. Pin, “Finite calculus formulations for finite element analysis of incompressible flows. Eulerian, ALE and Lagrangian approaches,” *Comput. Methods Appl. Mech. Eng.*, vol. 195, no. 23, pp. 3001–3037, Apr. 2006, doi: 10.1016/j.cma.2004.10.016.
- [38] C. Bradner, T. Schumacher, D. Cox, and C. Higgins, “Large–Scale Laboratory Observations of Wave Forces on a Highway Bridge Superstructure,” 2011.
- [39] “Module-2.pdf - MODULE II LABORATORY WAVE GENERATION Prof S A Sannasiraj Department of Ocean Engineering IIT Madras 1 INTRODUCTION Wave form moves.” <https://www.coursehero.com/file/32913067/Module-2pdf/> (accessed Feb. 18, 2020).

- [40] "Displacement-Based Beam-Column Element - OpenSeesWiki."
https://opensees.berkeley.edu/wiki/index.php/Displacement-Based_Beam-Column_Element (accessed May 21, 2020).
- [41] "Why wave height (solitary) is not constant along its propagation in Ansys Fluent?"
ResearchGate.
https://www.researchgate.net/post/Why_wave_height_solitary_is_not_constant_along_its_propagation_in_Ansys_Fluent (accessed Mar. 27, 2020).

Chapter 5

Conclusions and Future Work

5.1 Summary and Conclusions

This PhD dissertation explores the dynamic behavior of coastal bridges subjected to wave action. In particular, a better understanding has been created into how the dynamic properties are affected by submersion as well as how the forces a bridge superstructure experiences are affected by substructure flexibility. This was done by performing a comprehensive analysis of a large data set and by implementing the particle finite element method (PFEM). The data set had been created as part of previous research study that built a unique bridge model with different substructure flexibility levels. The testing protocol consisted of over 400 trials studying a range of wave conditions, water levels, and substructure flexibilities. The findings of this dissertation research are documented in three articles that will allow bridge engineers to build more accurate numerical models for fluid-structure interaction problems and provide practical guidance with respect to the magnification of wave-induced forces for design and evaluation applications. The main findings are summarized as follows:

- The dynamic properties of a structure such as type of damping and natural frequency change with changing levels of submersion. This change can be attributed to the added mass and hydroviscous damping provided by the

surrounding water. As the water level increases, and with it the level of submersion, both added mass and damping increase.

- Dynamic property changes affected by the level of fluid-structure interaction, which in turn affect the wave-induced forces a bridge must sustain and that was captured by the magnification factors.
- The degree of substructure flexibility influences the amount of added mass and damping increment. As substructure flexibility increases, added mass and damping increase. This is an indication of the increase of the vulnerability of a structure, by increasing external forces input.
- While the measured horizontal and vertical forces for both flexible (i.e., medium and soft) substructure conditions are notably different from the rigid case, the difference between the two flexible conditions do not appear significantly different but still show an increasing trend.
- As substructure flexibility increases, a decrease in wave energy dissipation can be observed. In another words, as flexibility increases, an increase in energy preservation occurs, which is the reason for the increase in the observed forces.
- Wave height is a more important variable for the unsubmerged cases and the case of zero clearance. Its effect decreases with increasing level of submersion.
- Forces are magnified as wave period increases. This can be attributed to the associated longer waves, which result in a longer time of exposure, which in turn leads to a higher energy transfer resulting in higher wave forces.

- As the level of submersion increases, an increase in level of substructure flexibility leads to an increase in the measured forces.
- The PFEM is able to predict the experimental data with reasonable accuracy. Even though the friction force was not implemented in the model, simulation results support the notion that structures with flexible supports experienced larger forces.
- From the simulation results, horizontal forces showed to be affected by wave celerity, whereas vertical forces are more dependent on wave height.

5.2 Recommendations for Future Work

A comprehensive statistical analysis of the available experimental data set along with PFEM simulations have provided insightful information on the importance of dynamic property changes on the measured response of a bridge superstructure specimen for different substructure flexibilities. It has further allowed studying how fluid-structure interaction changes by the change of these properties. Based on the work presented in this PhD dissertation, the following aspects should be investigated in the future:

- Investigate additional variables that may affect the proposed force magnification factors and develop a predictive equation that could be used to predict these quantities.
- Employ the PFEM method to perform numerical parameter studies in order to fill in data gaps existing in the current data set such as additional water levels, substructure flexibilities, and wave conditions.

- Utilizing the fundamental knowledge gained in this work as well as employing experimental and numerical data, develop a comprehensive regression model that allows bridge engineers to predict wave-induced forces on bridge superstructures, including substructure flexibility. Compare the model with the current AASHTO guide equations.
- Explore more advanced data mining techniques such as principal component analysis (PCA) (or dimensionality reduction method) to study the importance of variables and their relationships.
- Utilize the PFEM method to study other wave types, e.g. tsunami-based, as well as other structures, e.g. buildings to fill additional knowledge gaps and provide engineers with tools to predict wave-induced forces more accurately.

Appendix A: Runge-Kutta Method

A.1. Runge-Kutta for First Order Differential Equation

The classical fourth-order accurate Runge-Kutta method is used to compute numerical solutions to a first order ordinary differential equation of the form $\dot{x} = f(x, t)$. Letting x_i denote the approximation to the solution, i.e. $x_i \approx x(t_i)$ at time t_i , the Runge-Kutta method is based on the explicit Euler method which predicts the solution at the next time step x_{i+1} by adding the multiplication of the time step (Δt) by the slope (dx/dt) of the curve to the previous value x_i . The RK method however, is a weighted average that means it calculates several slopes and take the average of them that is used in the next step prediction. The following steps provide an explanation of how this method works when the ODE is coupled with the initial condition $x(0) = x_0$.

1) First four slopes are calculated:

$k_1 = F(t_i, x_i)$, the slope at current time and position,

$k_2 = F(t_i + \frac{\Delta t}{2}, x_i + k_1 \cdot \frac{\Delta t}{2})$, the slope at half step ahead using the first predicted slope,

$k_3 = F(t_i + \frac{\Delta t}{2}, x_i + k_2 \cdot \frac{\Delta t}{2})$, the slope at half step ahead using the second predicted slope, and

$k_4 = F(t_i + \Delta t, x_i + k_3 \cdot \Delta t)$, the slope at full step ahead using the third predicted slope.

2) Next the weighted average of the four slopes is multiplied by the time step and added to the current value to get the next predicted value

$$x_{i+1} = x_i + \Delta t \cdot \left(\frac{k_1 + 2k_2 + 2k_3 + k_4}{6} \right)$$

A.2. Implementation of Runge-Kutta Method for Solving Equation of Motion

In this work we seek numerical solutions to the second order equation of motion

$\frac{d^2x}{dt^2} + A \frac{dx}{dt} + Bx = f(t)$, where x denotes the position, and A & B depend nonlinearly on x, \dot{x} and t .

We first translate the second order equation to a system of two first-order equations. To do that, the following methodology [29] is implemented:

1. We introduce a moderator that manipulates the 2nd ODE to a system of 1st ODEs, as follows:

Let $v = \frac{dx}{dt}$ denote the velocity and $\frac{dv}{dt} = \dot{v} = a(t, x, v)$ denotes the acceleration.

The first order system is thus:

$$\text{system (1)} \begin{cases} \dot{x} = v \\ \dot{v} = f(t) - A \cdot v - B \cdot x \end{cases}$$

2. Given initial conditions x_0 and v_0 , we next apply the RK method to the system (1)

Letting $i=0$, we get the first predicted slopes for acceleration and velocity

$$k_1 = a(t_i, x_i, v_i):$$

$$l_1 = v_i$$

3. We then compute the slopes at the various points throughout the time step:

$$k_2 = a\left(t_i + \frac{\Delta t}{2}, x_i + \frac{l_1}{2}, v_i + \frac{k_1}{2}\right)$$

$$l_2 = v_i + \frac{k_1}{2}$$

$$k_3 = a\left(t_i + \frac{\Delta t}{2}, x_i + \frac{l_2}{2}, v_i + \frac{k_2}{2}\right)$$

$$l_3 = v_i + \frac{k_2}{2}$$

$$k_4 = a\left(t_i + \frac{\Delta t}{2}, x_i + l_3, v_i + k_3\right)$$

$$l_4 = v_i + k_3$$

4. Finally, we update position and velocity using the average:

$$v_{i+1} = v_i + \frac{1}{6} \cdot (k_1 + 2k_2 + 2k_3 + k_4) \cdot \Delta t$$

$$x_{i+1} = x_i + \frac{1}{6} \cdot (l_1 + 2l_2 + 2l_3 + l_4) \cdot \Delta t .$$

A.3. Runge-Kutta Verification Test

Numerical methods can serve as powerful tools in computing numerical solutions to differential equations whose analytical solutions are difficult to obtain. However, the reliability of the method in solving a certain problem should be analyzed in terms of its accuracy, stability, and convergence.

The Runge-Kutta method used in this work is both fourth order accurate, and conditionally stable (a property common to all explicit methods). Convergence means that the numerical solution converges to the true solution, as the time step decreases. If we do not know the exact solution, we can manufacture one through the method of manufactured solutions [40] and compare it with our numerical solution. This commonly used technique verifies convergence of the method at the convergence rate predicted by the method's accuracy.

The method of manufactured solutions determines an exact analytical solution to a modified version of the ODE we wish to solve. In most cases the modified problem is the original equation but with an additional source term. If convergence

can be shown for the modified problem, we have verified that our numerical code is producing reliable results. This methodology provides a rigorous test of convergence, allowing us to quantify the error as a function of time step used, and is frequently used in current research projects [41]. The fourth order RK method implies that the error is:

$$E_{\Delta t} = \|X_{exact} - X_{\Delta t}\| \approx C \cdot (\Delta t)^4$$

Where C is a constant,

$\|\cdot\|$ denotes the L_2 – norm,

X_{exact} is the exact solution evaluated at the grid pints t_0, t_1, \dots , and

$X_{\Delta t}$ is the numerical approximation obtained using a time step Δt .

Therefore, to verify that our method is convergent of order 4, we successively halve the time step and take the \log_2 of the ratio of the computed errors. This ratio should approach the theoretical prediction of 4, since,

$$E_{\frac{\Delta t}{2}} = \|X_{exact} - X_{\frac{\Delta t}{2}}\| \approx \left(\frac{\Delta t}{2}\right)^4, \text{ then the ratio}$$

$$\frac{E_{\Delta t}}{E_{\frac{\Delta t}{2}}} = \frac{C \cdot (\Delta t)^4}{C \cdot \left(\frac{\Delta t}{2}\right)^4} = 2^4, \text{ thus}$$

$$\log_2(\text{ratio}) = \log_2(2^4) = 4$$

The equation we solve in this work is the nonlinear second order equation:

$$m \cdot \ddot{x} + c \cdot \dot{x} + \mu \cdot m \cdot g \cdot \text{sign}(\dot{x}) + k \cdot x = 0$$

We manufacture a solution to the modified problem (i.e. we add a source term):

$$m \cdot \ddot{x} + c \cdot \dot{x} + \mu \cdot m \cdot g \cdot \text{sign}(\dot{x}) + k \cdot x = F(t)$$

Where the exact solution is given by

$$x = u_0 \cos(t), \dot{x} = -u_0 \cdot \sin(t), \ddot{x} = -u_0 \cdot \cos(t)$$

This means we can solve for the source term $F(t)$ such that our manufactured solution solves the modified problem, namely

$$F(t) = -m \cdot u_0 \cdot \cos(t) - c \cdot u_0 \cdot \sin(t) + \mu \cdot m \cdot g \cdot \text{sing}(-u_0 \cdot \sin(t)) + k \cdot u_0 \cdot \cos(t)$$

Re-arranging the equation yields

$$\ddot{x} = \frac{1}{m} (-c \cdot \dot{x} - \mu \cdot m \cdot g \cdot \text{sign}(\dot{x}) - k \cdot x - m \cdot u_0 \cdot \cos(t)) + c \cdot u_0 \cdot \sin(t) + \mu \cdot m \cdot g \cdot \text{sing}(-u_0 \cdot \sin(t)) + k \cdot u_0 \cdot \cos(t)$$

Using the 4th order Runge-Kutta method to compute a numerical solution, we compare it with the exact solution in the following table:

Table A.1. Rate of convergence of the Runge – Kutta method as expected to be approaching four for the classical fourth order

Δt	$E_{\Delta t}$	ratio	$\log_2(\text{ratio})$
0.2	5.00E-05		
0.1	3.28E-06	1.52E+01	3.930
0.05	2.05E-07	1.60E+01	4.002
0.025	1.27E-08	1.61E+01	4.007

The results presented in the above table demonstrate that our Runge-Kutta method is converging with fourth order of accuracy, as expected, and we have assurance that numerical solutions to the un-modified problem are reliable.

Appendix B: Global Search Algorithm Validation

The results shown in this section are simulated examples used as part of a parameter study to evaluate the optimization schemes, and do not reflect the real structure. Also, this validation shows a comparison between the used `globalsearch` and manual looping optimization techniques. Moreover, it holds for both soft and medium spring cases. As mentioned and explained in section (5.2), manual looping is based on defined increments for both the damping ratio (ζ) and the friction force (F), and they are defined here to be 0.01 and 10N, respectively. Whereas `globalsearch` is based on the gradient descent method to find the global minimum for the defined function, the manual looping method gets zero percentage errors when the actual values for both damping ratio and friction force are multiples of the defined increments. However, when this condition is not satisfied, `globalsearch` starts to give percentage errors less than the manual looping. Even though the percentage errors are very small and do not exceed 11% (for manual looping), global search proves to be more reliable than the manual looping. Therefore, `globalsearch` was chosen as the optimization tool throughout the study.

Table B.1 Global search algorithm validation for medium spring

X(0) (m)	k (N/m)	m (kg)	ζ <i>actu</i> (-)	F_actu (N)	%error_ GS		%error_ ML	
					ζ (%)	F (%)	ζ (%)	F (%)
0.05	450000	2500	0.07	250	0.060	0.320	0.000	0.000
0.07	450000	2500	0.07	250	0.020	0.063	0.000	0.000
0.1	450000	2500	0.07	250	0.050	0.097	0.000	0.000
0.07	450000	2500	0.07	350	0.000	0.095	0.000	0.000
0.07	450000	2500	0.07	450	0.071	0.266	0.000	0.000
0.05	450000	2500	0.07	253	0.029	0.139	0.000	1.186
0.05	450000	2500	0.063	253	0.740	2.832	3.175	5.138
0.05	450000	2500	0.062	253	0.078	0.224	3.226	10.672
0.05	450000	2500	0.064	252	0.081	0.390	1.563	4.762
0.05	450000	2500	0.064	251	0.003	0.200	1.563	4.382

Table B.2 Global search algorithm validation for soft spring

X(0) (m)	k (N/m)	m (kg)	ζ <i>actu</i> (-)	F_actu (N)	%error_ GS		%error_ ML	
					ζ (%)	F (%)	ζ (%)	F (%)
0.05	107000	2500	0.07	250	1.487	1.879	0	0
0.07	107000	2500	0.07	250	0.917	0.982	0	0
0.1	107000	2500	0.07	250	0.012	0.056	0	0
0.07	107000	2500	0.07	350	1.352	0.904	0	0
0.05	107000	2500	0.07	450	0.412	0.162	0	0
0.05	107000	2500	0.07	253	0.605	0.623	0	1.186
0.05	107000	2500	0.063	253	0.238	0.313	4.762	2.767
0.05	107000	2500	0.062	253	0.183	0.058	3.226	2.767
0.05	107000	2500	0.064	252	0.488	0.251	1.563	0.794
0.05	107000	2500	0.064	251	0.147	0.153	1.563	0.399

Appendix C: Parametric Study Exploring Effect of Damping Types on Response

A parametric study was conducted using numerical simulations of the EOM developed in this research (see Section 2.5.1) to provide insight on how the two damping mechanisms (viscous and friction) interact with each other. This study shows how both damping mechanisms are affected by initial displacement and damping ratio and how they interact with each other to produce the final response. In addition, the model's dynamic properties also contribute to the final response, namely in this case the spring stiffness, whose effect also has been studied here.

The fixed dynamic properties used in this parametric study are:

- $k_{medium} = 458 \text{ kN/m}$
- $k_{soft} = 107 \text{ kN/m}$
- $mass = 2500 \text{ kg}$
- $Friction\ force = 0.370 \text{ kN}$

As the reader proceeds through the following sections, the authors would like to draw their attention to the concept of damping mechanism domination between friction and viscous damping. This domination of damping mechanisms is considered when the response curve for the dominated damping system becomes the lower bound of the two responses.

C.1. Medium Springs Setup

C.1.1. Varying Initial Displacement

For a constant damping ratio and the same structure, initial displacement, $x(0)$ influences the domination of the phase response. Figure C.1 shows the free vibration response for four different initial displacements. As can be observed, as the initial displacement increases, the behavior starts to be dominated by viscous damping. However, friction damping at a certain point (near the end of the response, i.e. at small displacement amplitudes) will dominate. In other words, by increasing the initial displacement, we are increasing the potential energy imposed into the system, which causes the viscous damping role to dominate over the friction damping.

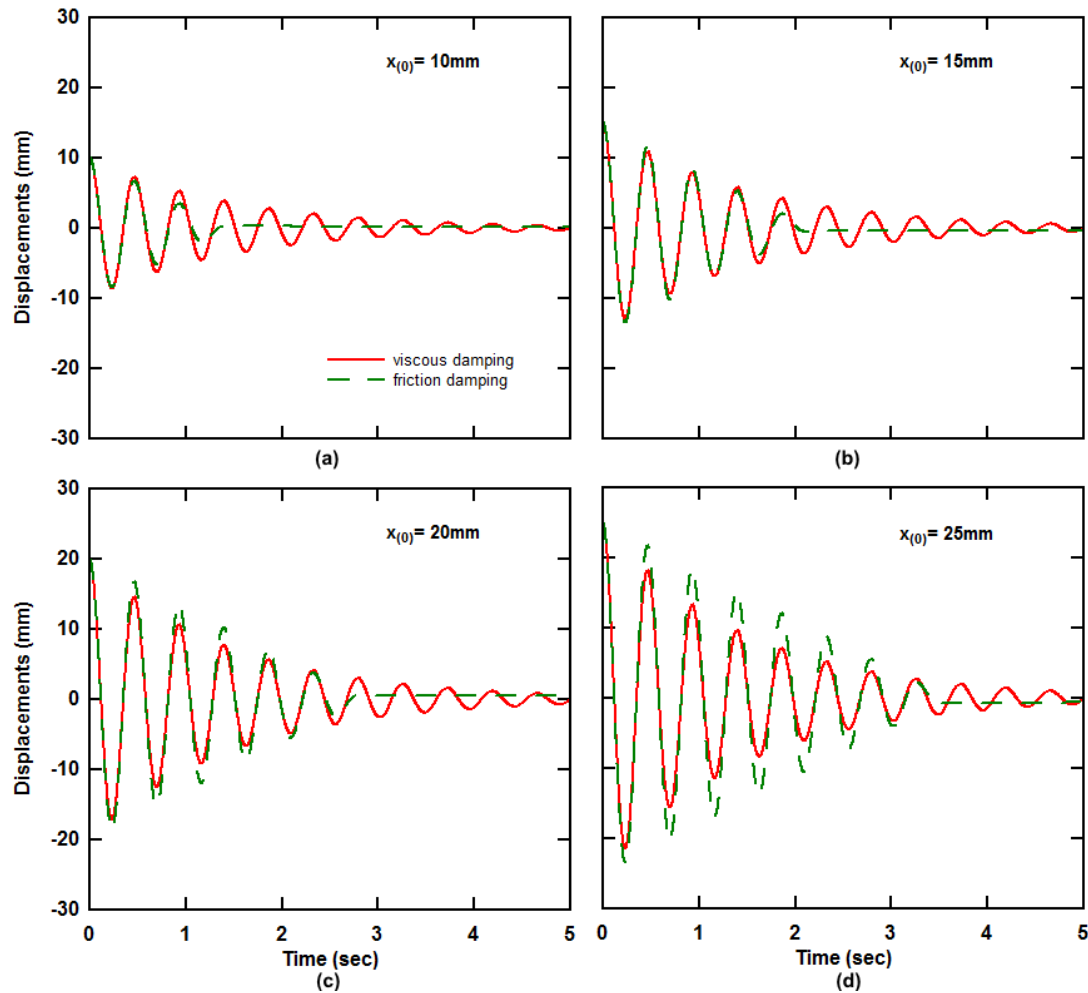


Figure C.1. Parametric study: the effect of initial displacement on the response of two systems having the same mass (2500kg) and stiffness (458 kN/m), one with friction damping ($F=370$ N) and the other with viscous damping $\zeta = 0.05$ (Medium spring case).

C.1.2. Varying Damping Ratio

For this case, the same initial displacement ($x(0) = 15$ mm) was used but in each analysis the damping ratio was increased. Fig. C.2 shows that as the damping ratio increases, the viscous damping force starts to dominate over friction force. Again, friction force starts to dominate at the end of the motion.

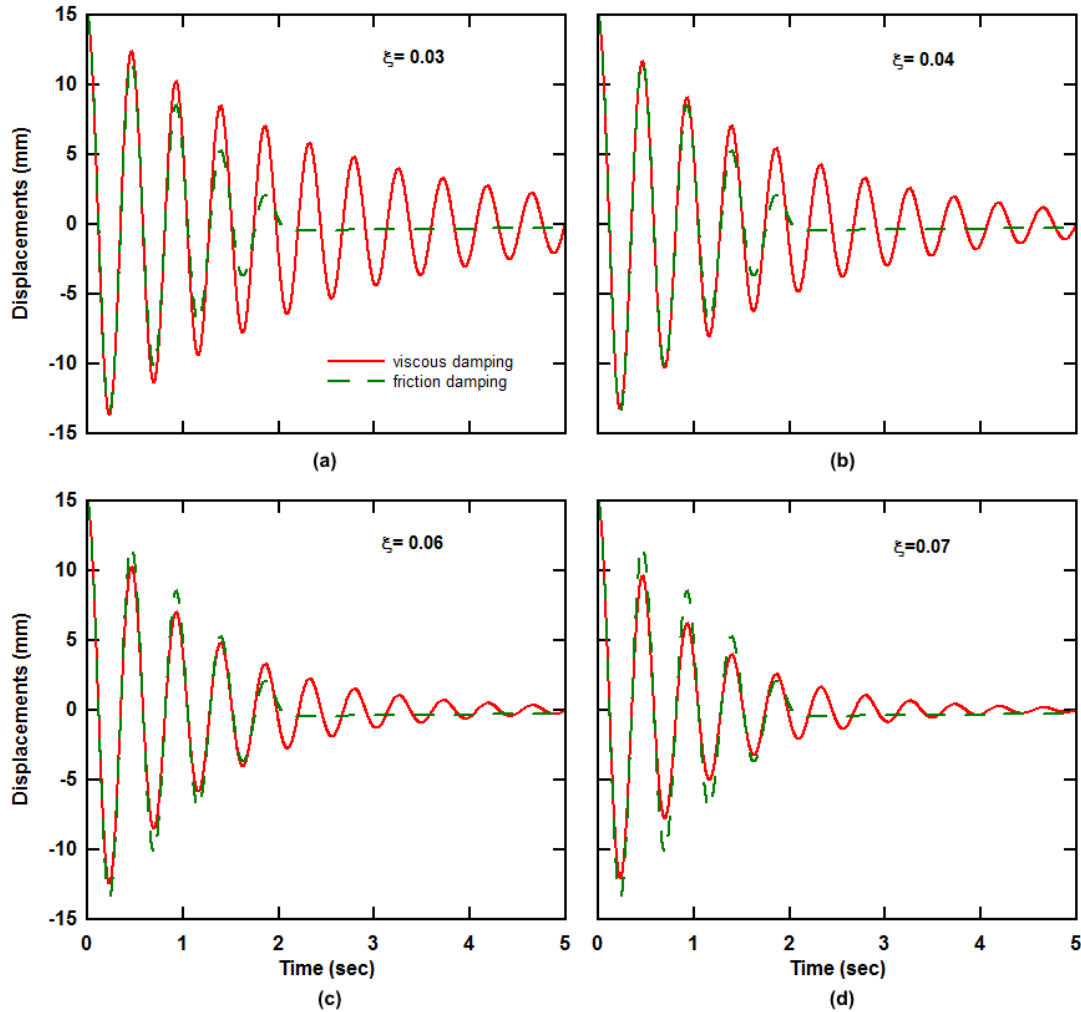


Figure C.2. Parametric study: the effect of damping ratio on the response of two systems of the same mass (2500kg) and stiffness (458kN/m), one with friction damping ($F=370\text{N}$) and the other with various viscous damping ratios, holding the initial displacement constant at ($x(0)= 15\text{mm}$), (Medium spring case).

C.2. Soft Spring Setup

In this case only the effect of the initial displacement will be studied

C.2.1 Varying Initial Displacement

Similar behavior was observed regarding the effect of initial displacement to that seen for the medium springs setup. As the initial displacement increases, viscous

damping starts to dominate over friction damping, except near the end of motion where the displacement amplitudes are small.

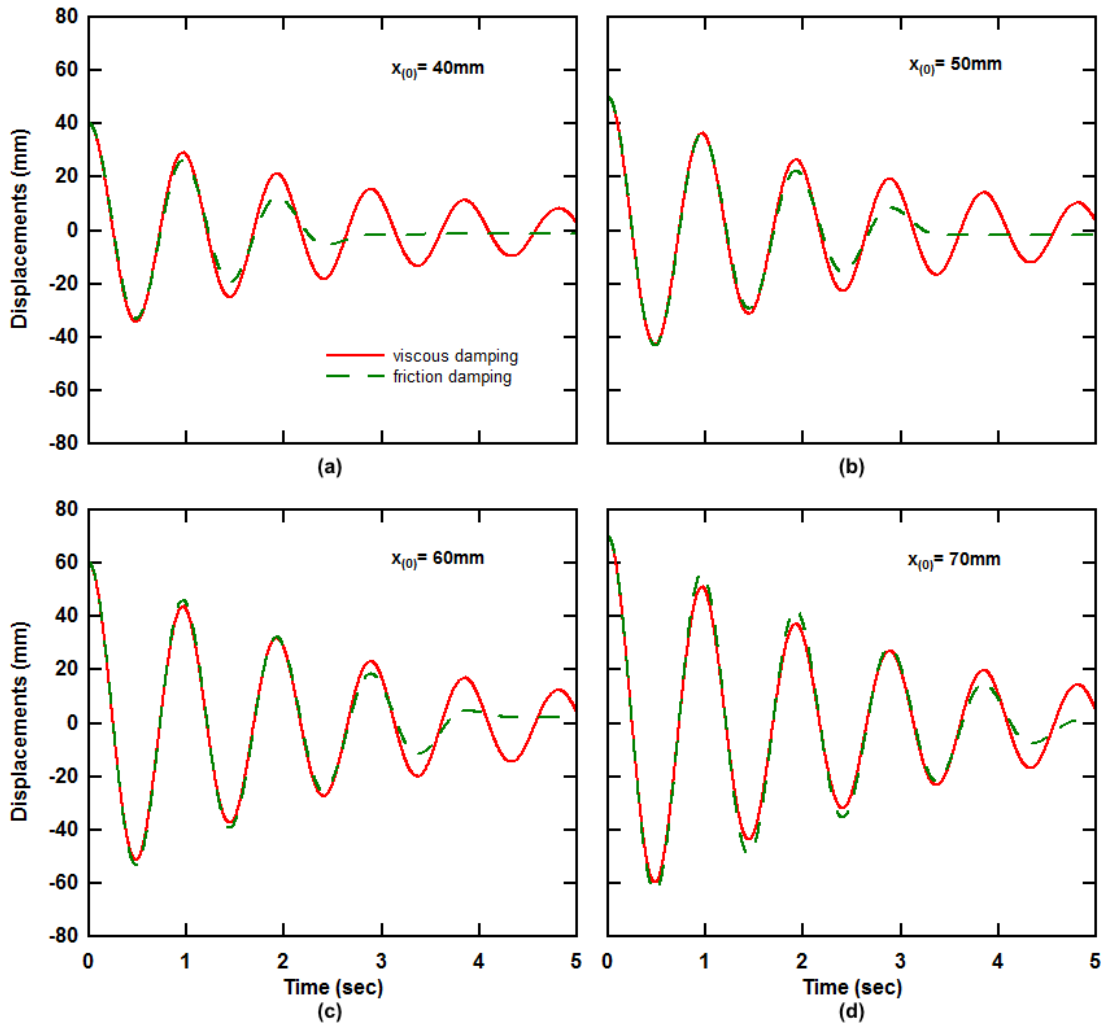


Figure C.3. Parametric study: the effect of initial displacement on the response of two systems of the same mass (2500kg) and stiffness (107kN/m), one with friction damping ($F=370\text{N}$) and the other with viscous damping ($\zeta = 0.05$), (soft spring case).

C.3. Varying Stiffness

Since two springs with different stiffnesses were used in the experiment, spring stiffness variation is chosen to be one of the studied parameters. Figure C.4 shows that for the same mass, damping ratio, and initial displacement, the response will

be dominated by friction more for softer spring, whereas for stiffer spring the response is dominated by viscous damping, until it reaches the end of response where it is controlled by friction.

In this case, the amount of potential force for medium spring is larger than that for soft spring, since they are distorted the same amount. In other word, the force needed for the medium spring to be displaced to the same distance that the soft spring has been displaced to is larger.

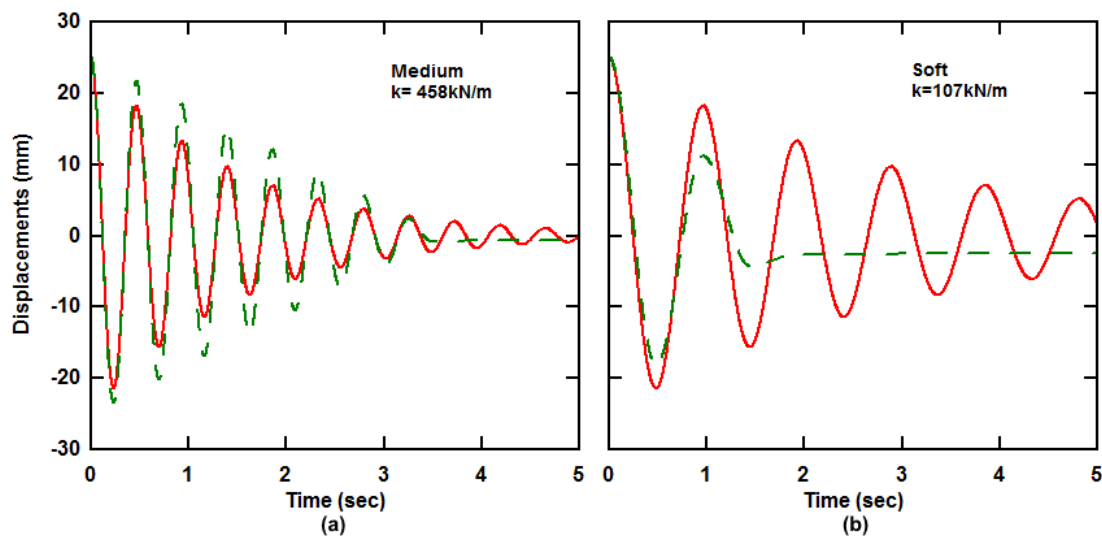


Figure C.4. Parametric study: the effect of system stiffness on the response of two systems having the same mass (2500kg), one with friction damping ($F=370\text{N}$) and the other with viscous damping ($\zeta = 0.05$), holding the initial displacement constant ($x(0)=25\text{mm}$).

C.4. Discussion and Conclusions

Two types of damping, viscous and friction damping, are studied in this appendix, and several distinct parameter configurations and cases discussed. Motion of bodies in fluid (water in this case) is opposed by forces proportional to the viscosity

of that fluid. Assuming that added mass has no effect in this case, let us call this opposing force “viscous damping force”. By mounting the experimental model on a guide rail to allow for horizontal movement, an additional, i.e. friction force, is introduced. The restoring force comes from the potential energy stored in the springs when they are deformed, which represents a distortion from their resting position.

When an initial displacement is introduced to the superstructure model, a force is stored in the springs in form of potential energy. Following release, a portion of this energy is gradually transformed into kinetic energy, whereas an additional portion is dissipated due to the friction force and viscous damping forces. When the model passes through the zero-displacement position, the kinetic energy reaches its maximum. This kinetic energy keeps model movement beyond the resting point if it is larger than the resisting forces (coming from friction and viscous damping forces). Passing the zero-displacement position, part of the kinetic energy will transform to potential energy and the other part will continue to be dissipated due to the friction force and viscous damping force. This schematic protocol in motion keeps happening until the motion is stopped.

As discussed in Section (C.1.1), as initial displacement increases, the domination of viscous damping increases, too. The increase in displacement is a manifestation of increasing in potential energy, according to:

$$PE = \frac{1}{2} \cdot k \cdot x^2 \quad (1.C)$$

Finally, it was observed that, as stiffness increases, the domination of viscous damping over friction damping increases. The increase in stiffness could be

interpreted as a simultaneous increase in potential energy, according to equation (1.C). The domination of one type of damping system means that there is a mitigation of the other type of damping. That is why the value of friction force is less for the medium springs setup with a decreasing trend (in the experimental data analysis). This also means that viscous damping reached a limit where any change in its value leads to an influential effect on the frictional domination. For the soft springs setup, however, due to the low value of stiffness, a low domination effect of viscous damping can be expected (has been mitigated) countered by an apparent increase in friction force (i.e. increase in the domination of friction force).

Appendix D: Scatter Plots of Wave-Induced Forces vs. Wave Height

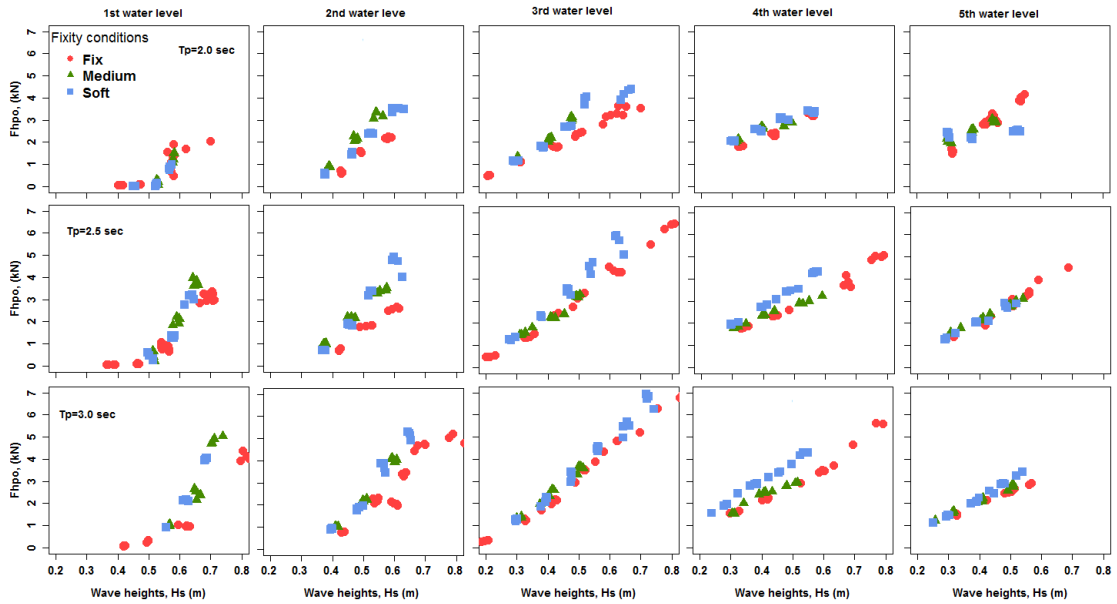


Figure D.1. Scatter plots of horizontal wave forces vs. wave height at water depths and wave periods.

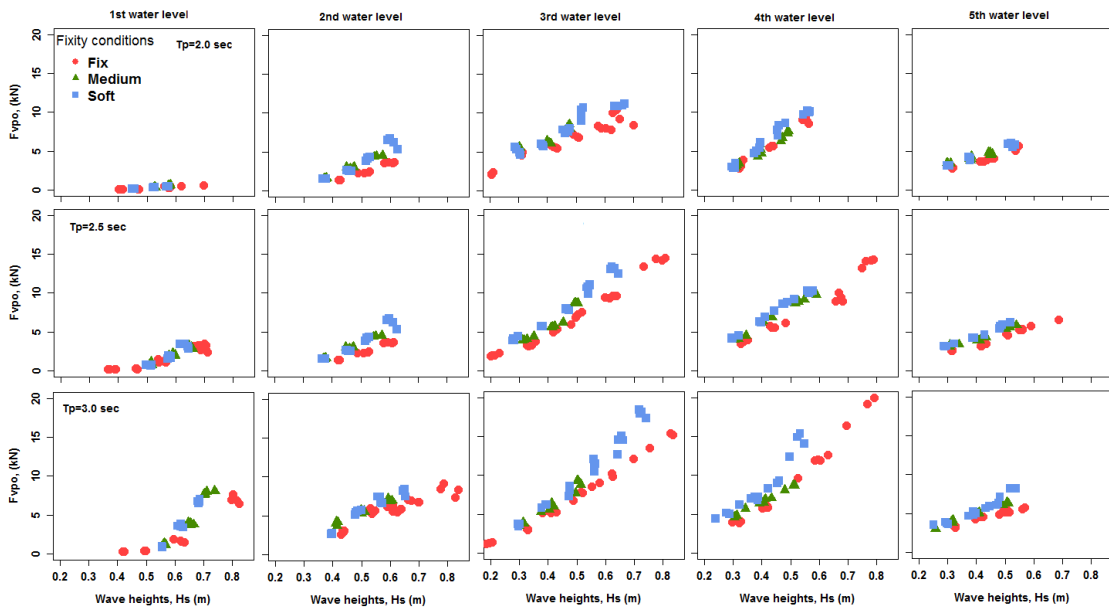


Figure D.2. Scatter plots of vertical wave forces vs. wave height at water depths and wave periods.

Appendix E: Magnification Factors for all Cases

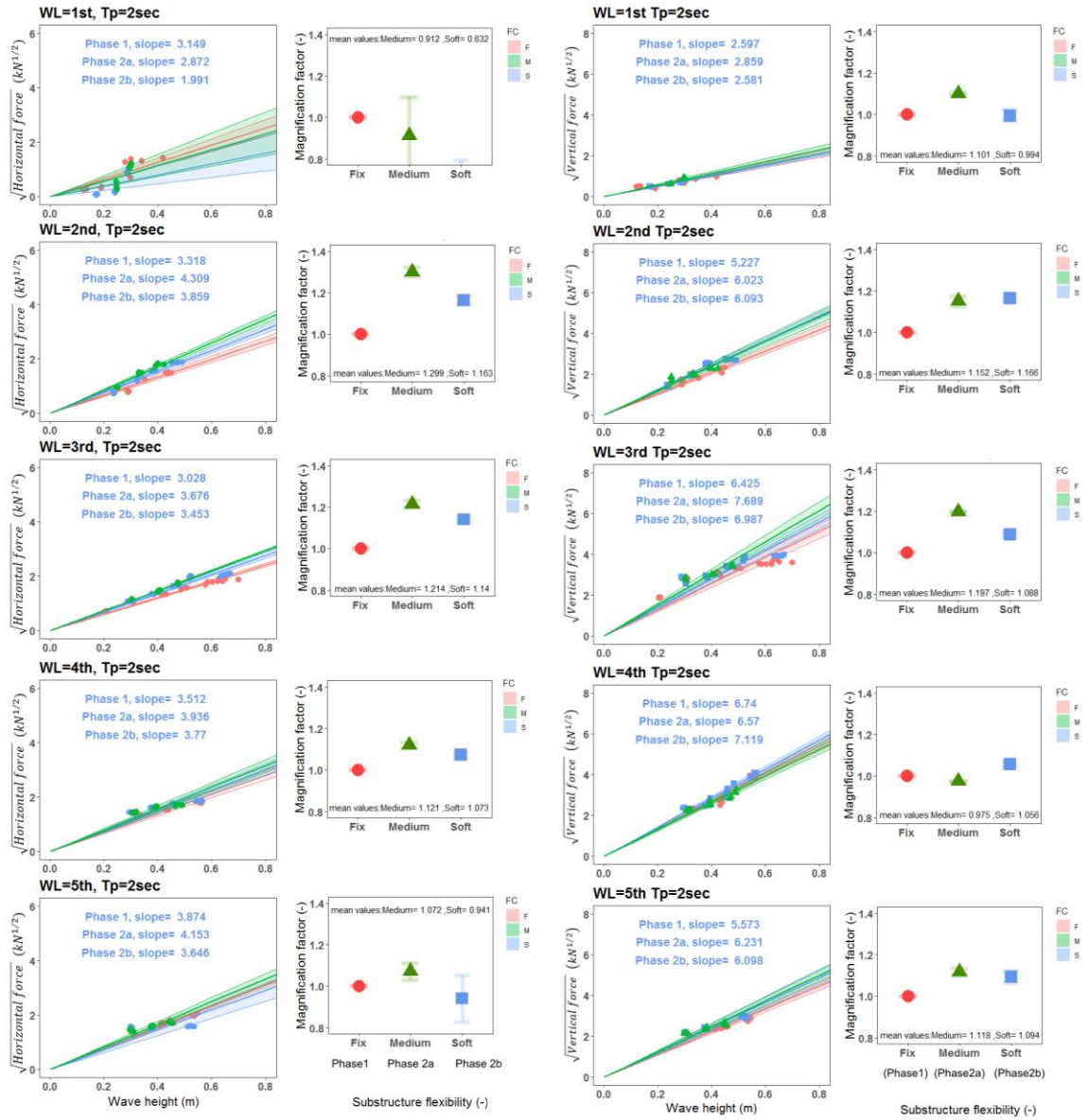


Figure E.1. Force magnification factors for horizontal and vertical forces at $T_p = 2.0$ s and different water levels.

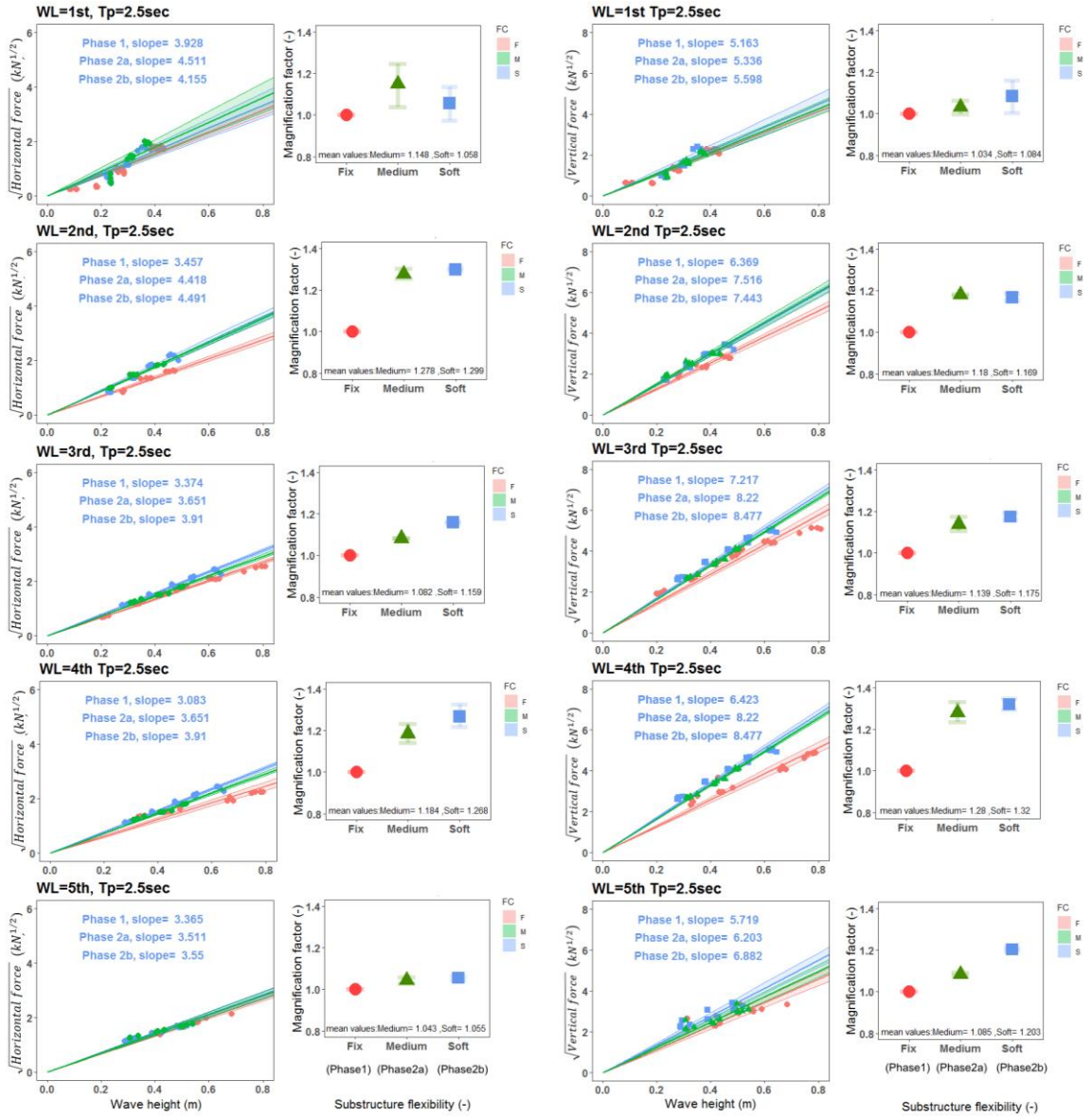


Figure E.2. Force magnification factors for horizontal and vertical forces at $T_p = 2.5$ s and different water levels.

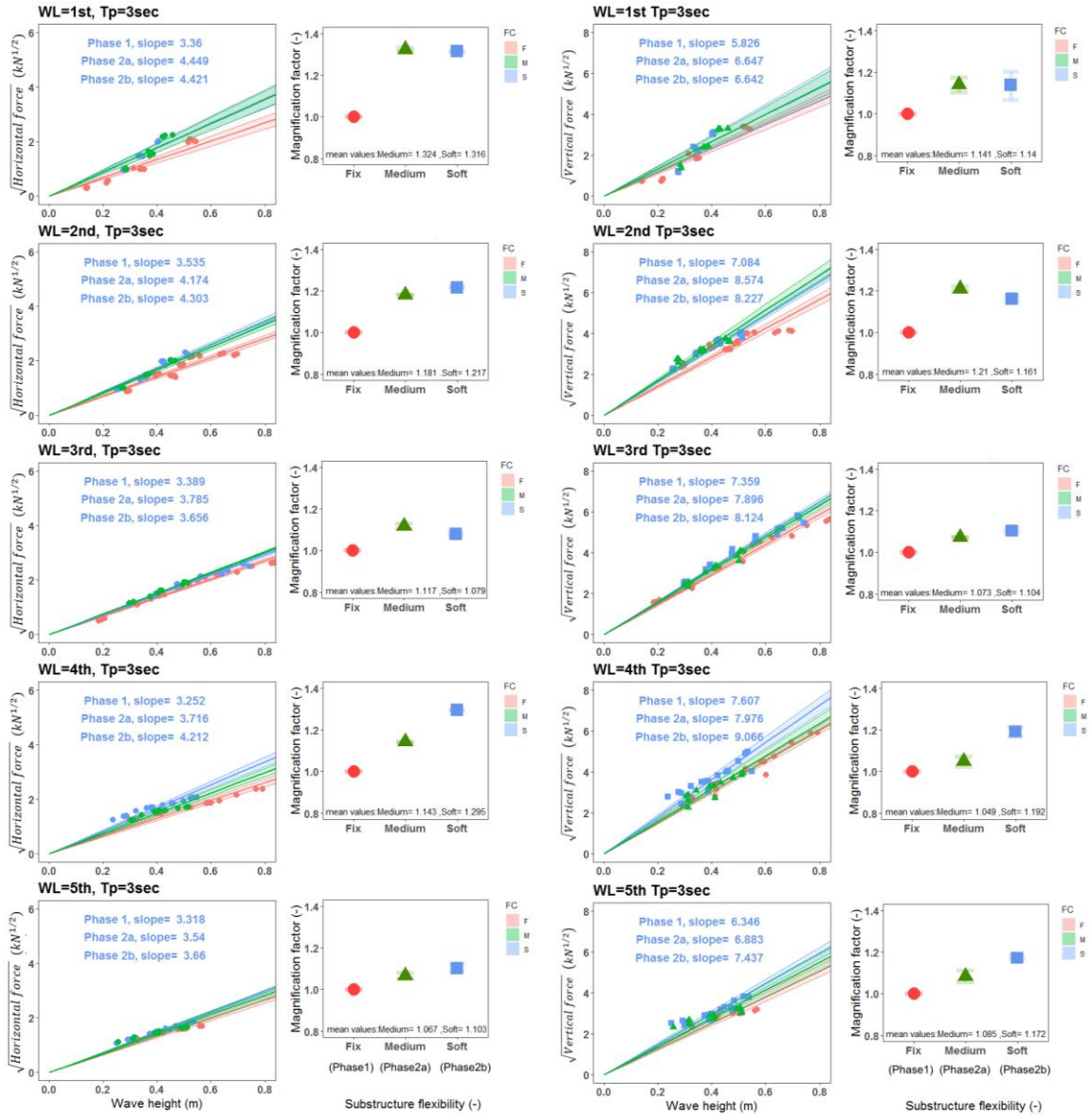


Figure E.1. Force magnification factors for horizontal and vertical forces at $T_p = 3.0$ s and different water levels.

Appendix F: Experiment -simulation results comparisons

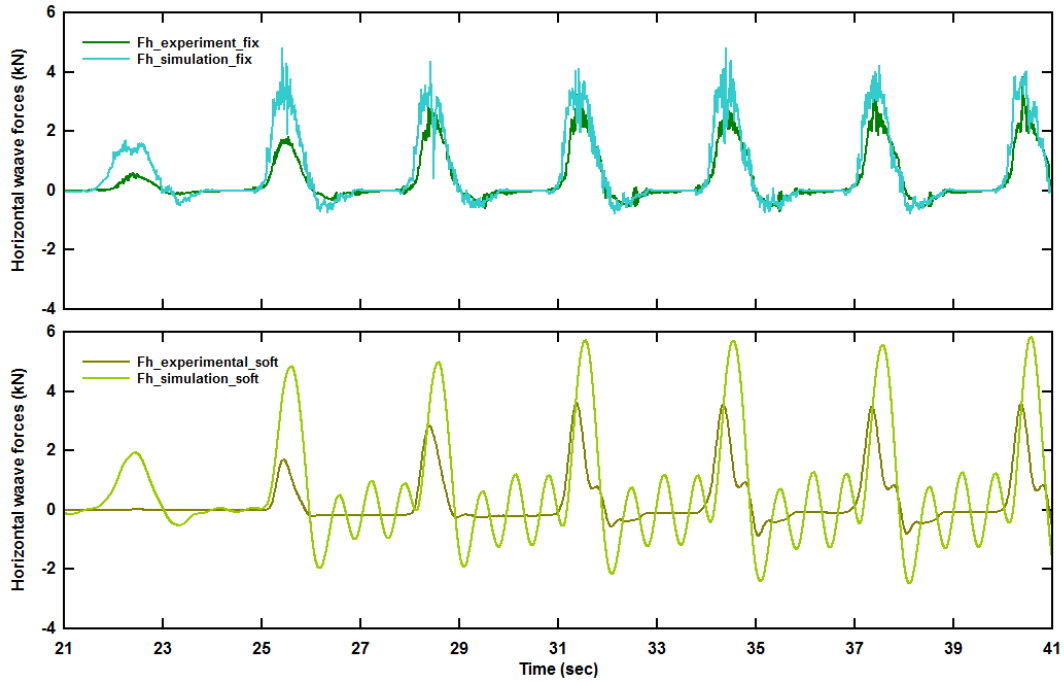


Figure F.1. Simulation results for horizontal forces compared with the experimental data for case $d^* = 0.0$, $H = 0.625\text{m}$, and $T_p = 3.0\text{sec}$, and for both rigid and soft setups.

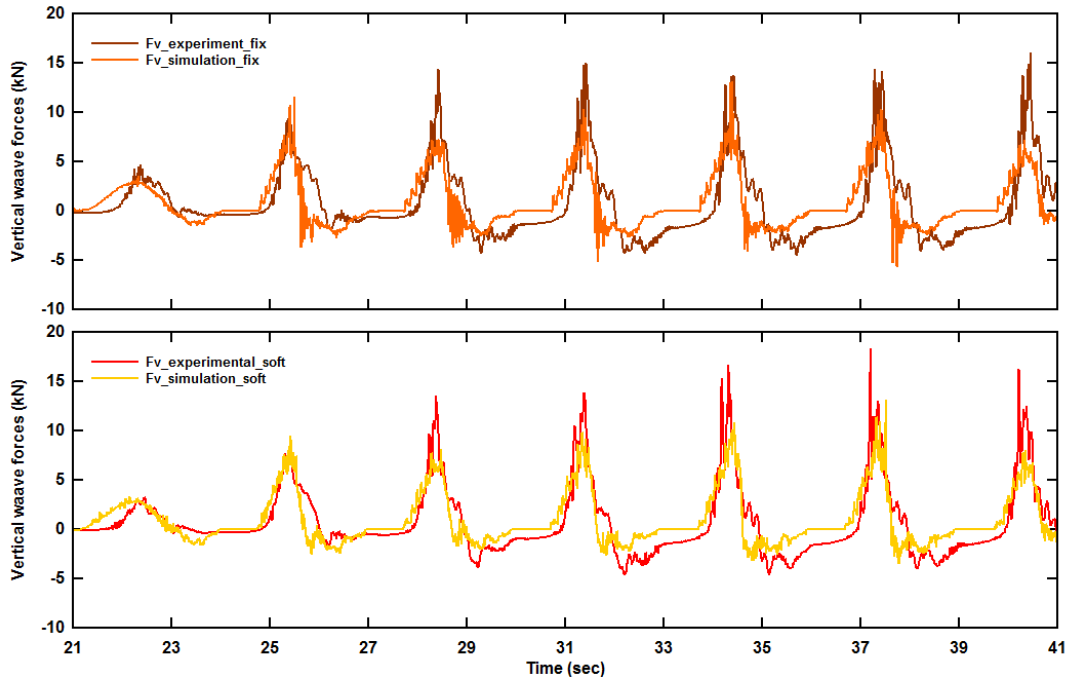


Figure F.2. Simulation results for vertical forces compared with the experimental data for case $d^* = 0.0$, $H = 0.625\text{m}$, and $T_p = 3.0\text{sec}$, and for both rigid and soft setups.

Appendix G: Flexibility Effect via Experiment and Simulation Results

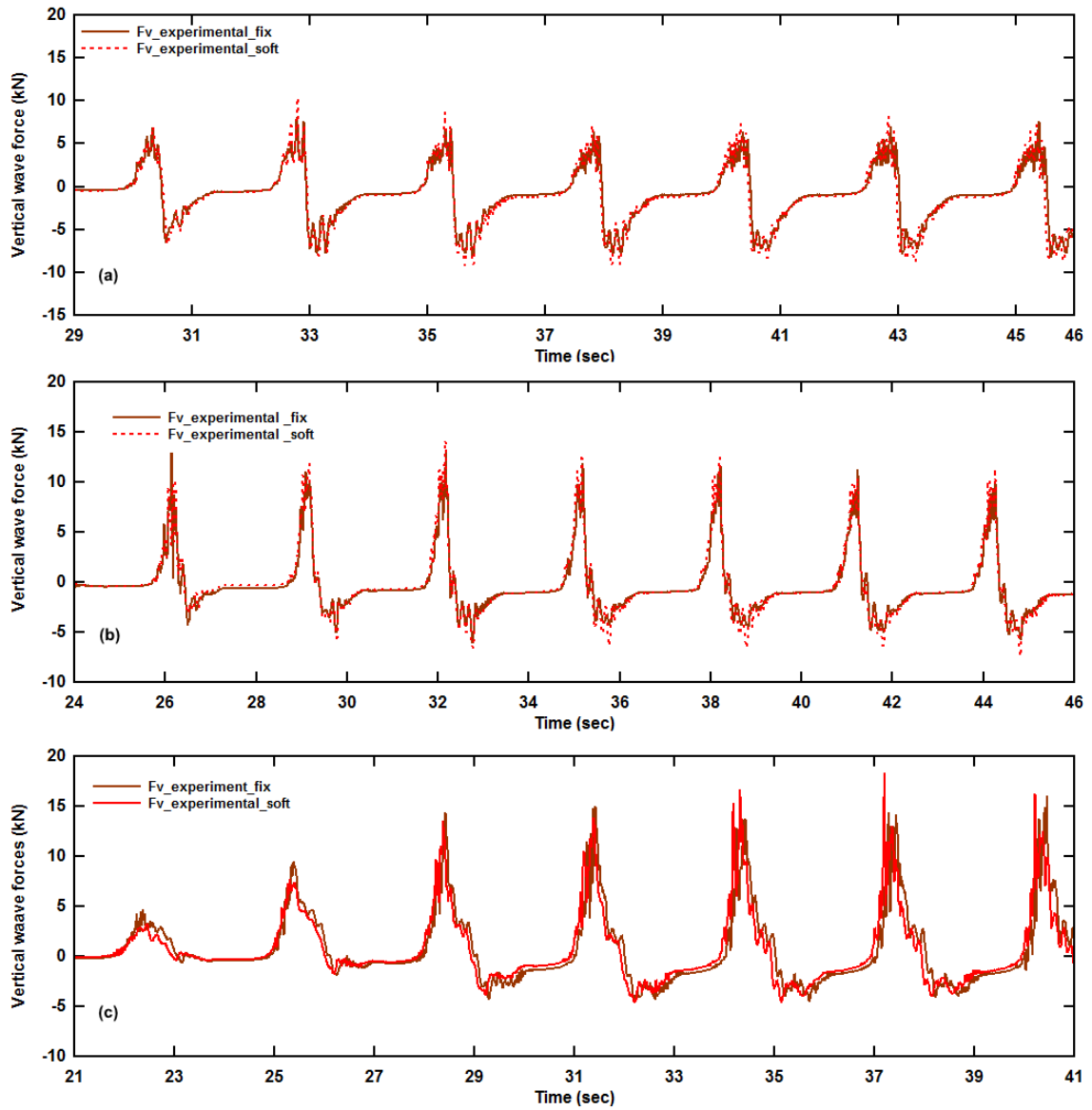


Figure G.1. Fixity condition effect on vertical forces for experimental results.

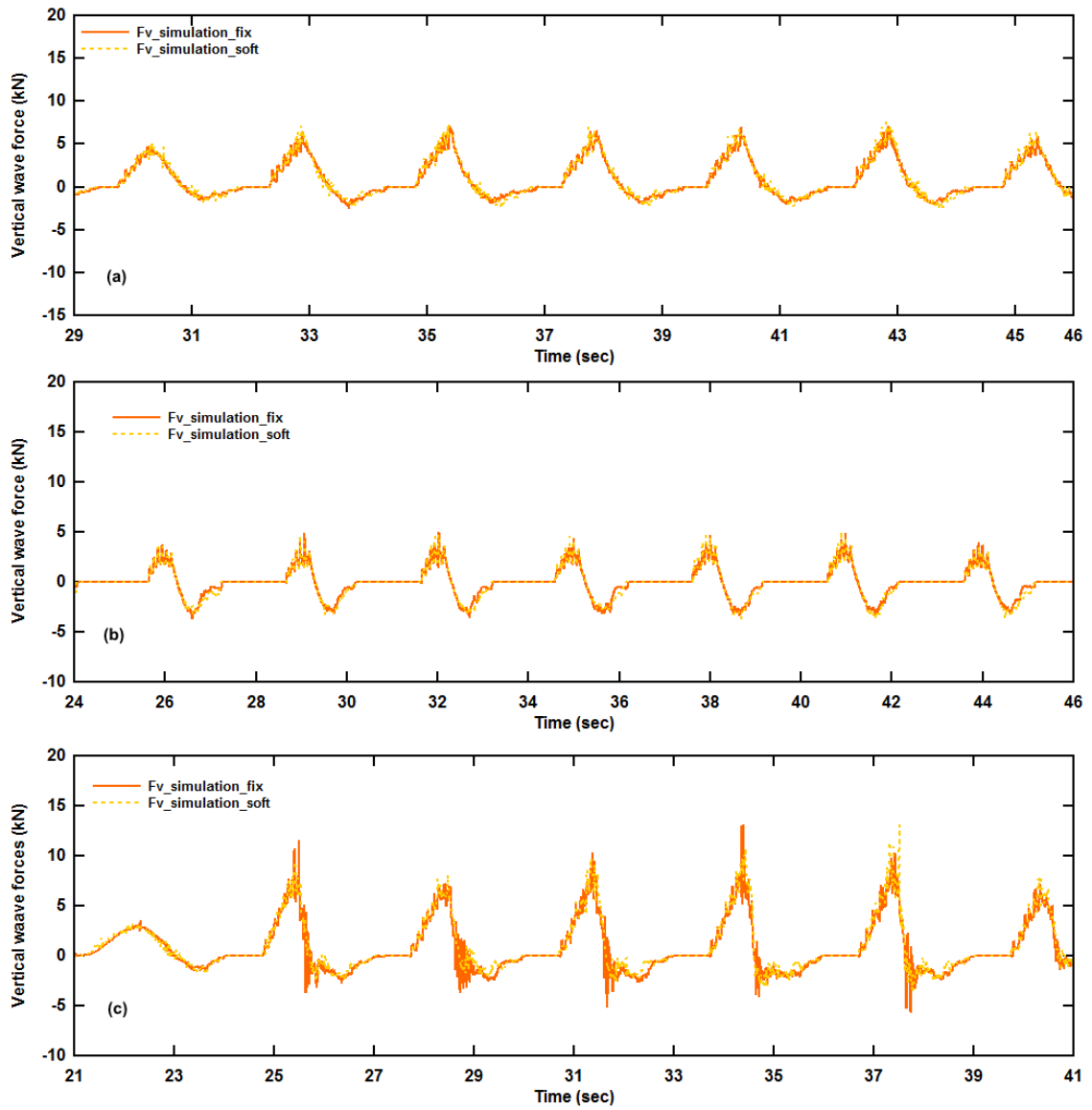


Figure G.2. Fixity condition effect on vertical forces for simulation results.